Dijets in Photoproduction and Soft Multiparton Interactions at HERA

Sebastian Naumann

Hamburg, 2007

Diplomarbeit

am Institut für Experimentalphysik
der Universität Hamburg

Tag der Abgabe: 5. April 2007

1. Gutachter: Prof. Dr. R. Klanner
2. Gutachter: JunProf. Dr. J. Haller

Abstract

Dijet events in photoproduction at HERA have been studied using data collected with the ZEUS detector in the period 1998-2000 that correspond to an integrated luminosity of $81.7\,\mathrm{pb}^{-1}$. The events have been selected in a kinematic region defined by restricting the virtuality of the incoming photon, Q^2, to $Q^2 < 1\,\mathrm{GeV}^2$ and its inelasticity, y, to $0.2 < y < 0.85$. This results in photon-proton center-of-mass energies in the range of $142\,\mathrm{GeV} < W < 293\,\mathrm{GeV}$. Jets have been reconstructed with the k_T-clustering algorithm and required to be in the pseudorapidity range $-1.0 < \eta < 2.4$. Differential cross sections have been measured for two different sets of jet selection criteria. One sample of dijet events has been obtained by demanding at least two jets with transverse energies of $E_{T,1} > 14\,\mathrm{GeV}$ and $E_{T,2} > 11\,\mathrm{GeV}$ in each event. Cross sections measured for this inclusive dijet sample have been compared to results obtained in data from the 1996-1997 period. Another sample of dijet events has been obtained using the transverse-energy requirements $E_{T,1} > 10\,\mathrm{GeV}$ and $E_{T,2} > 8\,\mathrm{GeV}$, demanding additionally that the two jets are roughly back-to-back in the azimuthal plane and have almost equal transverse energies and that no third hard jet is found in the event. All results have been compared to leading-order Monte Carlo predictions. The transverse energy in the region between the jets shows a large sensitivity to multiparton interactions, allowing parameters of the corresponding models to be tested. The measurement suggests that multiparton interactions are needed to describe the data. The analysis presented here contains the most comprehensive study of soft multiparton interactions at ZEUS to date.

Kurzfassung

Zweijet-Ereignisse in Photoproduktion bei HERA wurden in Daten des ZEUS-Detektors aus den Jahren 1998-2000 untersucht. Die Daten entsprechen einer integrierten Luminosität von $81.7\,\mathrm{pb}^{-1}$. Der kinematische Bereich der Analyse wurde definiert, indem die Virtualität des einlaufenden Photons, Q^2, auf $Q^2 < 1\,\mathrm{GeV}^2$ und seine Inelastizität, y, auf $0.2 < y < 0.85$ eingeschränkt wurden. Dies führt auf Photon-Proton-Schwerpunktsenergien im Bereich von $142\,\mathrm{GeV} < W < 293\,\mathrm{GeV}$. Jets wurden mit dem k_T-Clustering-Algorithmus rekonstruiert und ihre Pseudorapidität auf den Bereich $-1.0 < \eta < 2.4$ eingeschränkt. Differentielle Wirkungsquerschnitte wurden für zwei verschiedene Jet-Selektionen gemessen. Ein Satz von Zweijet-Ereignissen wurde selektiert, indem mindestens zwei Jets mit Transversalenergien von $E_{T,1} > 14\,\mathrm{GeV}$ und $E_{T,2} > 11\,\mathrm{GeV}$ in jedem Ereignis verlangt wurden. Wirkungsquerschnitte, die für diesen Satz inklusiver Zweijet-Ereignisse gemessen wurden, wurden mit Ergebnissen verglichen, die mit Daten aus den Jahren 1996-1997 gewonnen worden waren. Ein weiterer Satz von Zweijet-Ereignissen wurde mit Transversalenergien von $E_{T,1} > 10\,\mathrm{GeV}$ und $E_{T,2} > 8\,\mathrm{GeV}$ selektiert, wobei zusätzlich gefordert wurde, dass die beiden Jets ungefähr entgegengesetzte Richtungen in der Azimutalebene sowie beinahe gleiche Transversalenergien aufweisen und dass sich kein dritter harter Jet im Ereignis findet. Alle Ergebnisse wurden mit Vorhersagen von Monte-Carlo-Simulation in führender Ordnung verglichen. Die Transversalenergie in der Region zwischen den beiden Jets zeigt starke Sensitivität auf Multiparton-Wechselwirkungen, was es ermöglicht, die Parameter entsprechender Modelle zu testen. Die Messungen deuten darauf hin, dass Multiparton-Wechselwirkungen für eine gute Beschreibung der Daten notwendig sind. Die hier vorgestellte Analyse enthält die bislang eingehendste Untersuchung von weichen Multiparton-Wechselwirkungen bei ZEUS.

Contents

Introduction

The fundamental constituents of our universe, which cannot be further subdivided, are called elementary particles. The aim of particle-physics research is to identify, describe and understand these particles, their properties and the interactions between them.

According to our current understanding, there are four fundamental forces: gravity, electromagnetism and the weak and strong nuclear forces. The latter three have been successfully described by gauge theories. They are the pillars of the so-called Standard Model of particle physics, a theoretical framework that accommodates practically all observations made up to now. The Standard Model contains a relatively small number of elementary particles, which are classified into three basic types: leptons (e, ν_e, μ, ν_μ, τ, ν_τ), quarks (d, u, s, c, b, t) and fundamental bosons (γ, W, Z, g, H). There are three families of quarks and three families of leptons. Each family consists of two particles. In addition, all quarks and leptons have their respective antiparticles. The fundamental interactions of the Standard Model are mediated via the exchange of the gauge bosons γ, W, Z and g. The photon, γ, mediates the electromagnetic interaction between all electrically charged particles. The gauge bosons W and Z are the mediators of the weak force between all particles that carry a weak isospin, i.e. a "weak charge" (quarks and leptons and the bosons W and Z themselves). The gluon, g, which exists in different color states, is responsible for the strong force between particles with color charge (quarks and gluons). The Higgs boson, H, which remains the only particle in the Standard Model that has not been observed yet, is believed to be responsible for the masses of all particles.

Current flagships of high-energy particle-physics research are HERA, where electrons or positrons are brought into collision with protons at a center-of-mass energy of 318 GeV, and the TEVATRON, colliding protons with anti-protons at nearly 2 TeV. HERA is the only lepton-proton collider world-wide and offers unique possibilities to study both electroweak and strong interactions. The "Large Hadron Collider" (LHC), which is currently under construction and will start its operation in the second half of 2007, will collide protons at a center-of-mass energy of 14 TeV. Experiments at this unprecedented energy will enable not only further precision measurements, they will most probably lead at least either to the long-expected discovery of the Higgs boson or to the discovery of physics beyond the Standard Model.

Quantum Chromodynamics (QCD) is the theory of the strong nuclear force. In recent years, precise perturbative QCD predictions for high energies have become available. Despite all success and progress, the predictive power is quantitatively still not at a satisfactory level in some regions of the phase space in which perturbative methods cannot be applied. The LHC will give us new amazing opportunities for studying QCD phenomena. But at the same time, a good understanding of QCD is the basis for the whole LHC physics program, because identifying any signal of new or interesting physics will require a precise knowledge of the background from QCD-induced processes.

When two composite objects collide, more than one pair of constituents might interact. The possibility of so-called multiparton interactions (MPI) has to be taken into account at high center-of-mass energies. There is experimental evidence that MPI change the topology of events by producing a particle flow that leads to additional particle jets in the final state or - presumably in most of the cases - to an energy pedestal in the detectors. Extensive studies have been carried out at the TEVATRON. However, MPI are far from being understood, and there are large uncertainties associated with extrapolating the available phenomenological models to other energies. An understanding of MPI is crucial for developing robust analyses for future experiments and for the LHC in particular, but it is also an interesting physics topic in its own right.

At HERA, MPI might occur in resolved photon events, where a photon is emitted by the lepton and fluctuates into a partonic system before interacting with the proton. In consequence, HERA can contribute to the MPI studies. First, the additional range in energy that can be provided (around 200 GeV in the γp system) will help to pin down the energy dependence of MPI. Second, γp initial states constitute an alternative field to confront the MPI models with. Furthermore, it is possible to effectively switch MPI on or off by selecting regions of phase space where resolved or direct (i.e. point-like) photons dominate. In addition, the boost of the γp system in the laboratory frame of reference means that particles that have been produced by partons carrying only a small momentum fraction within the proton appear in the central region of the detectors. These are benefits of HERA that are neither present at the TEVATRON nor at the LHC.

In this thesis, an analysis of MPI in photoproduction dijet events at HERA is presented. The theoretical background of QCD, HERA physics and MPI is given in chapter 1. The HERA accelerator and the ZEUS detector are described in chapter 2. In chapter 3, the event simulation is described. The reconstruction of event variables, the selection of events for this analysis and the unfolding of the data are explained in chapter 4, chapter 5 and chapter 6, respectively. The results are presented in chapter 7. Finally, a summary is given and conclusions are drawn.

Chapter 1

Theoretical Framework

1.1 Quantum Chromodynamics

QCD is the theory of the strong interaction between quarks and gluons, one of the four fundamental forces in nature. Since there is much evidence that supports this theory [1, 2], it is regarded nowadays as one of the pillars of the Standard Model of particle physics. In this section, the main aspects of QCD will be pointed out.

1.1.1 Strong Interactions and Color Charge

The concept of the strong force was introduced phenomenologically in order to explain the binding of protons and neutrons inside atomic nuclei. The binding energies were known to be much larger than what could be expected from the electromagnetic force, but while the latter had an infinitive range, the strong force acted only within nuclear distances.

A large number of strongly interacting particles, which were denominated hadrons, was found over the years. This variety was simplified by the introduction of quarks as fundamental constituents of hadrons [3, 4]. The problem of an apparent violation of the Pauli principle by hadrons containing identical quarks was solved with the postulation of a new degree of freedom [5, 6]. The concept of this degree of freedom called color charge with three different states, commonly denominated reg, green and blue, was affirmed by measurements, for instance of the ratio R_{had}[1].

[1] In e^+e^- events, the ratio of the total hadronic cross section to the corresponding cross section for the production of lepton pairs, e.g. muons, at leading-order quantum electrodynamics can be calculated as $R_{\text{had}} = \sigma(e^+e^- \to \text{hadrons})/\sigma(e^+e^- \to \mu^+\mu^-) = N_c \sum_q Q_q^2$, where the sum runs over all active quark flavors, Q_q is the quark charge and N_c the number of colors.

QCD as a description of the strong interaction by a mathematically consistent quantum field theory was presented in the early 1970's [7]. Here, gauge bosons named gluons couple to the color charges of quarks and - as they carry color charges themselves - also to other gluons. It was shown at the same time that non-Abelian gauge theories exhibit the property of asymptotic freedom [8, 9].

1.1.2 Asymptotic Freedom and Confinement

In quantum field theories like QCD, physical observables can be expressed as a perturbation series in powers of the coupling parameter. If the couplings are small ($\ll 1$), the series may converge sufficiently quickly such that a realistic prediction of the observable is provided by a limited number of perturbative orders.

When calculating a physical quantity as a perturbation series in the strong coupling parameter α_s, renormalization is required to remove ultraviolet divergences. The renormalization procedure introduces an arbitrary energy scale μ_R, at which subtractions that remove the ultraviolet divergences are performed, and leads to a renormalized coupling $\alpha_s(\mu_R)$. The renormalization scale is usually identified with a physical energy scale of the process. To lowest-order perturbation theory, the so-called "running coupling" of QCD can be expressed as follows:

$$\alpha_s(\mu_R^2) = \frac{12\pi}{(33 - 2N_f)} \frac{1}{\ln(\mu_R^2/\Lambda^2)} \tag{1.1}$$

In this formula, N_f is the number of active flavors at the energy scale μ_R^2 and the parameter Λ represents the scale at which the coupling would diverge if extrapolated outside the perturbative domain, i.e. $\alpha_s(\mu_R^2) \to \infty$ for $\mu_R^2 \to \Lambda^2$. The value of Λ has to be deduced from experiments and is in the order of a few hundred MeV. Figure 1.1 shows an example of the energy-scale dependence of α_s.

The vanishing of strong interactions at high energies, i.e. $\alpha_s(\mu_R^2) \to 0$ for $\mu_R^2 \to \infty$, leads to the fact that quarks and gluons behave like free particles at high energies or, equivalently, at small distances. Another important consequence of asymptotic freedom is that the strong coupling gets sufficiently small at high energies to obtain quantitative predictions of physical processes from perturbation theory. Interactions at these energy scales are often referred to as hard processes, while interactions at energies at which perturbative methods may not be applied are referred to as soft processes.

The increase of the strong coupling at low energies and large distances leads to the fact that quarks and gluons are confined inside hadrons, which exhibit no net color charge. Trying to separate two quarks, for instance, results in increasing the energy of the color field in between them, and at some point it becomes possible to minimize the potential energy by creating new quarks out of the vacuum. Thus no isolated color charged particles

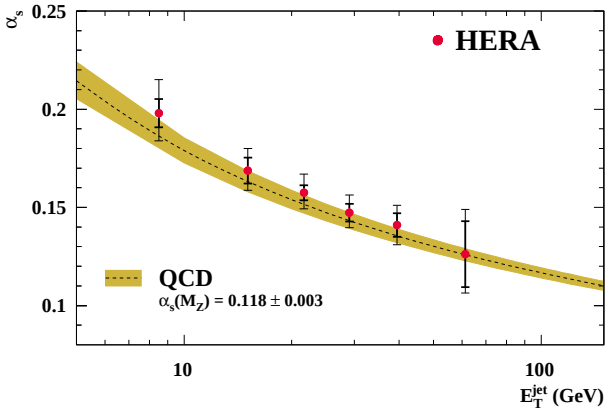

Figure 1.1: Running of the strong coupling. See [10] for details.

can be observed. Quarks and gluons emerge as "dressed-up" hadrons. The final result of high-energy QCD interactions are therefore bundles of hadrons. The properties of these bundles called jets[2] can be measured in a detector and are closely correlated with the properties of the initiating particles.

1.1.3 Factorization

Due to the contribution of long-distance interactions, not computable in perturbative QCD, it is not possible to calculate cross sections of scatterings involving hadrons directly in perturbation theory, even at high center-of-mass energies. However, factorization theorems allow to separate long-distance from short-distance effects [11].

The long-distance behavior of a hadron can be described using functions specifying the distribution of partons in the hadron. The term parton refers to point-like particles that carry a fraction x of the hadron momentum, moving without interacting among each other inside the hadron. The parton distribution functions (PDFs) have to be determined experimentally. A large number of different sets is available [12]. Figure 1.2 shows recent results for the proton PDF. Besides the distributions of the valence quarks in the proton (one d quark and two u quarks), it can be seen that for low x a significant contribution comes from gluons and so-called sea quarks (both scaled down in this illustration by a factor of 20).

The final cross section is a sum over the perturbatively calculable short-distance cross sections for all partons, convoluted with their corresponding PDFs. Examples will be given in section 1.2.2.

[2] A jet is not a universally defined object and its exact properties depend on the algorithm used to associate observed objects with the jet.

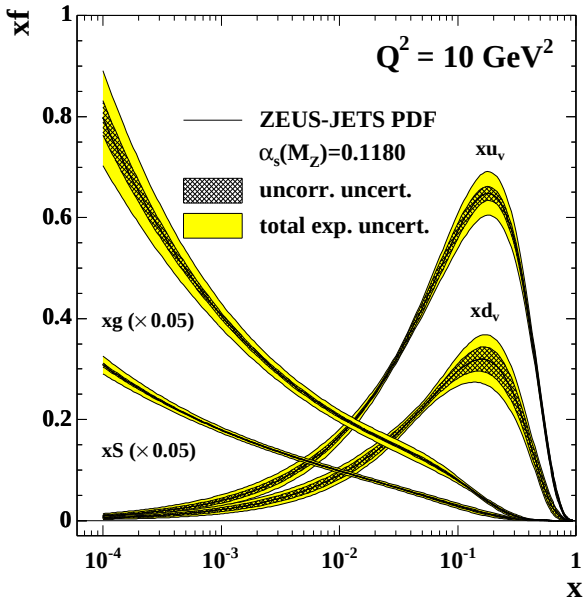

Figure 1.2: The valence-quark, sea-quark and gluon distributions extracted from the ZEUS-JETS fit [13].

1.2 Physics at HERA

In this section, the general kinematics of electron[3]-proton collisions at HERA as well as the characteristics of photoproduction events will be described.

1.2.1 Kinematics

In electron-proton collisions, the incoming electron scatters from the hadronic system via the exchange of a virtual gauge boson. The scattering process is mediated either by the electromagnetic force (photon exchange) or by the weak force (Z^0 or $W^\pm$ exchange). In neutral current events, where the exchanged boson is a photon or a Z^0, the electron is scattered through some angle. In the case of a charged current event, the interaction is mediated by a $W^\pm$ and the final-state lepton is a neutrino, which can only be detected indirectly via missing energy and missing momentum. The analysis in this thesis is based on single-photon exchange in neutral current events. Due to its mass, the exchange of a Z^0 is highly suppressed in the considered kinematic range.

The part of the proton that does not participate directly in the scattering is referred to as the proton remnant. It creates a shower of hadrons at low angles with respect to the initial proton direction.

[3]In the following, the generic name electron is used for both electrons and positrons if not stated otherwise.

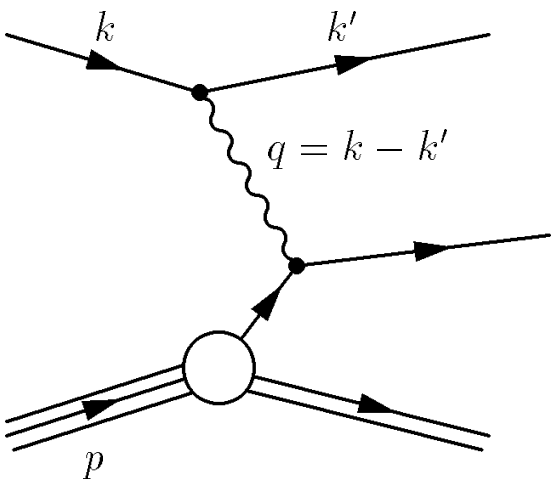

Figure 1.3: Kinematics of lepton-proton scattering at HERA.

A generic lepton-proton scattering is illustrated in figure 1.3. The four-momenta of the incoming and the scattered lepton are labeled k and k', respectively, p is the four-momentum of the proton and the four-momentum transferred between lepton and proton system is denoted by q. The kinematics of the scattering are most conveniently described by introducing Lorentz-invariant products of these four-vectors[4]:

$$s = (k+p)^2 = m_e^2 + m_p^2 + 2kp \tag{1.2}$$

$$Q^2 = -q^2 = -(k-k')^2 \tag{1.3}$$

$$W^2 = (p+q)^2 = m_p^2 + q^2 + 2pq \tag{1.4}$$

$$y = \frac{pq}{kp} \tag{1.5}$$

The squared center-of-mass energy $s = E_{\mathrm{CM}}^2$ is calculated from the four-momenta of the incoming particles. Neglecting the masses gives:

$$E_{\mathrm{CM}} \approx 2\sqrt{E_e E_p} \tag{1.6}$$

The negative squared momentum transferred in the scattering, Q^2, determines the virtuality of the exchanged boson. For $Q^2 \gtrsim \mathcal{O}(1\,\mathrm{GeV}^2)$, the regime of deep inelastic scattering (DIS), a virtual boson is exchanged. For $Q^2 \approx 0\,\mathrm{GeV}^2$, in contrast, the interaction is mediated by a quasi-real photon. These events are referred to as photoproduction.

A simple relation for the center-of-mass energy of the boson-proton system, W, can be derived by neglecting the proton mass:

$$W \approx \sqrt{sy - Q^2} \tag{1.7}$$

[4]Rationalized natural units with $\hbar = c = 1$ are used in this thesis. Energies, momenta and masses are thus all expressed in the same units.

The inelasticity y corresponds to the fraction of the electron energy transferred to the photon. It can be calculated from the energy E'_e and the polar angle θ'_e of the scattered lepton, measured in the laboratory frame and defined with respect to the direction of the incoming proton:

$$y = 1 - \frac{E'_e}{2E_e}(1 - \cos\theta'_e) \tag{1.8}$$

In photoproduction, the electron is scattered under a small angle, which means its polar angle remains close to 180°. In the limit $\theta'_e \to 180°$, equation 1.8 reduces directly to the following relation:

$$y = 1 - \frac{E'_e}{E_e} = \frac{E_\gamma}{E_e} \tag{1.9}$$

1.2.2 Cross Sections in Photoproduction

In the photoproduction regime, the incoming electron beam can be considered to be equivalent to a broad-band beam of real photons, whose momenta are distributed according to the Weizsäcker-Williams formula [14]:

$$f_\gamma^{(e)} = \frac{\alpha_{\text{em}}}{2\pi}\left[\frac{1+(1-y)^2}{y}\log\left(\frac{Q^2(1-y)}{m_e^2 y^2}\right) + 2m_e^2 y\left(\frac{1}{Q^2} - \frac{1-y}{m_e^2 y^2}\right)\right] \tag{1.10}$$

Here, α_{em} is the coupling constant of the electromagnetic interaction. The radiated photon subsequently interacts with the proton. The flux factor $f_\gamma^{(e)}$ factorizes from the total ep cross section, leaving the γp contribution [15]:

$$d\sigma_{ep}^{\text{tot}} = \int_y dy\ f_\gamma^{(e)}\ d\sigma_{\gamma p}^{\text{tot}} \tag{1.11}$$

Photoproduction can be classified into two types of processes: direct and resolved γp interactions.

- In direct photoproduction, the bare photon interacts directly with a parton from the proton. The two possible processes in leading order are $\gamma q \to qg$ (QCD Compton scattering) and $\gamma g \to q\bar{q}$ (boson-gluon fusion). Both are perturbatively calculable. Diagrams for direct events can be seen in figures 1.4.1 and 1.4.2.
- In resolved photoproduction, the photon acts as a source of quarks and gluons, which then interact with partons from the proton. In this case, only a fraction x_γ of the photon momentum participates in the hard scatter and a photon remnant is left behind. The fluctuation of the photon into a hadronic state is enabled by the low virtuality and, equivalently, the long life-time of the photon. The distribution of partons inside the photon can be described using PDFs. At leading order, possible processes in resolved events are (figure 1.4.3 shows exemplarily one of them):
  $qq' \to qq' \quad ; \quad q\bar{q} \to q'\bar{q}' \quad ; \quad q\bar{q} \to gg \quad ; \quad qg \to qg \quad ; \quad gg \to q\bar{q} \quad ; \quad gg \to gg$

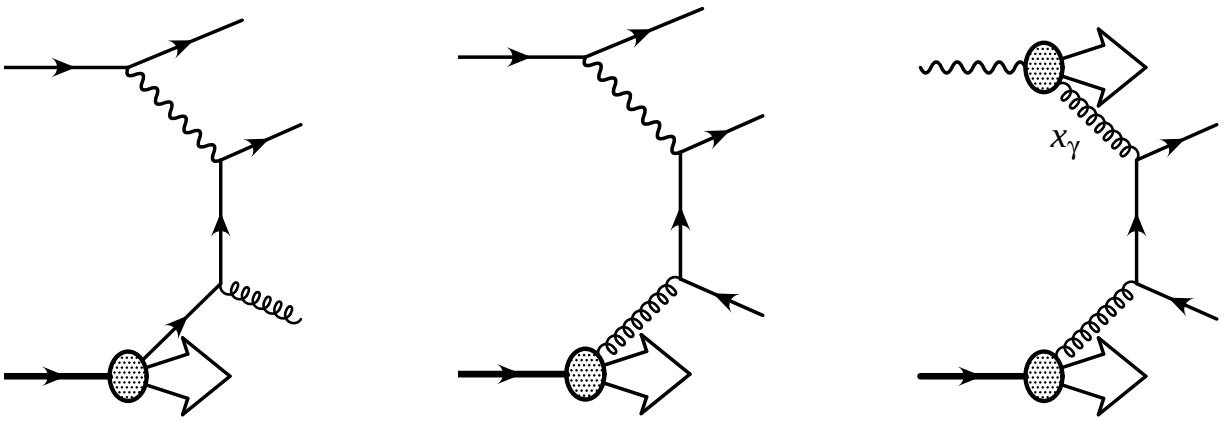

1: QCDC. **2**: BGF. **3**: Resolv. photoprod.

Figure 1.4: Diagrams for the two dominant processes in direct photoproduction, QCD Compton scattering (QCDC) and boson-gluon fusion (BGF), and one example for a process in resolved photoproduction (the scattered electron is omitted in this diagram).

The hard interaction in both the direct and the resolved photoproduction can give rise to two or more jets.

The total γp cross section contains the direct and the resolved component:

$$d\sigma_{\gamma p}^{\text{tot}} = d\sigma_{\gamma p}^{\text{dir}} + d\sigma_{\gamma p}^{\text{res}} \tag{1.12}$$

Let x_p be the fraction of the proton momentum carried by the initial-state parton. At leading order, the dijet cross section for resolved photoproduction is then given by:

$$d\sigma_{\gamma p}^{\text{res}} = \sum_{ij} \int_{x_\gamma} \int_{x_p} dx_\gamma \; dx_p \; f_i^{(\gamma)} \; f_j^{(p)} \; d\sigma_{ij} \tag{1.13}$$

The sum runs over all types of partons in the proton and the resolved photon. σ_{ij} is the cross section of the hard interaction between partons i and j. $f^{(p)}$ and $f^{(\gamma)}$ are the proton and photon PDFs, respectively. Replacing the photon structure by a delta function at $x_\gamma = 1$ gives the cross section for direct photoproduction:

$$d\sigma_{\gamma p}^{\text{dir}} = \sum_{j} \int_{x_p} dx_p \; f_j^{(p)} \; d\sigma_{\gamma j} \tag{1.14}$$

For a two-to-two parton scattering in leading-order QCD, the fraction of the photon energy

involved in the hard scatter can be calculated from the transverse energies $E_{T,i}$ and the pseudorapidities[5] η_i of the two final-state partons [16]:

$$x_\gamma = \frac{E_{T,1}\ e^{-\eta_1} + E_{T,2}\ e^{-\eta_2}}{2yE_e} \tag{1.15}$$

Since it is not possible to directly measure partons, an observable x_γ^{obs} is defined, analogously to x_γ from the above equation but referring to the transverse energies and the pseudorapidities of the two leading jets in the event.[6]

The matrix element in the partonic cross section for the two-to-two scattering process can be written in terms of the usual Mandelstam variables $\hat{s} = (p_i + p_j)^2$, $\hat{t} = (p_i - p_k)^2$ and $\hat{u} = (p_j - p_k)^2$, where p_i and p_j are the four-momenta of the initial-state partons and p_k denotes the four-momentum of one of the final-state partons. Alternatively, the matrix element can be calculated from only one of the Mandelstam variables, e.g. $\hat{s} = x_\gamma x_p s$, in combination with the scattering angle in the parton-parton center-of-mass frame, θ^*, by using the following relations [1]:

$$\hat{t} = -\frac{1}{2}\hat{s}\,(1 - \cos\theta^*) \tag{1.16}$$

$$\hat{u} = -\frac{1}{2}\hat{s}\,(1 + \cos\theta^*) \tag{1.17}$$

For massless partons, the center-of-mass scattering angle is given by:

$$\cos\theta^* = \tanh\left(\frac{\eta_1 - \eta_2}{2}\right) \tag{1.18}$$

Since partons are not directly measurable, the pseudorapidities of the jets with the highest transverse energies in the event are again used for η_1 and η_2. It is only possible to determine the absolute value of $\cos\theta^*$ because the originating partons of the two jets can not be distinguished.

It has been shown [17] that samples of events enriched in direct or in resolved photon processes have different angular distributions. This can be understood from the different propagators in the dominant processes. Direct photon processes involve a quark propagator (spin $\frac{1}{2}$), dominantly in the t or the u channel, while the dominant subprocesses in the resolved case have gluon propagators (spin 1) in the t channel. The angular dependence of the cross section is approximately $\propto (1 - |\cos\theta^*|)^{-1}$ for direct processes with a quark propagator and $\propto (1 - |\cos\theta^*|)^{-2}$ for resolved processes with a gluon propagator. The cross section for resolved processes thus rises more steeply at high $|\cos\theta^*|$ than that for direct processes.

[5] The pseudorapidity $\eta = -\ln\left(\tan\frac{\theta}{2}\right)$ is often used in preference to the polar angle θ.

[6] The definition of x_γ in terms of the jets is used throughout this thesis. The superscript "obs" will be omitted in the following.

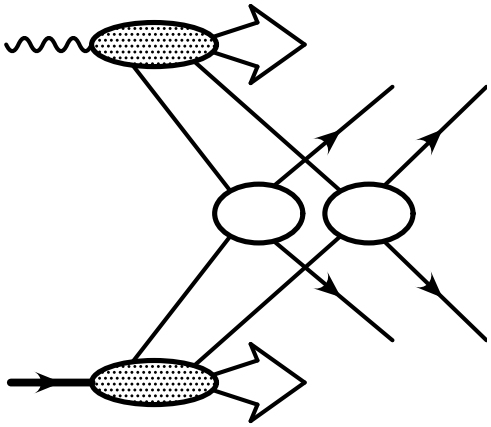

Figure 1.5: Illustration of MPI in resolved photoproduction.

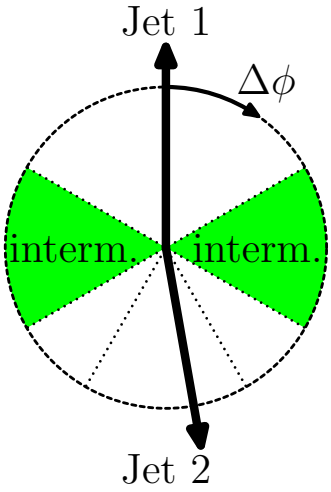

Figure 1.6: Illustration of the intermediate region defined by the azimuthal angle relative to the leading jet.

1.3 Multiparton Interactions

When two hadrons collide, the possibility exists that more than one pair of partons will interact. These multiparton interactions (MPI) could become significant especially in regions of small momentum fractions x of the hadrons, where the density of partons is high.

At HERA, MPI can occur in resolved γp interactions [18, 19] as illustrated in figure 1.5. Events from direct photoproduction cannot contain any MPI because the point-like component of the photon does not posses the additional particles for secondary collisions.

Since the p_T^2 scale is a good measure for the hardness of an interaction, it is interesting to study the differential partonic cross section $d\sigma/dp_T^2$. The hard-scattering partonic cross section above some $p_{T,\min}$ is given by:

$$\sigma^{\text{hard}}(p_{T,\min}) = \int_{p_{T,\min}^2}^{s/4} \frac{d\sigma}{dp_T^2} dp_T^2 \tag{1.19}$$

A lower bound for $p_{T,\min}$ has to be introduced because the calculated differential cross section diverges roughly like $1/p_T^4$ and, in consequence, σ^{hard} is also divergent for $p_{T,\min} \to 0$. A crucial fact is that $\sigma^{\text{hard}}(p_{T,\min})$ reaches the level of the total hadronic cross section, σ^{tot}, already for relatively high values of this lower bound ($\approx (1.5 - 2.0)$ GeV at present collider energies, i.e. $p_{T,\min} \gg \Lambda_{\text{QCD}}$) [20]. The ratio of both cross sections is interpreted as the

average number of parton-parton interactions per hadron-hadron collision:

$$\langle N_{\mathrm{MPI}} \rangle = \frac{\sigma^{\mathrm{hard}}(p_{T,\mathrm{min}})}{\sigma^{\mathrm{tot}}} \tag{1.20}$$

MPI are still not well understood. In fact, next-to-leading-order QCD calculations, e.g. for photoproduction at HERA, lead to a maximum of three partons in the final state, two of which will typically end up in the hard dijet system. Since a complete modeling of MPI clearly requires more than the remaining one parton, the present QCD calculations are not usable. Phenomenological models employing parton showering algorithms that populate the final state are therefore used. These models are are based on several assumptions and unknown parameters. The probabilities for the different pairwise interactions to take place are typically assumed to be uncorrelated. The number of MPI in one event is then given by a Poissonian distribution. Hadrons are not only composite but also extended objects, and the average number of interactions should be larger in central than in peripheral collisions. This can be taken into account, for example, by modifying the width of the Poissonian according to the impact parameter and the assumed matter distribution inside the colliding hadrons. The MPI that occur within one event should be correlated by momentum and flavor conservation, color connections and quantum-mechanical interference effects.

It might be useful to classify the MPI into "soft" and "hard" according to the energy flow generated by the secondary scatters. In this thesis, MPI are considered as hard only if they lead directly to the formation of additional jets in the final state. Soft MPI, in contrast, are expected to be relatively frequent and to influence the appearance of an event more subtly. They may affect jet cross sections as well, since it is not possible to uniquely determine the origin of the final-state particles, and the energy flow stemming from the soft scatters often will be convoluted into the jets from the primary interaction. Soft MPI are the dominant part of the so-called "underlying event", which is a general term describing all hadronic activity not coming directly from the primary hard interaction.

Different approaches are possible to study the physics of MPI. For hard MPI, the most obvious approach is to look for multi-jet states. The first strong evidence for MPI was reported by the CDF Collaboration at the $p\bar{p}$ collider TEVATRON in an analysis of this kind [21]. The effect of MPI on multi-jet states has also been measured in photoproduction at HERA [22]. The energy pedestal caused by the underlying event has also already been studied in HERA data (cf. e.g. [23]). In order to explicitly study soft MPI, it is necessary to conceive special methods for separating the energy flow stemming from the primary and from the secondary interaction. At CDF, this is done using charged tracks in different regions in the azimuth-pseudorapidity space defined with respect to the direction of the leading jet (see [24] and references therein). In events with two jets that are roughly back-to-back and of almost transverse energies, such that the effects of initial-state radiation (ISR) and final-state radiation (FSR) should be minimized, and without further jets above a given threshold, the region between the two jets[7] is of particular sensitivity to

[7]In CDF analyses, the term "transverse" region is typically used. However, the name "intermediate"

soft MPI. This approach, illustrated in figure 1.6, was also chosen for the analysis presented in this thesis.

region was chosen for this thesis to avoid confusion in the nomenclature when referring to the transverse energy in the different regions.

Chapter 2

Experimental Setup

2.1 DESY and the HERA Accelerator

The "Deutsches Elektronen Synchrotron" (DESY) is one of the leading particle accelerator centers in the world. It is member of the German Helmholtz Association of large-scale research facilities. HERA, the "Hadron-Elektron-Ring-Anlage" situated in Hamburg, is DESY's current flagship. In the following, design and performance of the HERA accelerator complex [25], shown in figure 2.1, are briefly described.

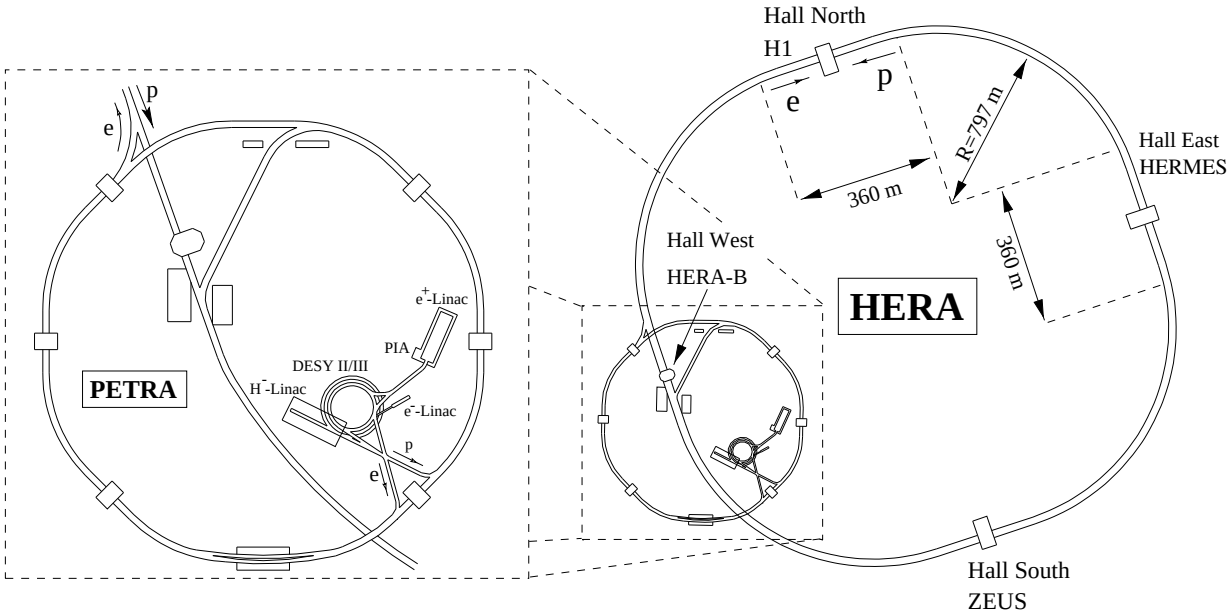

Figure 2.1: Schematic layout of HERA and its pre-accelerator system.

The first collisions of electrons and protons at HERA were registered in October 1991, physics operations began in May 1992. The accelerator can switch between electron and positron modes by reversing its magnet polarities and performing minor changes to the optics.

Both leptons and protons pass through several pre-accelerators prior to their injection into HERA:

- For the hadron beam, H^- ions are brought to an energy of 50 MeV with a linear accelerator (linac) before the two electrons are separated by a stripper foil. The bare protons subsequently are transferred into the synchrotron DESY III and later into PETRA, a ring accelerator owing its name ("Positron-Elektron-Tandem-Ring-Anlage") to its former use as an e^+e^- collider. From PETRA, the protons are injected at an energy of 40 GeV into HERA. There they reach their final energy, which in the first years was 820 GeV and since 1998 is 920 GeV. The maximum proton energy is limited by the strength of the magnets that are used to guide the beam.
- The leptons are brought to energies of up to 450 MeV with linacs. While electrons can be produced directly using an electron gun, positrons have to be obtained from pair production via electron bremsstrahlung in a tungsten target. The accumulator ring PIA allows collecting the required number of particles prior to further acceleration. The leptons are transferred into DESY II and PETRA successively. They are injected into HERA at an energy of 12 GeV. The final lepton energy is 27.5 GeV. It is limited by energy loss due to synchrotron radiation.

The two counter-rotating beams circulate in the HERA tunnel, which is located $(15-30)$ m below ground level, has a circumference of 6.3 km and consists of four 90° arcs joined by 360 m long straight sections. Protons and leptons travel in separate beam pipes, each of which can contain up to 210 bunches of more than 10^{10} particles. They have a revolution frequency of $4.73 \cdot 10^4\,\mathrm{s}^{-1}$.

Besides the center-of-mass energy, the main parameter of a collider is its luminosity $\mathcal{L}$, which correlates the event rate $\mathcal{N}$ of a given process with the cross section σ of this process:

$$\mathcal{N} = \sigma\mathcal{L} \tag{2.1}$$

HERA's luminosity can be calculated from the collision frequency f (i.e. the product of the number of colliding bunches and their revolution frequency), the number of particles in each lepton and proton bunch N_e and N_p, respectively, and the beam profile A at the interaction point:

$$\mathcal{L} = f\frac{N_e N_p}{A} \tag{2.2}$$

Instantaneous luminosities of around $1.5 \cdot 10^{31}\,\mathrm{cm}^{-2}\mathrm{s}^{-1}$ were reached until the year 2000. The accelerator and the affiliated detectors were then upgraded during a longer shutdown

year	collisions	E_e [GeV]	E_p [GeV]	E_{CM} [GeV]	L_{HERA} [pb^{-1}]	L_{ZEUS} [pb^{-1}]
1996	e^+p	27.5	820	300	17.2	10.8
1997	e^+p	27.5	820	300	36.4	27.8
1998	e^-p	27.5	920	318	8.1	4.6
1999	e^-p	27.5	920	318	17.1	12.1
1999	e^+p	27.5	920	318	28.5	19.6
2000	e^+p	27.5	920	318	66.4	45.4

Table 2.1: Type of collision, particle energies, center-of-mass energy, integrated luminosity delivered by HERA and integrated luminosity made available by ZEUS for physic analyses in selected running periods.

with the aim of significantly increasing the luminosity[1] (goal reached after initial problems). For practical reasons, the term luminosity will refer in the following to the luminosity integrated over the time:

$$L = \int \mathcal{L}(t)\ dt \tag{2.3}$$

There are four experimental halls along the HERA ring. The interactions of the colliding beams are measured by two multipurpose detectors covering almost the full solid angle: H1 [26] and ZEUS. In addition, there are two fixed-target experiments: HERMES [27] and HERA-B[2] [28].

Luminosities delivered by HERA and recorded by ZEUS during the running periods relevant for this thesis are listed in table 2.1 together with other important parameters.

2.2 The ZEUS Detector

The ZEUS detector is located in the southern experimental hall at HERA. It was designed for the study of high-energy lepton-proton scattering. Figure 2.2 illustrates size and arrangement of its main components. The detector is almost hermetic, with only the beam pipes breaking the full coverage. The asymmetry along the beamline reflects the large momentum imbalance between incident leptons and protons.

The coordinate system in ZEUS is right-handed and has its origin at the nominal interaction point. The z-axis is pointing in the proton beam direction, called the "forward" direction, and the x-axis is pointing towards the center of HERA. In polar coordinates, r is the distance to the beamline, the azimuthal angle ϕ is measured with respect to the x-axis and the polar angle θ with respect to the z-axis.

[1] In addition, the possibility of lepton-beam polarization was implemented.
[2] HERA-B stopped data taking in the year 2003.

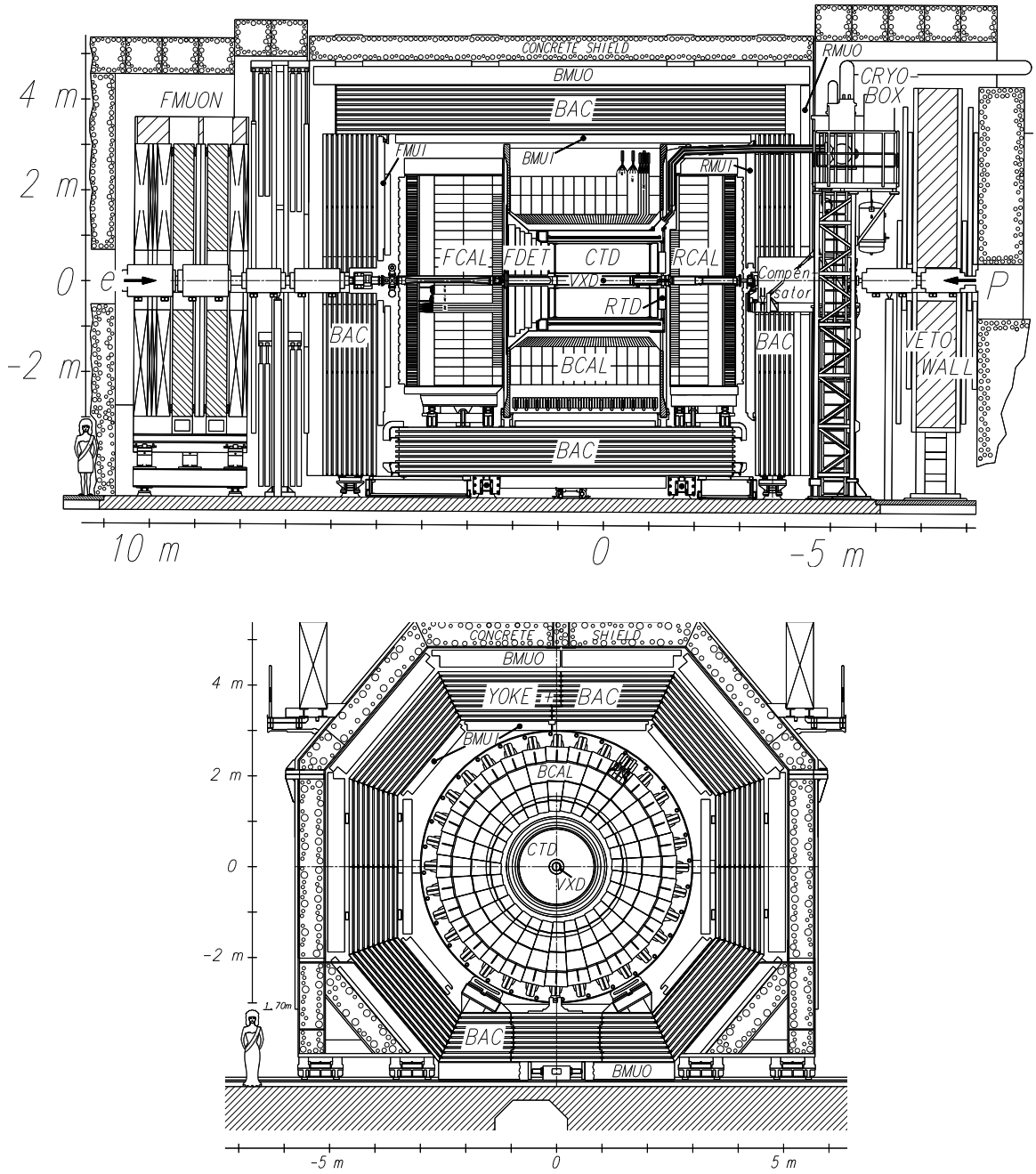

Figure 2.2: Drawing of the ZEUS detector in the (y, z)-plane (top) and in the (x, y)-plane (bottom).

A detailed description of the ZEUS detector can be found in [29]. The most important components, namely the central tracking detector (CTD), the uranium-scintillator calorimeter (CAL), the luminosity monitor and the trigger and data acquisition system, will further be discussed, always referring to the state of the detector in the period during which the data analyzed in this thesis were taken.

2.2.1 The CTD

The CTD is a cylindrical multi-wire chamber dedicated to the detection of charged particles. Its active volume is located in the region specified by $-100\,\text{cm} < z < 105\,\text{cm}$ and $18.2\,\text{cm} < r < 79.4\,\text{cm}$. The polar angle coverage is $15^\circ < \theta < 164^\circ$, i.e. $|\eta| < 2.0$.

The CTD has 4608 sense wires. They are arranged in 72 radial layers, which are grouped into nine so-called superlayers. Five of the superlayers have their wires parallel to the beam pipe. These are alternated by four superlayers that contain wires having a small angle with respect to the beam pipe ($\sim \pm 5^\circ$) in order to facilitate a more precise reconstruction of space points. The CTD contains 19584 field wires, which provide a uniform electric field, and it is surrounded by a superconducting solenoid providing a magnetic field of 1.43 T. The chamber is filled with a gas mixture composed of argon, ethane and carbon dioxide.

The relative transverse-momentum resolution for tracks crossing all nine superlayers of the CTD is $\sigma(p_T)/p_T = 0.0058 p_T \oplus 0.0065 \oplus 0.0014/p_T$ with p_T in GeV and where $\oplus$ symbolizes the summation in quadrature [30].

2.2.2 The CAL

The high-resolution calorimeter, located outside the superconducting solenoid, is made of plates of depleted uranium interleaved with plastic scintillator layers. The thicknesses of the plates of absorbing uranium (3.3 mm) and scintillating material (2.6 mm) were chosen such that the CAL is compensating, which means the response to electrons and hadrons is equal when the initiating particles have the same energy.

The CAL consists of three parts: forward (FCAL) covering $4.3 > \eta > 1.1$, barrel (BCAL) covering the central region $1.1 > \eta > -0.75$ and rear (RCAL) covering the backward region $-0.75 > \eta > -3.8$. Together they cover 99.7% of the solid angle. The structure of the three CAL components is similar. They are segmented longitudinally into one inner electromagnetic and either one (in the RCAL) or two (in the BCAL and FCAL) outer hadronic sections and subdivided transversely into towers with a base area of typically $5\,\text{cm} \times 20\,\text{cm}$ in the electromagnetic and $20\,\text{cm} \times 20\,\text{cm}$ in the hadronic sections. Electromagnetic towers in the BCAL are near-projective in θ, while all other towers are non-projective. The towers are read out by photomultipliers via wave length shifter bars and light guides.

The relative energy resolutions of the CAL are $\sigma(E)/E = 0.18/\sqrt{E} \oplus 0.01$ for electrons and $\sigma(E)/E = 0.35/\sqrt{E} \oplus 0.02$ for hadrons (E in GeV) [29].

2.2.3 Luminosity Monitor

For processes with well-known cross sections, measuring the corresponding event rates allows to determine the luminosity according to equation 2.1. In ZEUS, this is done by monitoring the rate of the lepton-proton bremsstrahlung $ep \to e\gamma p$ (Bethe-Heitler process). The photon from this process is typically emitted under a small angle and detected in a lead-scintillator calorimeter placed in the HERA tunnel at $z = -107\,\mathrm{m}$.

2.2.4 Trigger System and Data Acquisition

The time between bunch crossings in the HERA accelerator is 96 ns, which corresponds to a frequency of slightly more than 10 MHz. Despite the high vacuum in the beam pipes and although the experiments are located underground, event rates in the detectors are largely dominated by beam-gas interactions and cosmic rays. In order to efficiently select interesting lepton-proton events while achieving the maximum background rejection, a fast decision instance that accepts or rejects events is needed. Such a system is commonly called trigger. The ZEUS experiment employs a three-level trigger system. At each trigger stage, a decision is made whether an event is passed on for further analysis or not. Events are finally written to tape with a rate of a few Hz. A diagram of the ZEUS trigger environment can be found in figure 2.3.

For every bunch crossing, all data taken by ZEUS are stored in pipelines for $\sim 5\,\mu$s. The first level trigger (FLT) operates only on a subset of the full data. Each subdetector that is participating in the FLT completes its internal calculations and passes information for a particular bunch crossing to the global first level trigger (GFLT) within roughly $2\,\mu$s. The GFLT calculations take another $2\,\mu$s. The use of pipelines makes ZEUS deadtimeless, accepting new data every 96 ns.

A "GFLT accept" signal causes data to be transferred from the detector components to buffers for processing by the second level trigger (SLT). The input rate at this stage is reduced already to below 1 kHz. Like at the first trigger stage, different detector components have their own SLTs, which pass their information to the global second level trigger (GSLT). In contrast to the FLT, the SLT is able to perform iterative calculations and to access a large fraction of the full data for the event.

Following acceptance by the GSLT, each component passes its data via the event builder to the third level trigger (TLT). The input rate at this stage is below 100 Hz. For the TLT, a reduced version of offline analysis code runs on a computer farm. The event rate has to

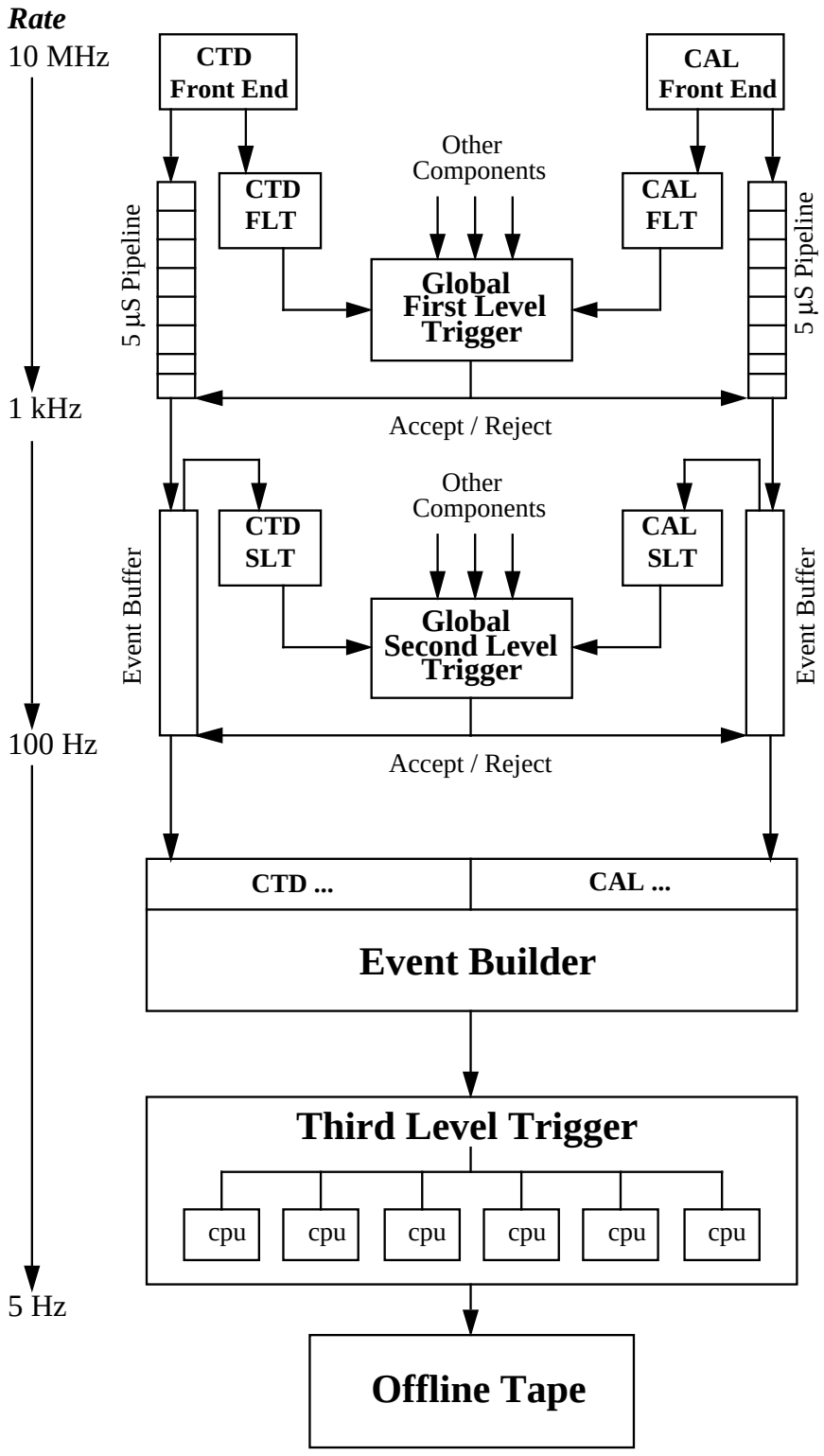

Figure 2.3: Data flow through the ZEUS trigger system.

be reduced to $\sim 5\,\mathrm{Hz}$ before the data are written to mass storage units.

Chapter 3

Event Simulation

Processes in high-energy particle physics are typically simulated using Monte Carlo (MC) techniques, which means that random-number generators are utilized to select variables according to probability distributions. In this chapter, the layout of a generic event simulation is depicted, before PYTHIA, the most important generator for the analysis presented here, and the MC samples used in the thesis are described.

3.1 General Layout

The difficult task of simulating events in high-energy physics is faced by factorizing the problem into several components, which correspond to different - though correlated - physical aspects. This is schematically shown in figure 3.1. The calculation of the different aspects is typically not performed by one single program.

Partons entering the hard scattering are derived from beam hadrons or photons using PDFs. The Q^2 dependence of PDFs is accounted for by evolution equations. The spectrum of photons is derived from the lepton beam (cf. equation 1.10). ISR of the hadronic part of the event is approximated using parton showering methods. The hard interaction of two fundamental particles is calculated from the matrix element of the respective Feynman diagrams. It is this hard scattering that determines the main characteristics of the event. Therefore, most generators start by calculating the hard interaction and handle ISR within backwards evolution. In addition to the hard primary interaction, the possibility of interactions between other partons has to be taken into account. These secondary scatters may be simulated by means of phenomenological models. FSR is approximated using again parton showering methods. Due to the QCD confinement, only color-neutral objects are allowed in the final state. A hadronization model that properly takes into account all color correlations, not only for the newly produced quarks and gluons but also for the remnants

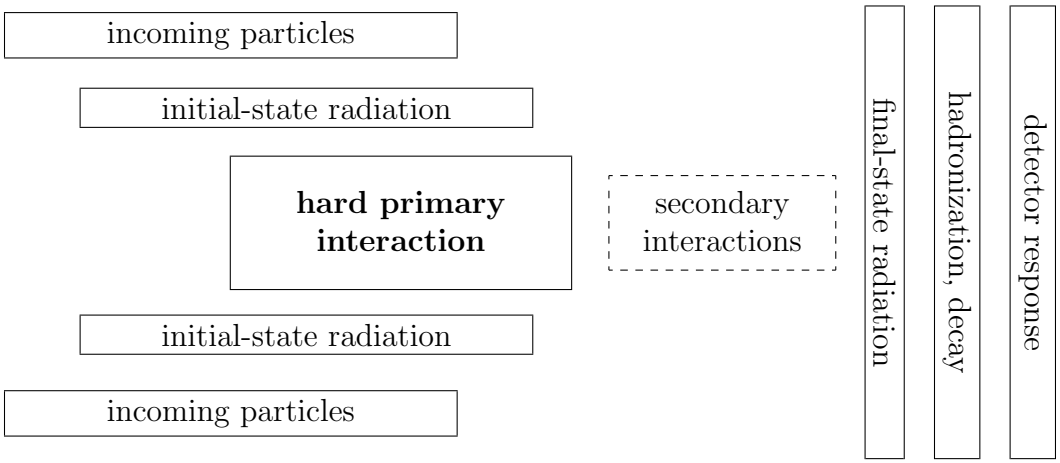

Figure 3.1: Simplified visualization of different aspects in the simulation of a generic generic particle collision.

of the incoming beam particles, is therefore needed. Furthermore, it has to be considered that all unstable particles might decay within the detector.

In order to make the MC prediction comparable to the measured data, the response of the detector has to be simulated for each event. The geometry of the detector, the effect of inactive material and the performance of all relevant subdetectors and of the trigger system have to be modeled.

3.2 The PYTHIA Generator

PYTHIA [31, 32] is an event generator for lepton-lepton, hadron-hadron and lepton-hadron interactions. It uses the Lund string model [33] for hadronization. ISR and FSR are simulated by space-like and time-like parton showers, respectively, starting the calculation from the hard interaction. These showers are ordered with respect to the virtuality of the branching[1], which is related to the mass or transverse momentum of the branching. They begin at some Q^2_{max}, determined from the kinematics of the hard interaction, and evolve down to Q^2_{min}, typically around $1\,\text{GeV}^2$. The parameters `PARP(67)` and `PARP(71)` are provided for adjusting the factor by which Q^2_{hard} is multiplied to set Q^2_{max} in ISR and FSR, respectively.

PYTHIA offers different models for simulating MPI, all based on the first detailed model that was presented [20]. The so-called "simple model" assumes the same probability for MPI in all events, deduced from a simple Poissonian, and an abrupt $p_{T,\text{min}}^{\text{MPI}}$ cut-off. Other

[1]The option of transverse-momentum-ordered instead of virtuality-ordered showers has been introduced recently [32].

models account for varying impact parameters and assume a single or double Gaussian matter distribution in the hadrons and a continuous turn-off of the cross section. Unfortunately and for technical reasons only[2], these more sophisticated models have not been implemented for γp physics in PYTHIA, even in the most recent version [32]. Yet in the simple model, a slow energy dependence of $p_{T,\mathrm{min}}^{\mathrm{MPI}}$ as a function of the hadron-hadron center-of-mass energy, at HERA the energy in the system of the proton and the resolved photon, is assumed:

$$p_{T,\mathrm{min}}^{\mathrm{MPI}} = \texttt{PARP(81)} \cdot \left(\frac{W}{\texttt{PARP(89)}} \right)^{\texttt{PARP(90)}} \tag{3.1}$$

This ansatz is inspired by the observed rise of the total cross section as a function of the center-of-mass energy, which increases approximately like $E_{\mathrm{CM}}^{2\cdot\epsilon}$ with $\epsilon \approx 0.08$ and suggests `PARP(90)` $= 0.16$. The parameter `PARP(89)` is a reference energy scale. It could be set to the center-of-mass energy of the colliding particles, but has no physical meaning in itself. It can be seen from equation 3.1, that `PARP(81)` directly gives $p_{T,\mathrm{min}}^{\mathrm{MPI}}$ at $W =$ `PARP(89)` or for `PARP(90)` $= 0$. Two other important parameters are related to the character of the particles produced in MPI: `PARP(85)` sets the probability for two gluons with color connections to the nearest neighbors in momentum space and `PARP(86)` the total probability for two gluons, either as in `PARP(85)` or as a closed gluon loop. The remaining fraction is supposed to consist of $q\bar{q}$ pairs. The three different possibilities for outgoing particles from secondary scatterings were originally assumed to be equally probable, which yields a probability of $\frac{1}{3}$ for each possibility and corresponds to the setting `PARP(85; 86)` $= 0.33; 0.66$. Recently, these parameters have been varied over a wide range. The values of most of the parameters in the MPI models are sensitive to the choice of PDFs.

Table 3.2 shows the default values of the PYTHIA parameters mentioned above. Listed are the values for two different program versions, namely 6.2 [31] and 6.4 [32]. It can be seen that in PYTHIA 6.4 the maximum shower virtuality allowed in ISR was increased by a factor of 4 (to the same scale valid for FSR[3]) and the fraction of gluons with color connections to the nearest neighbors in momentum space was increased drastically. These changes were stimulated mainly by tunes to CDF data (cf. e.g. [24]). It has to be pointed out that these tunes were made for a model with varying impact parameters and a double Gaussian matter distribution, not for the simple MPI model.

3.3 Monte Carlo Samples Used in this Analysis

MC simulations are used mainly for two purposes in this thesis: to correct the data for detector effects and to compare to the measured hadron-level cross section. PYTHIA 6.2

[2]It would be necessary to provide more information for different center-of-mass energies in the γp system and for different components of the photon [34].

[3]This had been the default already in versions prior to PYTHIA 6.2.

parameter	default		unfolding	hadron-lvl.
	vers. 6.2	vers. 6.4	the data	comparison
proton PDF	CTEQ 5L	CTEQ 5L	CTEQ 4L	CTEQ 5L
photon PDF	SaS 1D	SaS 1D	GRV-G LO	GRV-G LO
`PARP(67)`	1.0	4.0	4.0	4.0
`PARP(71)`	4.0	4.0	(d)	(d)
`PARP(81)`	1.9 GeV	1.9 GeV	(d)	1.7 GeV
`PARP(85)`	0.33	0.90	(d)	(d)
`PARP(86)`	0.66	0.95	(d)	(d)
`PARP(89)`	1.0 TeV	1.8 TeV	(-)	(-)
`PARP(90)`	0.16	0.16	0.00	0.00

Table 3.1: Summary of some important parameters in PYTHIA. Listed are the defaults in the program versions 6.2 and 6.4 as well as the settings that were employed in the MC samples used in this thesis for unfolding the data and for the hadron-level comparison. (d) indicates that the default value from PYTHIA 6.2 was used, (-) indicates that this parameter is obsolete due to the setting chosen for another parameter.

[31] is used for the analysis presented here. The ZEUS detector is simulated using a program based on GEANT [35]. In PYTHIA, the $p_{T,\mathrm{min}}$ of the hard interaction, `CKIN(3)`, was set to 2.0 GeV. The other settings that were chosen are shown in table 3.2. While those samples that are used to correct the data for detector effects were generated with the CTEQ 4L [36] parameterization of the proton, the newer CTEQ 5L [37] was employed for the samples used for the hadron-level comparison. In both cases, the GRV-G LO [38] parameterization was used for the photon. Direct and resolved photoproduction were simulated separately. The respective samples that were used to unfold the data are combined in the ratio that gives the best fit to the x_γ distribution in the data. However, the direct and resolved samples used to compare to the measured cross sections are combined according to the ratio predicted by PYTHIA.

In addition, a DIS sample generated with ARIADNE [39] and the CTEQ 5D [37] parameterization of the proton is used for the estimation of high-Q^2 background.

Chapter 4

Event Reconstruction

Within ZEUS, photoproduction events are defined through the requirement that the scattered electron is not detected in the CAL. As a consequence, the kinematic reconstruction relies completely on the detection of the hadronic final state. A reliable method of electron identification and the accurate measurement of energy deposits belonging to the hadronic final state are thus of great importance for photoproduction analyses.

4.1 Electron Identification

In this thesis, electrons are identified offline using the SINISTRA electron finder [40]. This identification algorithm uses a neural network approach and the information from the CAL. Electrons are separated from single hadrons and jets of particles in a multidimensional configuration space based on their different showering properties in matter. The output of SINISTRA for each event is a list of electron candidates with their respective kinematic properties and a number $0 < \mathfrak{p}_e < 1$ that represents the individual electron probability of the candidate.

4.2 Energy Flow Objects

The hadronic final state is reconstructed from energy flow objects (EFOs) that are formed from a combination of tracking and calorimeter information [41]. This approach optimizes the resolution of kinematic variables and the one-to-one correspondence between detector-level objects and hadrons. The use of tracking information reduces the sensitivity to energy losses in inactive material in front of the CAL and exploits the good resolution of the ZEUS tracking system for low-momentum particles. CAL information is indispensable

for particles for which no track information is available (e.g. neutral particles) and at high particle energies, where the CAL resolution is better than that of the tracking. The energies measured in the CAL can be corrected for energy losses in inactive material by analyzing neutral current DIS events and balancing the scattered lepton with the hadronic final state [42]. The thus corrected EFOs are used in the offline analysis both to determine kinematic variables and for the reconstruction of jets. In this thesis, EFOs in the range $-3.8 < \eta < 4.3$ are taken into account, which corresponds to the coverage of RCAL, BCAL and FCAL.

4.3 The Jacquet-Blondel Method

The Jacquet-Blondel method was originally proposed to reconstruct the kinematics of charged current events, in which an outgoing neutrino remains undetected [43]. It is based on momentum conservation and relies solely on the hadronic final state.

The inelasticity of the photon can be calculated summing over all EFOs i from the hadronic final state:

$$y_{\mathrm{JB}} = \frac{1}{2E_e} \sum_i (E_i - p_{z,i}) \tag{4.1}$$

Figure 4.1 shows the inelasticity reconstructed in this way compared to the true value of the MC generator for photoproduction events. Except for very low and very high values of y_{JB}, the agreement is nearly perfect for direct photoproduction. This confirms the quality of the energy correction applied to the EFOs. In resolved photoproduction, the reconstructed y_{JB} is shifted by about 4% with respect to y_{true}. Nonetheless, it was decided to apply no further corrections to the reconstructed variable.

4.4 Jet Algorithms

Jets are not universally defined objects and different algorithms exist for assigning objects to a jet. Both from a theoretical and from an experimental point of view, a jet algorithm should fulfill several requirements. Two important aspects are infrared safety (the result should not change if an infinitesimally small amount of energy is added to the final state) and collinear safety (the result should not change when replacing two collinear particles by a single one with the same total momentum). These two features are not only significant for the cancellation of divergences in perturbative calculations in QCD; they also guarantee that the final result does not exceedingly depend on the detection of very-low-energy particles from soft radiation and that the result is largely independent of the granularity of the detector.

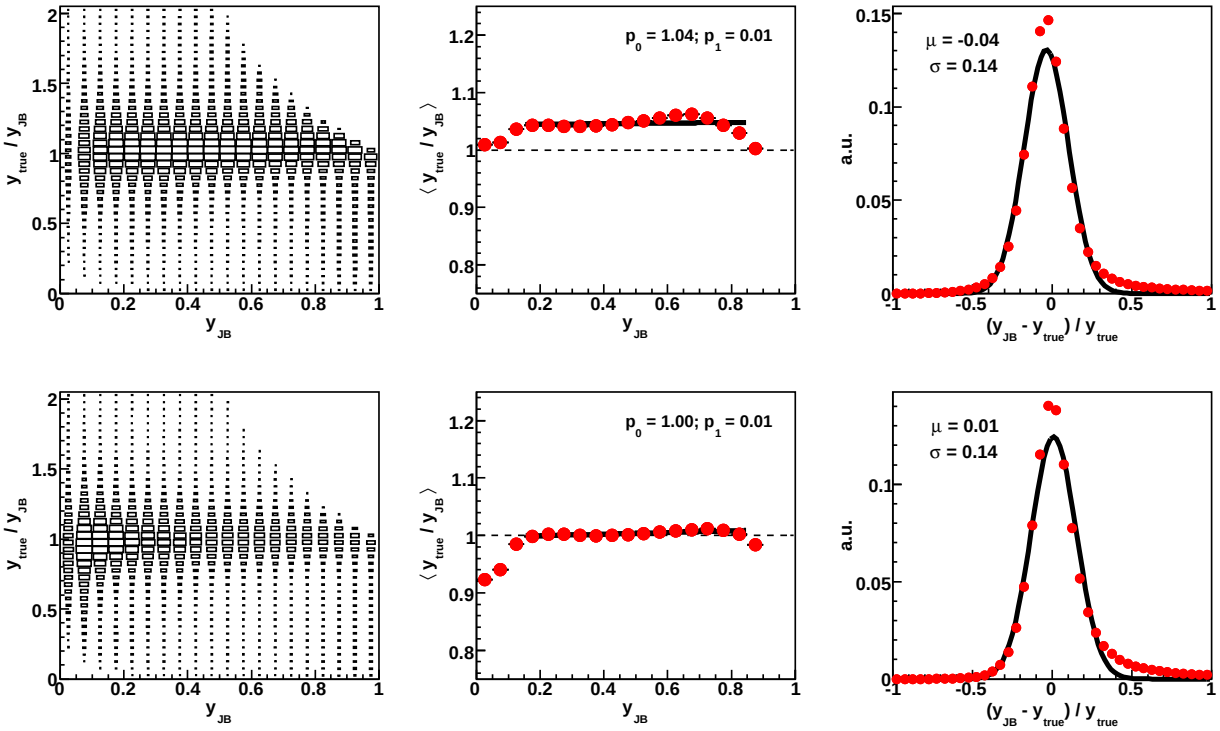

Figure 4.1: Comparison of y_{JB} and y_{true} in MC for resolved photoproduction (upper row) and direct photoproduction (lower row). The mean value of the ratio of both quantities, $\langle y_{\mathrm{true}}/y_{\mathrm{JB}}\rangle$, as a function of y_{JB} is shown in the central column. p_0 and p_1 are the intercept and the slope of a first-order polynomial fitted to the points in the range $0.15 < y_{\mathrm{JB}} < 0.85$. The spread of the underlying distribution is illustrated in the left column. The relative deviation $(y_{\mathrm{JB}} - y_{\mathrm{true}})/y_{\mathrm{true}}$ fitted with a Gaussian can be seen in the right column. μ and σ are the respective mean and variance.

Transverse energy, pseudorapidity and azimuthal angle of a jet are typically calculated according to the Snowmass definitions [44], summing over all objects assigned to the jet[1]:

$$E_{T,\text{jet}} = \sum_i E_{T,i} \tag{4.2}$$

$$\eta_{\text{jet}} = \frac{1}{E_{T,\text{jet}}} \sum_i E_{T,i} \cdot \eta_i \tag{4.3}$$

$$\phi_{\text{jet}} = \frac{1}{E_{T,\text{jet}}} \sum_i E_{T,i} \cdot \phi_i \tag{4.4}$$

In this thesis, jets are considered to be massless. The four-momentum of a jet can then be calculated directly from the above quantities [1]:

$$p = \begin{pmatrix} E \\ p_x \\ p_y \\ p_z \end{pmatrix} = E_T \begin{pmatrix} \cosh\eta \\ \cos\phi \\ \sin\phi \\ \sinh\eta \end{pmatrix} \tag{4.5}$$

The invariant mass of a dijet system, M_{jj}, follows from the four-momenta of the two jets. Equation 4.5 leads to:

$$M_{jj} = \sqrt{(p_1 + p_2)^2} = \sqrt{2\, E_{T,1}\, E_{T,2} \cdot (\cosh(\eta_1 - \eta_2) - \cos(\phi_1 - \phi_2))} \tag{4.6}$$

There are two main types of jet algorithms: cone algorithms and clustering algorithms. In the case of this thesis, a cone algorithm is used by the TLT to select jet events online, while a k_T-clustering algorithm is applied in the subsequent offline analysis.

4.4.1 Cone Algorithms

The idea of cone algorithms is to merge all objects i that are found within a cone of some radius R:

$$R_i = \sqrt{(\eta_i - \eta_{\text{jet}})^2 + (\phi_i - \phi_{\text{jet}})^2} \leq R \tag{4.7}$$

Different approaches are possible concerning the choice of the "seed" with which to begin the jet finding and regarding the handling of overlapping jets. One problem of cone algorithms is that they are not a-priori infrared safe to all orders of α_s.

The EUCELL cone algorithm used at the TLT takes as seeds all regions in the calorimeter where the transverse energy is above a certain threshold. The jet quantities are initially

[1]The subscript "jet" is omitted in this thesis, whenever it can be seen from the context that a variable refers to a jet.

calculated by including all the calorimeter cells contained in a cone centered on the seed. Based on the jet parameters obtained from equations 4.2-4.4, the cells belonging to the jet are newly chosen using equation 4.7. This process is performed iteratively until the resulting values converge (or a maximum number of iterations is reached). Only the jet with the highest transverse energy is accepted. The cells contained within the corresponding cone are excluded from further jet finding to avoid overlapping jets. The whole process is repeated until no seeds with transverse energies above the threshold are found anymore.

4.4.2 Clustering Algorithms

An alternative approach to the reconstruction of jets are clustering algorithms, which successively merge pairs of neighboring objects. These algorithms generally suffer from fewer restrictions than those based on simple cone definitions.

In this thesis, a longitudinally-invariant k_T-clustering algorithm [45] is used in the inclusive mode of Ellis and Soper [46]. To decide which objects should be merged, the following two quantities are calculated for all objects i and all pairs of objects (i, j), respectively:

$$d_i = E_{T,i}^2 \tag{4.8}$$

$$d_{i,j} = \left((\eta_i - \eta_j)^2 + (\phi_i - \phi_j)^2\right) \cdot \min\left(E_{T,i}^2, E_{T,j}^2\right) \tag{4.9}$$

If $d_{k,l}$ is the smallest of all obtained numbers, then objects k and l are combined into a single new object. If d_k is the smallest, then object k is considered to be a jet and it is excluded from further jet finding. This procedure is repeated until all objects are assigned to jets.

4.5 Jet Energy Correction

In order to evaluate the effect of systematic energy mismeasurements, jets on detector level and hadron level are matched in MC events. The matching is done using their distance in the (η, ϕ)-plane:

$$d = \sqrt{(\eta_{\text{had}} - \eta_{\text{det}})^2 + (\phi_{\text{had}} - \phi_{\text{det}})^2} \tag{4.10}$$

To have a well defined sample of properly matched jets, a lower cut on the transverse energy is applied at 3 GeV, $d < 0.5$ is required and pairs in which for the hadron-level jet a second detector-level jet with $d < 1.0$ is found are rejected.

Figure 4.2 shows the mean ratio of the transverse energies of matched jets as a function of E_T^{det} differentially in 13 bins of η. The value of $< E_T^{\text{had}}/E_T^{\text{det}} >$ clearly differs from 1.0 over wide ranges. The mean value of the relative deviation $(E_T^{\text{det}} - E_T^{\text{had}})/E_T^{\text{had}}$ amounts

up to 5% in some regions of the detector (see histogram in the center of the bottom row in figure 4.2). The original energy correction of the EFOs, which were used as input for the jet reconstruction on detector level, seems to have partially the effect of a slight overcorrection. An individual energy correction is therefore performed in this thesis for all jets reconstructed on detector level, using a correction factor that depends on the pseudorapidity as well as on the transverse energy of the jet:

$$E_T^{\mathrm{det}} \rightarrow C(E_T^{\mathrm{det}}, \eta) \cdot E_T^{\mathrm{det}} \tag{4.11}$$

Taking E_T^{had} as the "true" transverse energy of the jet, the correction factor can be obtained from the mean ratio of E_T^{had} over E_T^{det} in the respective bin of E_T^{det} and η. As illustrated in figure 4.2, the trend of this ratio can be approximated by an exponential curve combined with a first-order polynomial:

$$C(E_T^{\mathrm{det}}, \eta) = \left\langle \frac{E_T^{\mathrm{had}}}{E_T^{\mathrm{det}}} \right\rangle = \exp\left(-p_0 \cdot E_T^{\mathrm{det}} + p_1\right) - p_2 \cdot E_T^{\mathrm{det}} + p_3 \tag{4.12}$$

Fits are performed to determine the four parameters of the above function. Figure 4.3 confirms the improvement achieved by this correction procedure. The value of $< E_T^{\mathrm{had}}/E_T^{\mathrm{det}} >$ is shifted towards 1.0 in almost all bins of E_T^{det} and η. The mean value of $(E_T^{\mathrm{det}} - E_T^{\mathrm{had}})/E_T^{\mathrm{had}}$ is smaller than 1% over the whole range of η after the jet energy correction, while the respective variance σ shows no major changes.

Corrected jet energies are used in this thesis for calculating other variables based on jet quantities with the exception of x_γ. Since corrected EFOs are used both for the calculation of the transverse jet energies and for the calculation of y_{JB}, the same energy correction enters in the numerator and in the denominator of $x_\gamma = (E_{T,1}\ e^{-\eta_1} + E_{T,2}\ e^{-\eta_2}) \,/\, \sum (E_i - p_{z,i})$. In this particular case, incorporating an additional jet energy correction could even result in unphysical values ($x_\gamma > 1$). This problem would only be solved by bringing the correction of the EFOs to a grade at which any further jet energy correction becomes unnecessary.

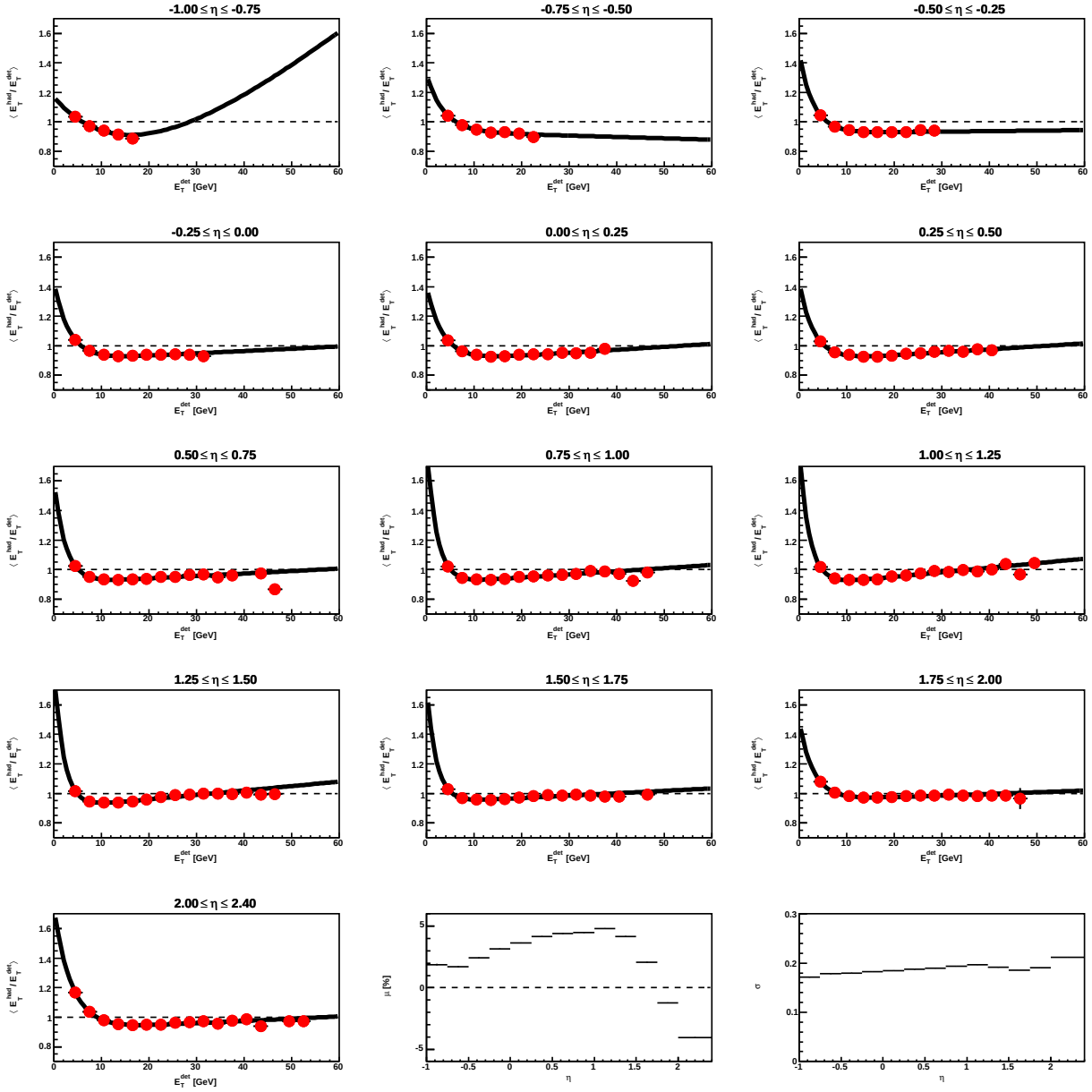

Figure 4.2: Mean ratio of the transverse jet energies on hadron and detector level before the correction of E_T^{det} for 13 different bins of the pseudorapidity, η. See text for a description of the fitted function. The last row contains two histograms showing the mean value μ and the variance σ of the relative deviation $(E_T^{\mathrm{det}} - E_T^{\mathrm{had}})/E_T^{\mathrm{had}}$ as a function of η.

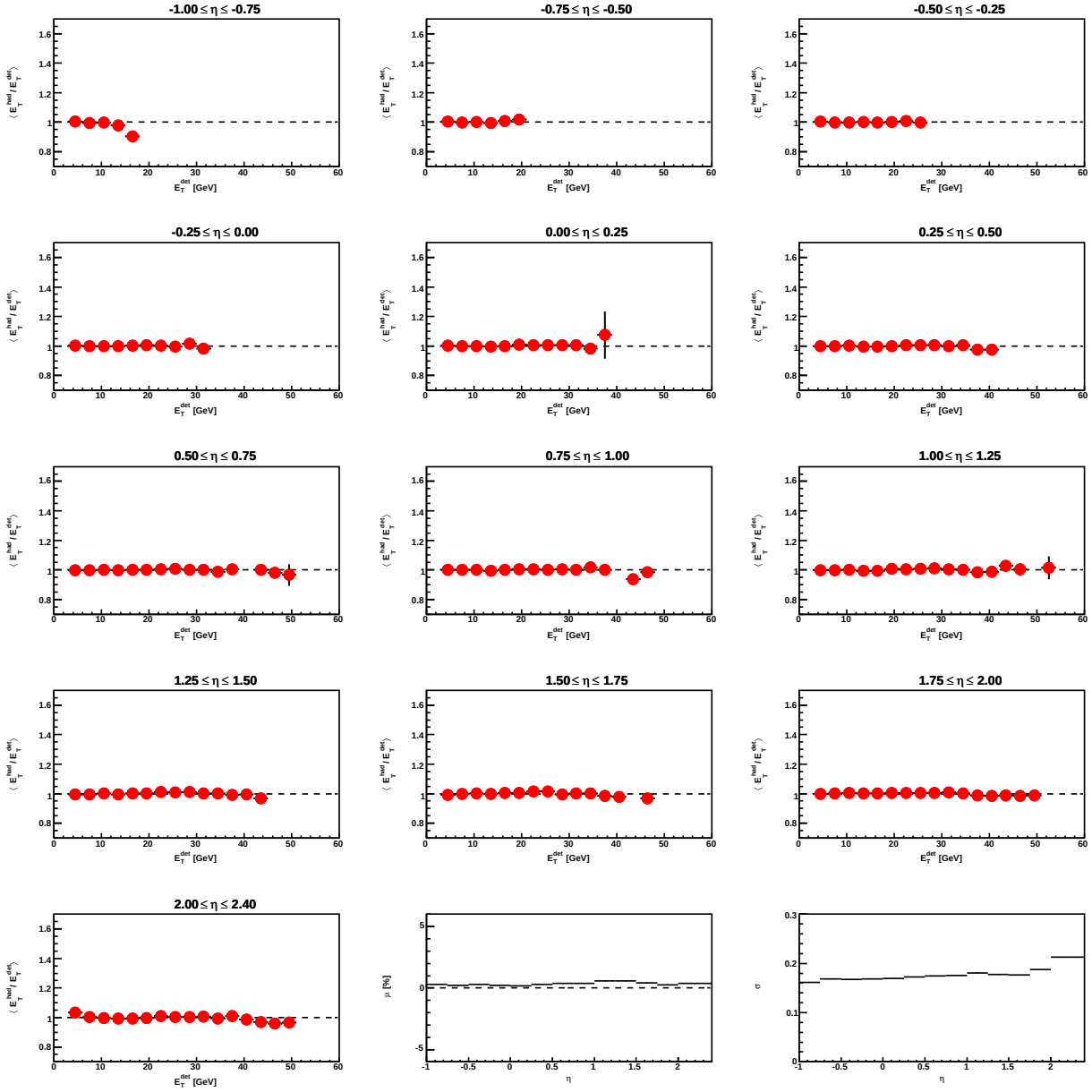

Figure 4.3: Mean ratio of the transverse jet energies on hadron and detector level after the correction of E_T^{det} for 13 different bins of the pseudorapidity, η. The last row contains two histograms showing the mean value μ and the variance σ of the relative deviation $(E_T^{\text{det}} - E_T^{\text{had}})/E_T^{\text{had}}$ as a function of η.

Chapter 5

Event Selection

The data used in the analysis presented here were collected with the ZEUS detector in the period 1998-2000 and correspond to an integrated luminosity of $81.7\,\mathrm{pb}^{-1}$. The general methods used in photoproduction to minimize the contribution of background processes, the actual online and offline event selection criteria of this analysis and the resulting final dijet samples are presented in this chapter.

5.1 Background Rejection Methods

The main processes that are a potential source of background to photoproduction events can be classified into two groups:

- non-ep background originating from beam-gas interactions and cosmic rays
- background from neutral current DIS and charged current DIS

Non-ep background is efficiently rejected by imposing requirements on the reconstructed interaction vertex and on the timing information of the event. Typically a certain number of well-measured tracks is demanded to reconstruct a vertex. For real ep collisions, the distribution of the longitudinal position of the vertex, z_{vtx}, can be approximated by a Gaussian centered around the nominal interaction point at $z = 0\,\mathrm{cm}$, while for beam-gas interactions and cosmic rays the distribution is uniform. Timing information provided by several subdetectors helps to identify events occurring not at the expected time of the bunch crossing and events originating outside the ZEUS detector.

By virtue of energy and momentum conservation, the difference $(E - p_z)$ of the total energy E and the longitudinal momentum p_z of the event is a conserved quantity. In

neutral current DIS, $E - p_z \approx 2E_e = 55\,\text{GeV}$ is observed. In photoproduction, where the scattered lepton escapes undetected along the beam pipe, one finds $E - p_z \approx 2E_\gamma = 2yE_e$, which is typically smaller than 55 GeV. Any cut on $(E - p_z)$ is directly correlated with a cut on y_{JB} and vice versa (cf. equation 4.1). Restricting these two variables to a certain range is a powerful method of discriminating both DIS and non-ep background. The upper cut rejects neutral current DIS events and the lower cut suppresses background from proton beam-gas collisions which have a low value of $(E - p_z)$. The majority of the remaining neutral current DIS events can be identified due to the detection of the scattered lepton. Instead of a lower cut on $(E - p_z)$, an upper cut on the ratio p_z/E is sometimes performed, which has a similar effect.

Charged current DIS events, in which the outgoing neutrino remains undetected, are characterized by missing transverse momentum. Since the incoming lepton and proton beams have no transverse components, the total transverse momentum of the final state, p_T, should be zero in neutral current events. Since the resolution of the detector is finite, a distribution arises, the width of which is assumed to be proportional to $\sqrt{E_T}$. An upper cut on the ratio $p_T/\sqrt{E_T}$ is therefore performed to reject charged current events.

5.2 Online Event Selection

The three-level trigger system of the ZEUS detector is used to select events online. Each level has a number of separate channels called slots. Each slot is designed to accept a particular class of physics events. Those trigger slots that are used in this thesis are described in the following.

5.2.1 FLT

Selection criteria at the first trigger stage are based mainly on global and regional energy sums in the CAL, together with simple tracking requirements from the CTD and vetoes from additional components. In this thesis, FLT slots 42 and 43 are used. In order to select events potentially arising from hard ep processes, they are required to fulfill at least one of the following criteria:

- total energy in the CAL $> 15.0\,\text{GeV}$
- energy in the electromagnetic CAL $> 10.1\,\text{GeV}$
- energy in the electromagnetic BCAL $> 3.4\,\text{GeV}$
- energy in the electromagnetic RCAL $> 2.0\,\text{GeV}$

- transverse energy in the CAL $> 11.6\,\mathrm{GeV}$

In addition, non-*ep* background is rejected by vetoes based on tracking and timing information.

5.2.2 SLT

More detector information and time for more sophisticated algorithms to reconstruct physical quantities are available at the SLT than at the FLT. In this thesis, trigger HPP01 is used to select events at the second level. This slot is dedicated to the selection of high-E_T events from hard photoproduction. It calculates the quantity E_T^{box}, defined as the sum of transverse energy in all CAL cells excluding the first ring around the FCAL beam pipe. Besides requirements on the quality of tracks and the position of the reconstructed vertex, events have to satisfy all of the following three criteria to be selected:

- $E - p_z > 8.0\,\mathrm{GeV}$
- $(E - p_z > 12.0\,\mathrm{GeV})$ or $(p_z/E < 0.95)$
- $E_T^{\mathrm{box}} > 8.0\,\mathrm{GeV}$

5.2.3 TLT

At the TLT, yet more time and information is available. In this thesis, slots HPP02 and HPP15 are used at the third trigger stage. Besides requirements on the quality of tracks, both trigger slots impose these two criteria:

- $|z_{\mathrm{vtx}}| < 60\,\mathrm{cm}$
- $E - p_z < 75\,\mathrm{GeV}$

Both slots use the EUCELL algorithm to find jets. HPP15 is a dedicated dijet trigger. Its specific requirements are:

- at least 2 jets with
  - $(E_T \geq 4\,\mathrm{GeV}$ and $\eta < 1.5)$ or $(E_T \geq 6\,\mathrm{GeV}$ and $\eta < 2.5)$ (1998 - mid 1999)
  - $E_T \geq 6\,\mathrm{GeV}$ and $\eta < 2.5$ (mid 1999 - 2000)
- $p_z/E < 1.0$

The inclusive jet trigger HPP02 is used to increase the efficiency for dijet events in which the second jet was not properly reconstructed, e.g. owing to its position near to boundaries between detector components. HPP02 demands at least one jet with $E_T > 10\,\text{GeV}$ and $\eta < 2.5$ in each event.

5.3 Offline Event Selection

In order to obtain a clean sample of photoproduction events, the following cuts are performed in the offline analysis:

- $|z_{\text{vtx}}| < 40\,\text{cm}$
- $p_T/\sqrt{E_T} < 1.5\,\sqrt{\text{GeV}}$
- $0.20 < y_{\text{JB}} < 0.85$
- no electron candidate with $\mathfrak{p}_e > 0.9$ and $y_e < 0.85$

Just like y_{JB}, the variables p_T and E_T are determined using corrected EFOs. Events with an electron candidate found by SINISTRA are accepted if they have high values of y_e, which is calculated according to equation 1.8, since electrons that are high in y_e are low in energy and come typically from electromagnetic showers or are in fact other particles that were misidentified. Rejecting all events with any electron observed in the CAL would dismiss a significant number of genuine photoproduction events.

To be able to unfold the data to the hadron level, MC sets are required that contain both detector-level information and hadron-level information. In order to restrict the analysis to the same phase space on both levels, an event selection has to be performed at hadron level as well. Instead of the four criteria listed above, the following cuts are applied to the MC events on hadron level:

- $Q^2_{\text{true}} < 1\,\text{GeV}^2$
- $0.20 < y_{\text{true}} < 0.85$

In the offline analysis, the longitudinally-invariant k_T-clustering algorithm is applied to the corrected EFOs for the reconstruction of jets (and to hadrons for the reconstruction of jets on hadron level in MC). The algorithm runs in an inclusive mode, which means that all objects are clustered into jets. To obtain well defined samples with hard jets observed in well understood regions of the detector, the jet finding has to be followed by a jet selection.

	$E_{T,1}$ [GeV]	$E_{T,2}$ [GeV]	N_{jets}	$\Delta\phi_{jj}$	$E_{T,1}/E_{T,2}$
selection 1	> 14	> 11	≥ 2	any	any
selection 2	> 10	> 8	$= 2$	$> 150°$	> 0.75

Table 5.1: Jet requirements used to select events for the final samples.

The selection criteria used in this thesis are:

- $E_T > 5\,\text{GeV}$
- $-1.0 < \eta < 2.4$

In the ZEUS data from 1998-2000, a total of 606494 events pass all cuts and have at least two jets matching the chosen definition.

5.4 Final Samples

Two subsets of the selected dijet events are used for the further analysis. These final samples differ in the requirements imposed on the jets, which are summarized in table 5.1.

The first sample, denoted by "selection 1", is used to calculate cross sections and compare them to cross sections measured by the ZEUS Collaboration with the 1996-1997 data. In consequence, the jet requirements used to select events for this sample are adopted from the already published analysis [47]. Events are chosen in which the transverse energies of the two leading jets (sorted in E_T) lie above 14 GeV and 11 GeV, respectively.

For the second sample, denoted by "selection 2", the cuts on the transverse energies are lowered to 10 GeV and 8 GeV. In addition, only events containing exactly two jets are chosen and these jets are required to be roughly back-to-back in the azimuthal plane and to have almost equal transverse energies. The azimuthal distance of the dijet system is calculated as:

$$\Delta\phi_{jj} = |\phi_1 - \phi_2| \tag{5.1}$$

$\Delta\phi_{jj}$ is demanded to be greater than 150° and the ratio $E_{T,2}/E_{T,1}$ to be greater than 0.75 for this sample. The aim is to study the region between the jets and to estimate the effect of soft MPI, which possibly cause an extra energy flow in the detector but do not give rise to additional hard jets. This sample is sensitive to the actual value of the minimal transverse energy required from each jet candidate to be considered as a hard jet (5 GeV in this thesis), since all events with a third jet above the threshold are dismissed.

The number of events in selection 1 and selection 2 is 94863 and 175052, respectively. The overlap contains 48659 events.

5.4.1 Control Plots

In figures 5.1 and 5.2, control plots for both selections are shown. The direct and the resolved PYTHIA samples were normalized to the number of selected events in the data before the optimal proportion (45% to 48% direct and 55% to 52% resolved) was determined in a χ^2-fit to the x_γ distribution for each selection separately. The prediction of ARIADNE is shown to estimate the contribution of DIS background to the selected events. This MC sample was scaled by the luminosity of the data divided by the luminosity of the MC sample. The contribution of background from high Q^2 events to the final selections is estimated to be below 1%.

Besides kinematic variables of the selected events, jet quantities are shown in the control plots. While for $E_{T,1}$ and $E_{T,2}$ the jets are ordered with respect to their transverse energies, η_F and η_R refer to the pseudorapidities of the most forward and the rear of the two highest energetic jets in the event. The shape of the η_F distribution turns out to be highly dependent on the amount of resolved photon processes contributing to the MC prediction, especially for high values of η_F. The poor description of the $\Delta\phi_{jj}$ distribution by the MC can be understood from the fact that the azimuthal distance of the two leading jets is very sensitive to higher-order processes like FSR and to the adequate simulation of parton showering.

The x_γ distribution is of particular importance for this analysis, since it is used to determine the proportion of direct and resolved photon processes included in the combined MC prediction on detector level. Control plots revealed problems in the description of the data by the MC for low values of x_γ. It was found that the agreement between data and MC could be improved by assigning to each event a factor w that gives more weight to those events from the low-x_γ region. The following reweighting approach was therefore chosen:

$$w = 1 + \frac{a}{x_\gamma^{\text{true}}} \tag{5.2}$$

This reweighting procedure is performed on detector level and on hadron level with the same factor w, but only in the resolved MC sample that is used for unfolding the data ($w = 1$ in all other cases). The optimal reweighting coefficient a is determined in a series of χ^2-fits on detector level to be 0.02 and 0.04 for selection 1 and selection 2, respectively. By comparing figures 5.1 and 5.2 with the respective control plots for $a = 0.00$, which can be found in appendix A, an improvement in the description of the data by the MC can be seen in the x_γ distribution, especially for selection 2. No major changes are observed in the description of the other variables. The agreement between data and MC is within 10% in most bins with significant statistics.

Figure 5.3 shows the transverse energy flow per event as a function of the pseudorapidity. The discontinuity near $\eta \approx 1.0$ is presumably related to the transition between different components of the detector (BCAL and FCAL). The peak around $\eta \approx 3.2$ stems from the

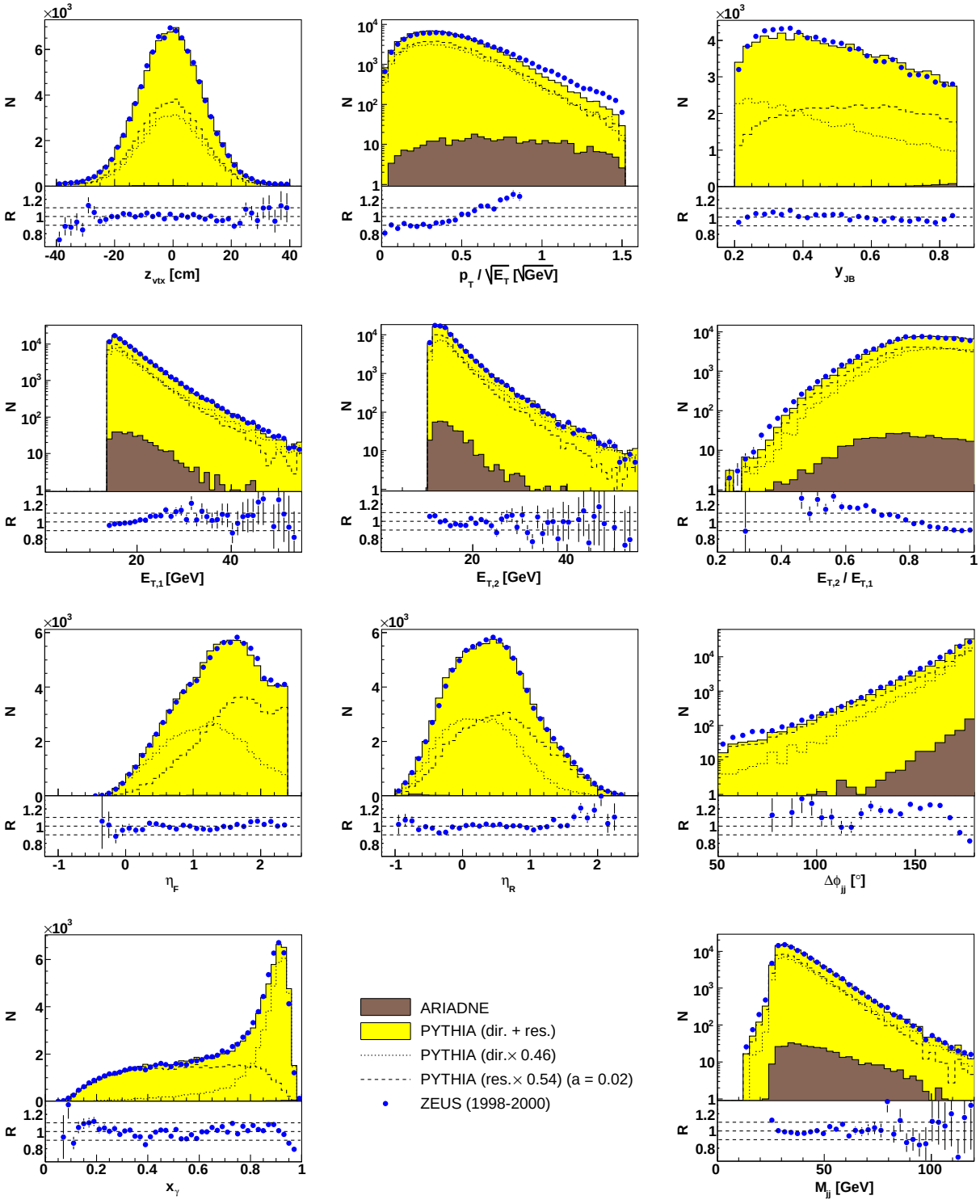

Figure 5.1: Control plots for selection 1 after the reweighting with respect to x_γ^{true}. Shown are the number of selected events N and the ratio R = ZEUS / PYTHIA.

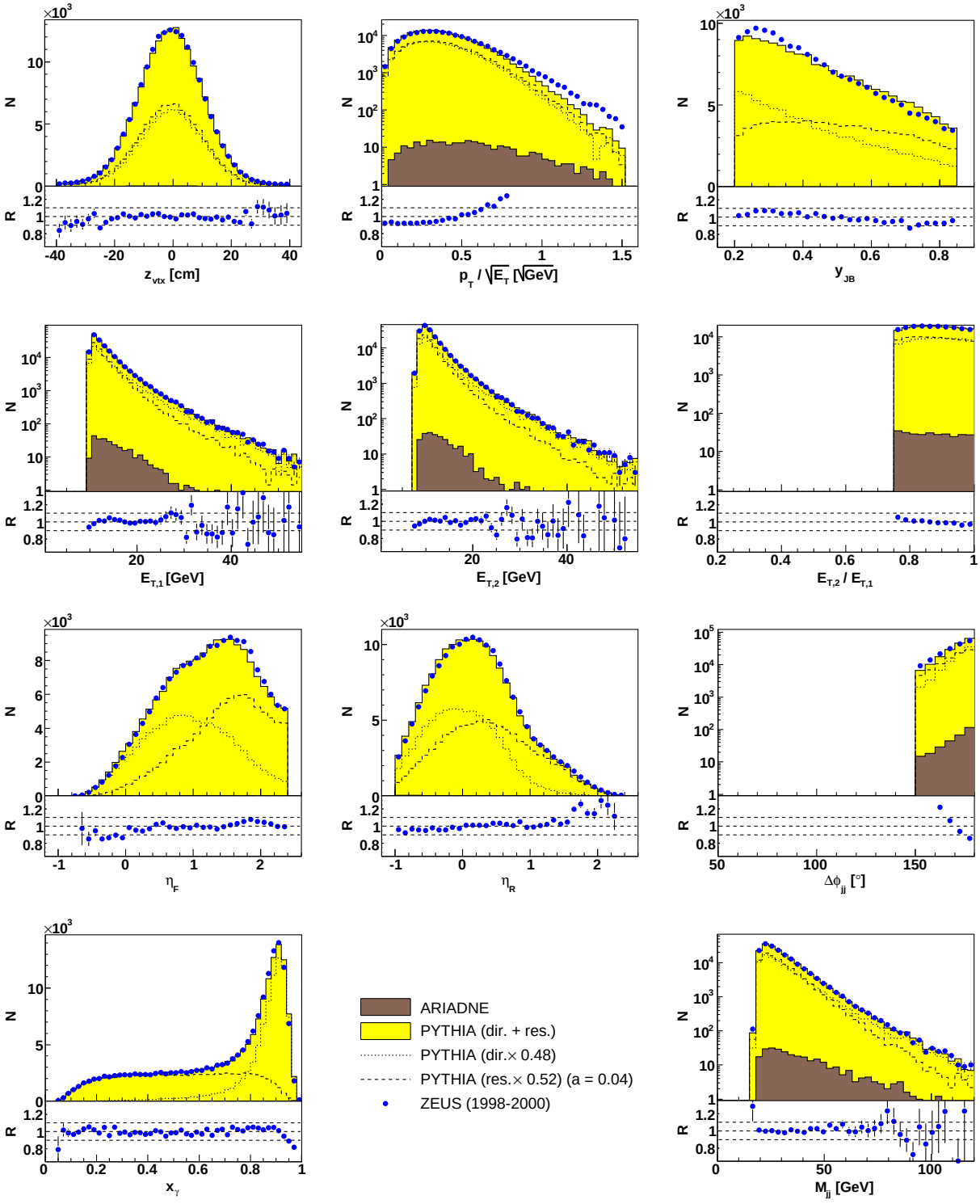

Figure 5.2: Control plots for selection 2 after the reweighting with respect to x_γ^{true}. Shown are the number of selected events N and the ratio R = ZEUS / PYTHIA.

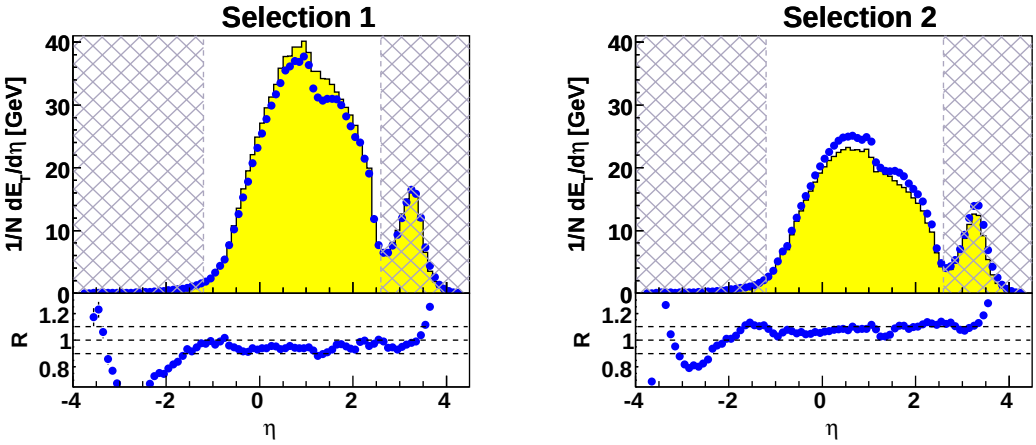

Figure 5.3: Transverse energy flow $dE_T/d\eta$ per event as a function of the pseudorapidity η. The data points correspond to ZEUS 1998-2000 (uncorrected data). The solid line corresponds to the prediction from PYTHIA. In the lower part of the figure, the ratio R = ZEUS / PYTHIA is shown. The crosshatched areas indicate those regions of η that are not taken into account for the calculation of energy flow in the following.

proton remnant. The agreement between data and MC is of the same quality as previously observed in ZEUS analyses with data from the 1996-2000 period. In order to exclude the proton remnant and to minimize the sensitivity to detector regions where the description of the data by the MC is poor, the energy flow will be calculated in this thesis only in the range $-1.2 < \eta < 2.6$.

The transverse energy flow per event as a function of the azimuthal distance to the leading jet is shown in figure 5.4. For selection 2, the resulting distribution is almost flat in the intermediate region between the two jets (cf. section 1.3 and figure 1.6). This is not the case for selection 1, for which the distance of the two leading jets in the azimuthal plane and the ratio of their transverse energies are not subject to restrictions and no upper limit on the transverse energy of any further jet is set, such that a significant amount of energy stemming from the second jet as well as from possible additional jets can be deposited in the intermediate region.

The transverse energy flow in the region between the two jets is used in this thesis to study the physics of MPI. The variable E_T^{int} is calculated as the summed transverse energy of all EFOs in the intermediate region :

$$E_T^{\text{int}} = \sum_i E_{T,i} \qquad \{i \mid 60^\circ < \Delta\phi_{ij} < 120^\circ, -1.2 < \eta_i < 2.6\} \tag{5.3}$$

It can be seen from figures 5.3 and 5.4 that the measured transverse energy flow in the data differs from the MC prediction. However, since this shift is almost constant in the

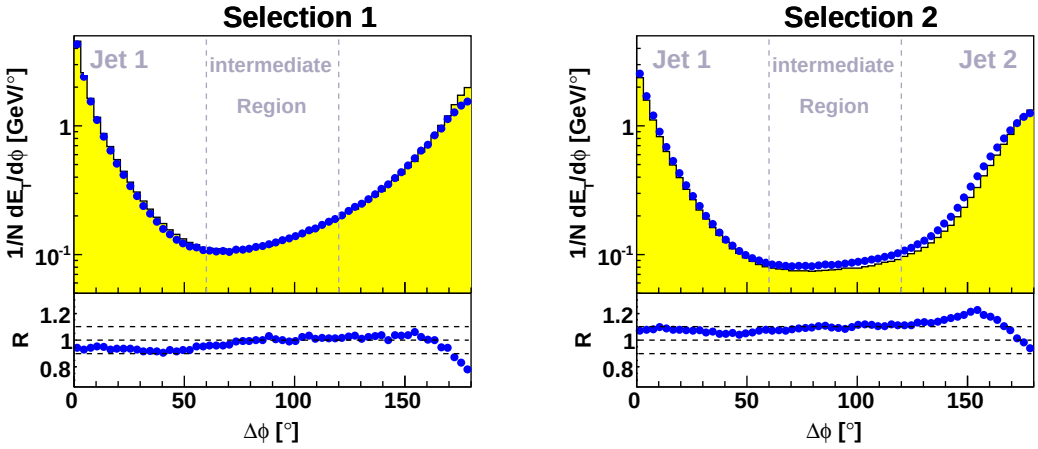

Figure 5.4: Transverse energy flow $dE_T/d\phi$ per event as a function of the azimuthal distance to the leading jet, $\Delta\phi$, in the range $-1.2 < \eta < 2.6$. The data points correspond to ZEUS 1998-2000 (uncorrected data). The solid line corresponds to the prediction from PYTHIA. In the lower part of the figure, the ratio $R =$ ZEUS / PYTHIA is shown. While the position of the second jet in the azimuthal plane is not subject to restrictions for selection 1, it is restricted by $\Delta\phi_{jj} > 150°$ for selection 2.

azimuthal plane, its effect should me minimized by cancellation when regarding the ratio $E_T^{\text{int}}/E_T^{\text{tot}}$ instead of E_T^{int}, where E_T^{tot} is calculated from all EFOs in the azimuthal plane.

5.4.2 Trigger Efficiency

To study the efficiency of the trigger configuration used in the online event selection for this thesis, a data set from the first 50 runs in the year 2000 without a specific trigger preselection is employed. Among a large number of background events from other sources, this data set contains a significant number of events with muons from cosmic showers. Since these cosmic muons typically traverse the detector producing very straight tracks in the CTD, they often lead to high energy EFOs although only little energy is deposited in the CAL. Under certain circumstances, two back-to-back jets are reconstructed and the event passes all criteria of the offline selection, while most trigger would have rejected the event correctly on the basis of timing vetoes or the small energy deposit in the CAL. In order to maximize the purity of genuine photoproduction dijets in the final samples and to reduce the bias in this efficiency study, an additional cut is applied that makes use of the average timing of the upper and the lower halves of the CAL, t_u and t_d, and the amount of energy deposited in the upper and the lower halve, E_u and E_d, respectively:

$$|t_u - t_d| < 6\,\text{ns} \quad \text{and} \quad \min(E_u, E_d) \geq 2\,\text{GeV}$$

The efficiency of the chosen trigger configuration[1] is calculated as the the number of events accepted by this particular trigger configuration and selected in the subsequent offline analysis divided by the number of events accepted by any trigger and passing the offline selection:

$$\varepsilon_{\text{trigger}} = \frac{N(\text{trigger} \wedge \text{offline})}{N(\text{offline})} \tag{5.4}$$

An efficiency below 1.0 indicates that a fraction of photoproduction dijet events that in fact should contribute to the final cross sections is lost owing to the online event selection. The most important question is whether the trigger efficiency is reasonably described by the MC. An inefficiency on detector level would then be compensated by the acceptance corrections performed later on. Nonetheless, the efficiency should never drop too low, since otherwise the calculation of cross sections would be based mainly on extrapolation.

The trigger efficiency is shown in figure 5.5 for the two final samples as a function of the transverse energies of the two leading jets and as a function of their pseudorapidities. The efficiency is high and well simulated for selection 1. In the case of selection 2, the efficiency drops from $\sim 97\%$ to $\sim 78\%$ for small transverse energies and the description by the MC gets poor. This problem is not unequivocally located in η, although the efficiency varies along η_1 and η_2, demonstrating deficits especially in the forward and the rear regions. Despite the observed problems, it was decided not to raise the lower cut on the jet energies for selection 2. However, the discrepancies have to be kept in mind in the further analysis.

5.5 Definition of the Cross Section

Cross section measurements in this thesis are carried out in the kinematic region defined by $Q^2 < 1\,\text{GeV}^2$ and $0.2 < y < 0.85$. The photon-proton center-of-mass energy is restricted thereby to the range $142\,\text{GeV} < W < 293\,\text{GeV}$. The requirements imposed on the jets for the selection of dijet events are described in section 5.4 and summarized in table 5.1.

Differential cross sections are presented as a function of W, x_γ, η_2, M_{jj}, $|\cos\theta^*|$, E_T^{int} and $E_T^{\text{int}}/E_T^{\text{tot}}$. They are shown in different ranges of x_γ, $E_{T,1}$, η_1 or M_{jj}. The cross section $d\sigma/d\eta_2$ in ranges of η_1 is symmetrized with respect to the pseudorapidities of the jets by interchanging the roles of the first and the second jet. In consequence, each event contributes twice to this cross section. This procedure is chosen to minimize the dependence on soft particles related to the ordering of the two hardest jets [48].

Additional kinematic constraints are applied exclusively to the measurement of the cross section as a function of $|\cos\theta^*|$. For a given center-of-mass energy, events with high $|\cos\theta^*|$ have small scattering angles θ^* and thus jets with lower E_T. From equations 4.6 and 1.18,

[1] In this thesis: (FLT 42 $\vee$ 43) $\wedge$ (SLT HPP01) $\wedge$ (TLT HPP02 $\vee$ HPP15).

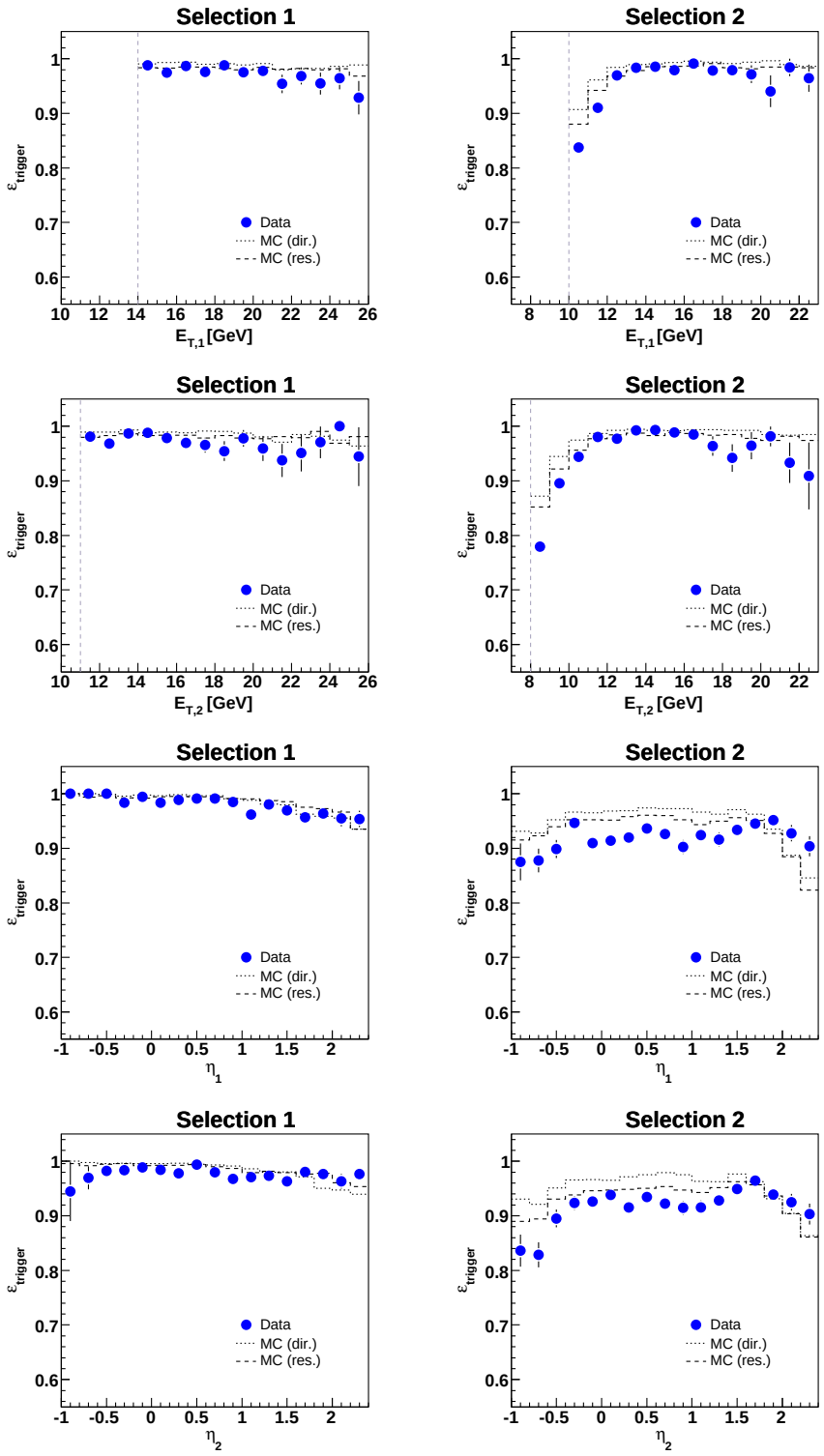

Figure 5.5: Efficiency of the chosen trigger configuration as a function of the transverse energies of the two leading jets and as a function of their pseudorapidities.

the following relation between scattering angle and dijet mass can be derived for jets of equal transverse energy and back-to-back in the azimuthal angle:

$$M_{jj} = \frac{2E_T}{\sqrt{1 - |\cos\theta^*|^2}} \tag{5.5}$$

The minimum accessible dijet mass for a given value of $|\cos\theta^*|$ can be deduced from this equation. For this purpose, the average of the minimum transverse energies of the two jets is taken as the minimum E_T. To study the $|\cos\theta^*|$ distribution up to $|\cos\theta^*| = 0.8$ without bias from the transverse energy cuts at 14 GeV and 11 GeV, a minimum dijet mass of 42 GeV is required. Although E_T cuts at 10 GeV and 8 GeV would allow to relax this requirement, $M_{jj} > 42\,\text{GeV}$ is used for measuring $d\sigma/d|\cos\theta^*|$ both in selection 1 and in selection 2. Furthermore, a cut on the boost of the dijet system, $\bar{\eta} = \frac{1}{2}(\eta_1 + \eta_2)$, of $0.1 < \bar{\eta} < 1.3$ is applied. As a result, the measured cross section as a function of $|\cos\theta^*|$ is not biased by any of the imposed cuts for $|\cos\theta^*| < 0.8$ [47].

Chapter 6

Unfolding the Data

As a result of the limited resolution, acceptance and efficiency of the detector, the measured distributions do not correspond directly to those which represent the processes occurring at the level of final-state hadrons. A detector-level distribution corresponds to the hadron-level distribution folded with some transfer function, which accounts for the response of the detector. In order to study the physics of processes at the hadron level and not detector-specific effects, the measured distributions have to be unfolded. For the unfolding procedure, MC samples are needed that were passed through a full detector simulation and that supply both hadron-level and detector-level information.[1]

The bin-by-bin unfolding, which is used in this thesis, is a simple method for correcting the measured data for detector effects. It is based on the fact that all distributions are measured in discrete bins, and it provides a simple correction factor for each bin. The bin-by-bin unfolding can be performed when the description of the data by the MC is reasonable and when the migrations between bins are not too big.

6.1 Migrations

Migrations between the different bins can described by a matrix in which the element mn represents the number of events that were reconstructed in bin m on detector level and generated in bin n on hadron level. The diagonal elements of this migration matrix contain those events that were reconstructed in the same bin on detector level as generated on hadron level. Rows/columns with the label "0" are used for events that were not reconstructed/generated in any of the bins defined on detector/hadron level or that did not pass the event selection on the respective level. Two examples of migration matrices are shown in figure 6.1, the figures for all variables that were unfolded in this thesis can

[1] Cf. section 3.3 for informations about the MC samples used in this thesis.

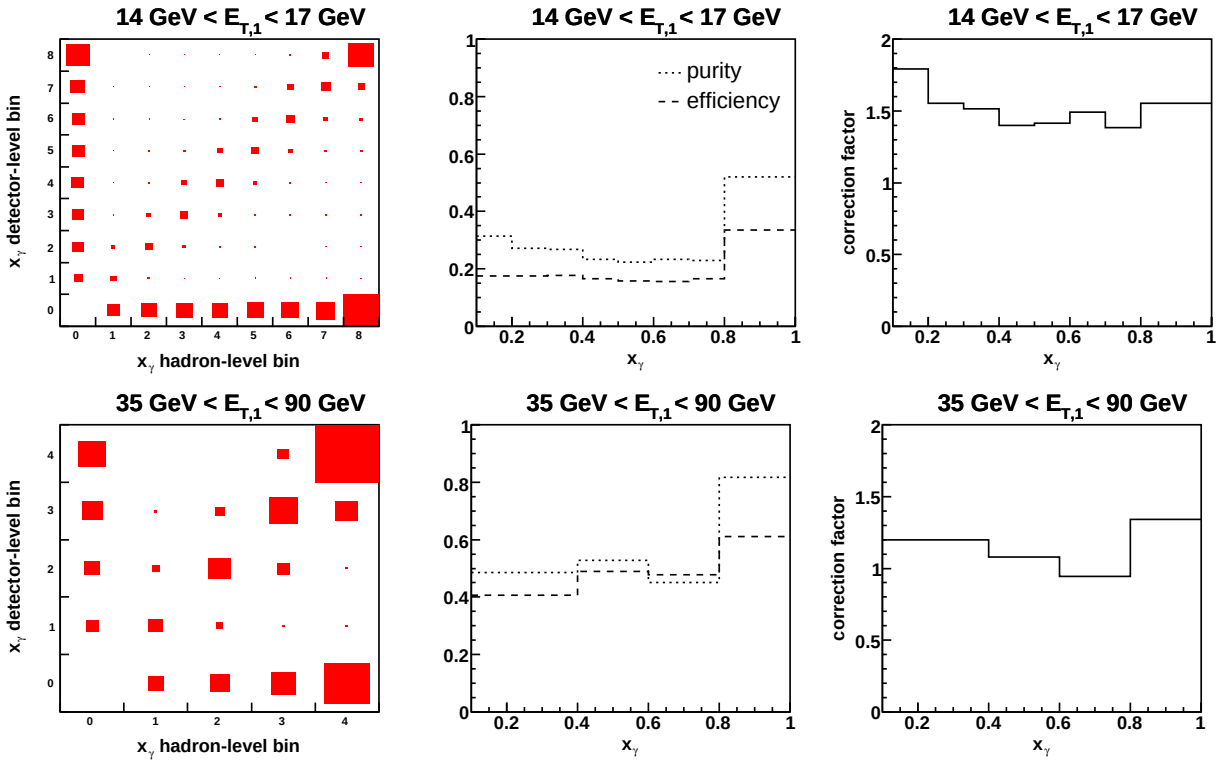

Figure 6.1: Histograms for the unfolding for selection 1 as a function of x_γ in two different regions of the transverse energy of the leading jet, $E_{T,1}$. Shown are the migration matrix (left), the efficiencies and purities (center) and the correction factors (right).

be found in appendix B. Most events are reconstructed in the adequate bin (diagonal elements) or fail at least one of the selection criteria (row or column "0"), while the amount of long-range migrations within the selection is relatively small.

In order to quantify the migration effects, efficiencies and purities can be calculated. For bin i, the efficiency ε_i, which is inversely proportional to the amount of losses into other detector-level bins, is determined from the number of events in the corresponding diagonal element in the migration matrix divided by the number of all events in this bin on hadron level:

$$\varepsilon_i = \frac{N_i(\text{hadron level} \wedge \text{detector level})}{N_i(\text{hadron level})} \tag{6.1}$$

The purity $\mathcal{P}_i$, which is inversely proportional to migrations from other detector-level bins into bin i, is defined analogously, dividing by the number of all events in bin i on detector level:

$$\mathcal{P}_i = \frac{N_i(\text{hadron level} \wedge \text{detector level})}{N_i(\text{detector level})} \tag{6.2}$$

Efficiencies and purities as a function of x_γ in two different ranges of the transverse energy of the leading jet, $E_{T,1}$, are shown in figure 6.1, and the figures for all variables can be found again in appendix B. In this analysis, typical efficiencies and purities are $\varepsilon \approx (15-45)\%$ and $\mathcal{P} \approx (25-60)\%$. They are better in the direct-enriched than in the resolved-dominated region, relatively good in the range of high jet energies and particularly poor in the rear region of the detector, i.e. for small values of η_1 and η_2. The best efficiency and purity, $\varepsilon \approx 60\%$ and $\mathcal{P} \approx 80\%$, are achieved for $x_\gamma > 0.8$ and $E_{T,1} > 35\,\text{GeV}$. The major part of the inefficiencies and impurities seem to be due to the low cuts on the transverse energies of the two leading jets. Increasing the E_T cuts in the event selection would cut into an important part of the kinematic space and quickly reduce the sensitivity to processes like MPI. Poor purities and efficiencies are therefore tolerated in this analysis. However, bins in which efficiency or purity are below 10% are not used for the results presented in this thesis.

6.2 Correction Factors

The correction factors for the bin-by-bin unfolding can be determined from the efficiencies and purities or directly from the number of selected events on detector and on hadron level. For bin i, the correction factor is given by any of the two ratios in the following equation:

$$C_i = \frac{\mathcal{P}_i}{\varepsilon_i} = \frac{N_i(\text{hadron level})}{N_i(\text{detector level})} \tag{6.3}$$

In the following, the unfolded number of events in bin i is calculated by simply multiplying the respective number of selected events in the experimental data with the correction factor C_i determined from the MC simulation.

The correction factors for the whole unfolding procedure in this thesis can be found in appendix B, two examples in figure 6.1. The correction factors are typically greater than 1.0 in this analysis, since the purity is better than the efficiency in almost all bins.

Chapter 7

Results

7.1 Cross Sections

The cross section, σ, differential in some variable x is calculated from the number of selected events in a detector-level bin i, denoted by N_i, the respective correction factor C_i (cf. section 6.2), the width of the bin, denoted by $(\Delta x)_i$, and the integrated luminosity L of the data sample:

$$\left(\frac{d\sigma}{dx}\right)_i = \frac{C_i \cdot N_i}{L \cdot (\Delta x)_i} \tag{7.1}$$

In this section, differential cross sections are presented that were measured as defined in section 5.5. They are presented separately for selection 1 and selection 2. Cross sections measured earlier by the ZEUS Collaboration in data from the years 1996-1997 [47] are shown for comparison where available. These older data were already compared to next-to-leading-order QCD calculations. The theory could not reproduce all features of the data, but the overall description was reasonable. Next-to-leading-order QCD is well suited for studying the processes directly related to the hard primary interaction in a dijet event. In contrast, MPI cannot be described by next-to-leading-order calculations alone due to the low population of the hadronic final state. Phenomenological models in MC simulations using parton showering algorithms have to be employed. All cross sections measured in this thesis are compared to the leading-order prediction from PYTHIA. Besides the PYTHIA sample described in section 3.3, a sample that contains no MPI (but was generated identically in other respects) and the contribution from direct photon processes alone are shown. The PYTHIA samples are scaled with a factor that accounts for the fact that leading-order MC simulations typically describe the shape of differential cross sections but do not necessarily predict the exact magnitude of the cross section. These so-called k-factors are calculated as the ratio of the measured cross section over the predicted cross section. For this purpose, the cross section for $M_{jj} > 42\,\text{GeV}$ and the PYTHIA sample

without MPI were used here. The obtained k-factors are 1.17 and 0.95 for selection 1 and selection 2, respectively. The numerical values for all cross sections that were measured in this thesis can be found in appendix C.

7.1.1 Selection 1

The measured cross section as a function of $|\cos\theta^*|$ for selection 1 is shown in figure 7.1, separately for $x_\gamma < 0.75$ and $x_\gamma > 0.75$. It can be seen that the cross section rises more steeply with increasing $|\cos\theta^*|$ in the resolved-enriched than in the direct-enriched region (the ratio of the cross sections in the last bin and the first bin is 10.6 ± 1.3 for $x_\gamma < 0.75$ and 5.1 ± 0.4 for $x_\gamma > 0.75$). This difference in shape is related to a difference in the dominant propagators in the underlying processes (cf. section 1.2.2). The results for the 1998-2000 data agree with the old data from 1996-1997 within the statistical uncertainties, which are smaller than 12% for each data set. The prediction from PYTHIA lies $(10 - 20)\%$ below the measured cross section in the direct-enriched region and roughly by the same amount above the measurement in the resolved-enriched region. The influence of MPI on this differential cross section is small, which can be understood from the fact that it is measured exclusively for high dijet masses ($M_{jj} > 42\,\text{GeV}$). Differences between the PYTHIA samples with and without MPI are only visible for high values of $|\cos\theta^*|$ in the resolved-enriched region, where the prediction of PYTHIA without MPI is though slightly closer to the measured cross section.

Figure 7.2 shows the cross section as a function of M_{jj}. In most bins, the prediction from PYTHIA lies again about $(10-20)\%$ below the measured cross section in the direct-enriched region and above the measurement in the resolved-enriched region. Effects of the MPI model are visible in the resolved-enriched region only.

Figure 7.3 shows the cross section as a function of x_γ in four different regions of the transverse energy of the leading jet, $E_{T,1}$. The low-x_γ region tends to be kinematically suppressed and for this reason the cross section falls more rapidly with decreasing x_γ for high values of $E_{T,1}$. The relative difference between old and new data amounts up to about 20% in these differential cross sections. The best agreement is observed for $17\,\text{GeV} < E_{T,1} < 25\,\text{GeV}$. Again, with respect to the measurement the PYTHIA prediction is too high in the resolved and too low in the direct-enriched region. The largest discrepancies are observed in the mid-x_γ region ($0.4 < x_\gamma < 0.6$) for $E_{T,1} < 25\,\text{GeV}$, where the agreement between old and new data is quite good (within 5%). Effects of MPI are visible for low values of $E_{T,1}$ in the low-x_γ region. The cross section as a function of x_γ is shown in figure 7.4 separately for $M_{jj} < 42\,\text{GeV}$ and $M_{jj} > 42\,\text{GeV}$. Here, the influence on MPI on the low-x_γ region for low jet masses and the kinematic suppression of this region for high jet masses can be seen even more clearly. All discrepancies between the measured cross section and PYTHIA are observed in analogy to figure 7.3.

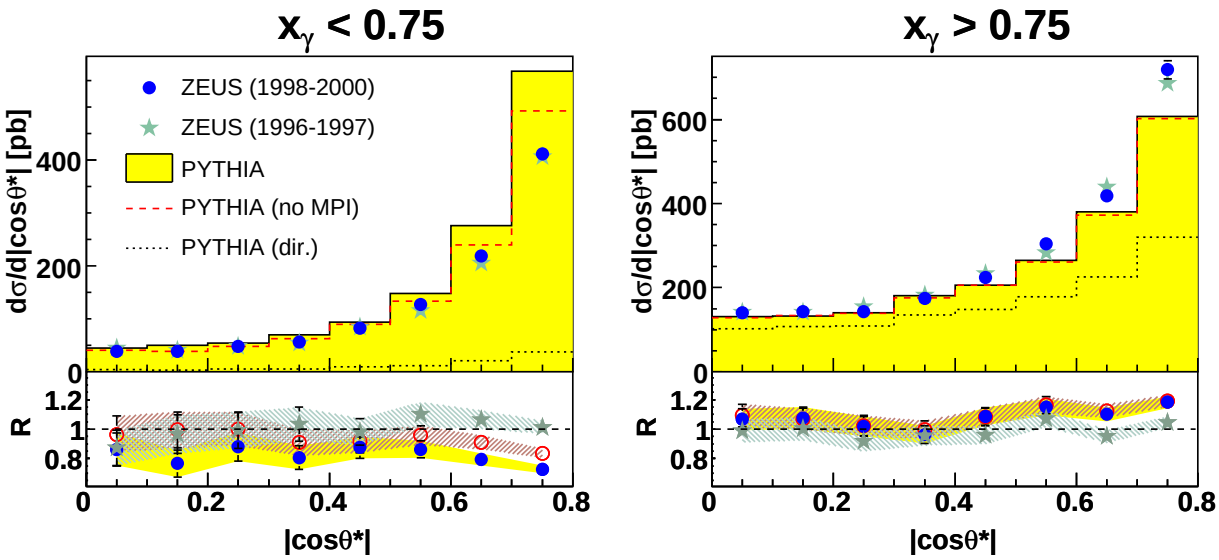

Figure 7.1: Measured cross section for selection 1 as a function of $|\cos\theta^*|$ for the resolved-enriched region ($x_\gamma < 0.75$) and for the direct-enriched region ($x_\gamma > 0.75$). The ratio R is shown for ZEUS 1998-2000 over ZEUS 1996-1997 (stars), for ZEUS 1998-2000 over PYTHIA with MPI (solid points) and for ZEUS 1998-2000 over PYTHIA without MPI (open circles). For all data sets, only statistical uncertainties are taken into account and visualized using error bars and shaded or hatched bands.

Figure 7.5 shows the cross section as a function of W, separately for $M_{jj} < 42\,\text{GeV}$ and $M_{jj} > 42\,\text{GeV}$. For high dijet masses, the cross section falls noticeably with decreasing W. This is reasonable since the production of two jets with high masses is suppressed for low energies of the γp system. An influence of MPI is observed for high values of W. PYTHIA without MPI describes the measured cross section well in most bins. The agreement is within 5% except for low values of W and M_{jj}, where the contribution from direct photon processes is relatively high and the prediction from PYTHIA is up to 20% below the measured cross section. Just were the effect of MPI is the largest, i.e. for low M_{jj} and and high W, the prediction from PYTHIA including MPI is $(10 - 20)\%$ too high with respect to the measurement.

The cross section as a function of η_2 is shown in figure 7.6 for $x_\gamma < 0.75$ and in figure 7.7 for $x_\gamma > 0.75$. It can be seen that the boost towards the forward region is significantly larger in the resolved-enriched than in the direct-enriched region. For $x_\gamma > 0.75$, old and new data agree within statistical uncertainties (here typically smaller than 5% for each data set) in nearly all bins. For $x_\gamma < 0.75$, the agreement is slightly worse. An eye-catching difference is found for $\eta_1 < 0.0$ and $\eta_2 > 2.0$ (i.e. the two jets have the largest distance in η that is possible in the kinematic region of this analysis) in the resolved-enriched region. The discrepancy amounts to 24% in this bin. The prediction from PYTHIA is again too high for $x_\gamma < 0.75$ and too low for $x_\gamma > 0.75$ with respect to the measured cross section. It is worth noting that the agreement seems to be getting better the higher the contribution from direct photon processes is.

The cross section is shown as a function of E_T^{int} in figure 7.8 and as a function of $E_T^{\text{int}}/E_T^{\text{tot}}$ in figure 7.9. The prediction of PYTHIA without MPI is drastically below the measured cross section for high values of E_T^{int} and $E_T^{\text{int}}/E_T^{\text{tot}}$. The relative difference between data and PYTHIA without MPI is nearly 60% for $M_{jj} < 42\,\text{GeV}$ and still more than 40% for $M_{jj} > 42\,\text{GeV}$, while the agreement between the measurement and the prediction from PYTHIA including MPI is within 20% for all bins. In the case of selection 1, the energy in the intermediate region will not solely be due to MPI but also to FSR and other effects. It is therefore even more interesting to look at $d\sigma/dE_T^{\text{int}}$ and $d\sigma/d(E_T^{\text{int}}/E_T^{\text{tot}})$ for selection 2.

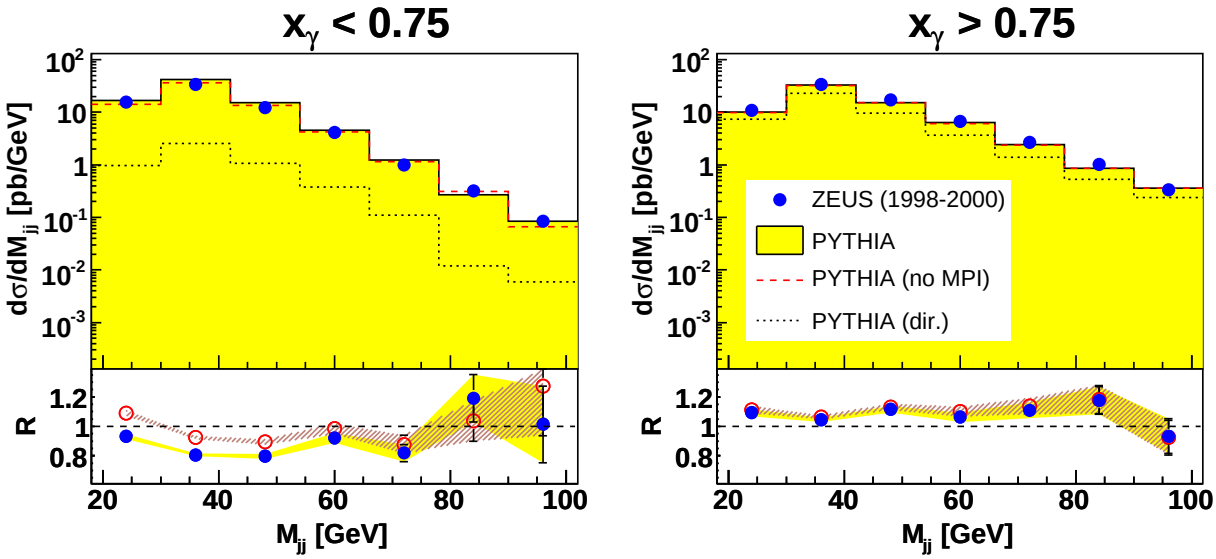

Figure 7.2: Measured cross section for selection 1 as a function of M_{jj} for the resolved- enriched region ($x_\gamma < 0.75$) and for the direct-enriched region ($x_\gamma > 0.75$). The ratio R is shown for ZEUS 1998-2000 over PYTHIA with MPI (solid points) and for ZEUS 1998-2000 over PYTHIA without MPI (open circles). Only statistical uncertainties are taken into account and visualized using error bars and shaded or hatched bands.

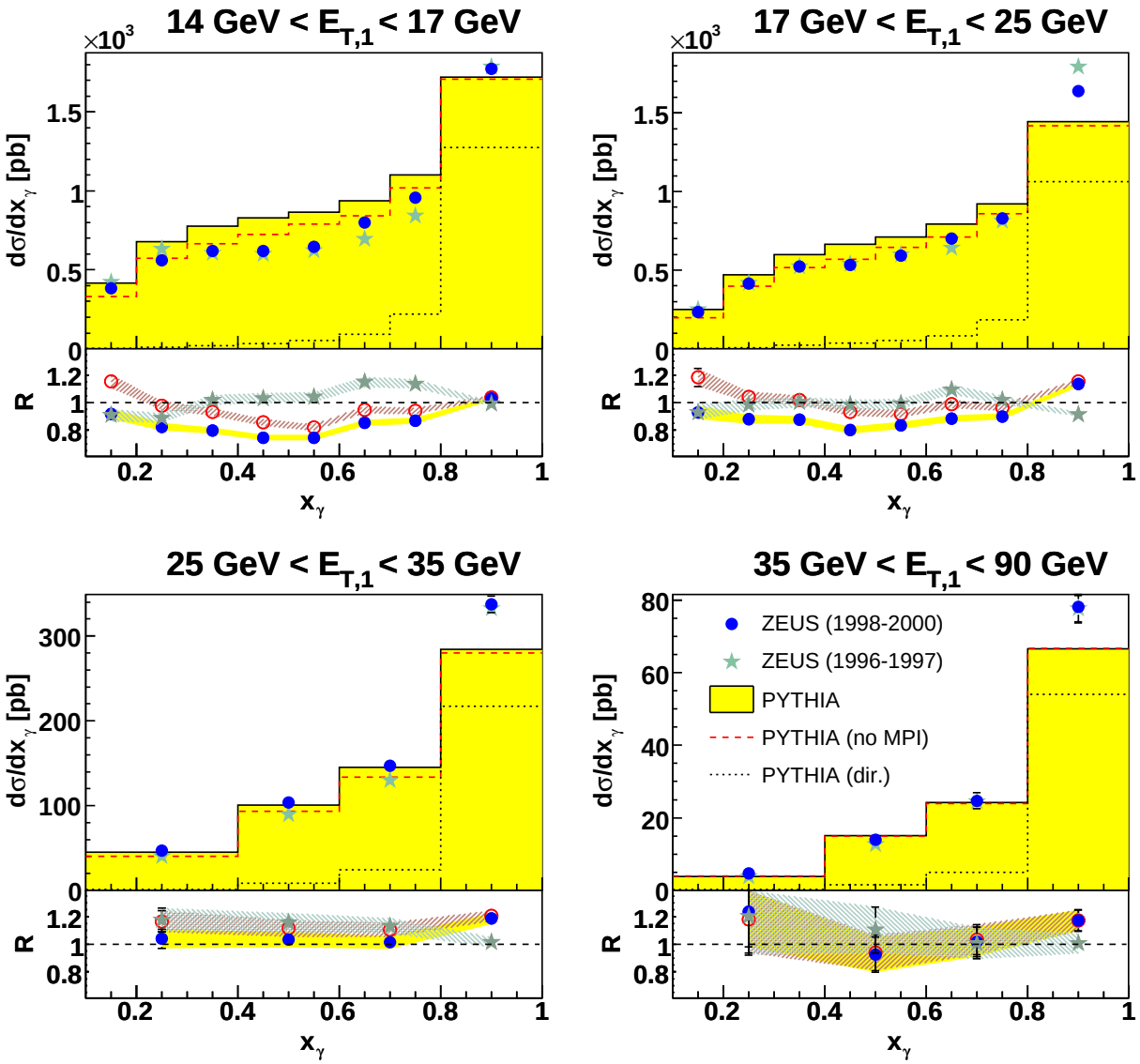

Figure 7.3: Measured cross section for selection 1 as a function of x_γ in four different regions of the transverse energy of the leading jet, $E_{T,1}$. See the caption to figure 7.1 for further details.

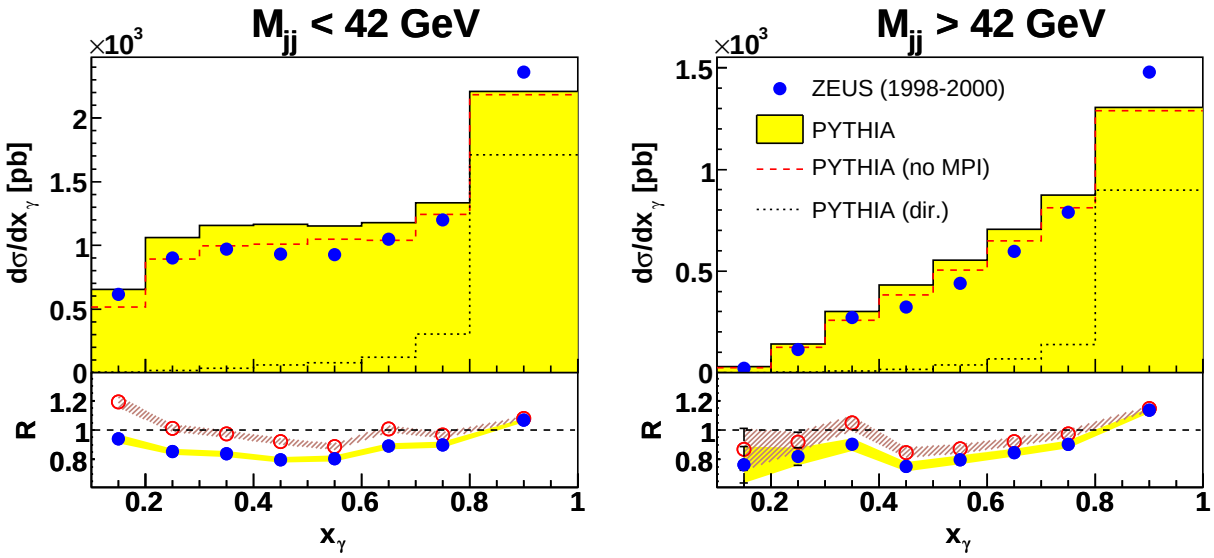

Figure 7.4: Measured cross section for selection 1 as a function of x_γ for low and for high values of the dijet mass M_{jj}. See the caption to figure 7.2 for further details.

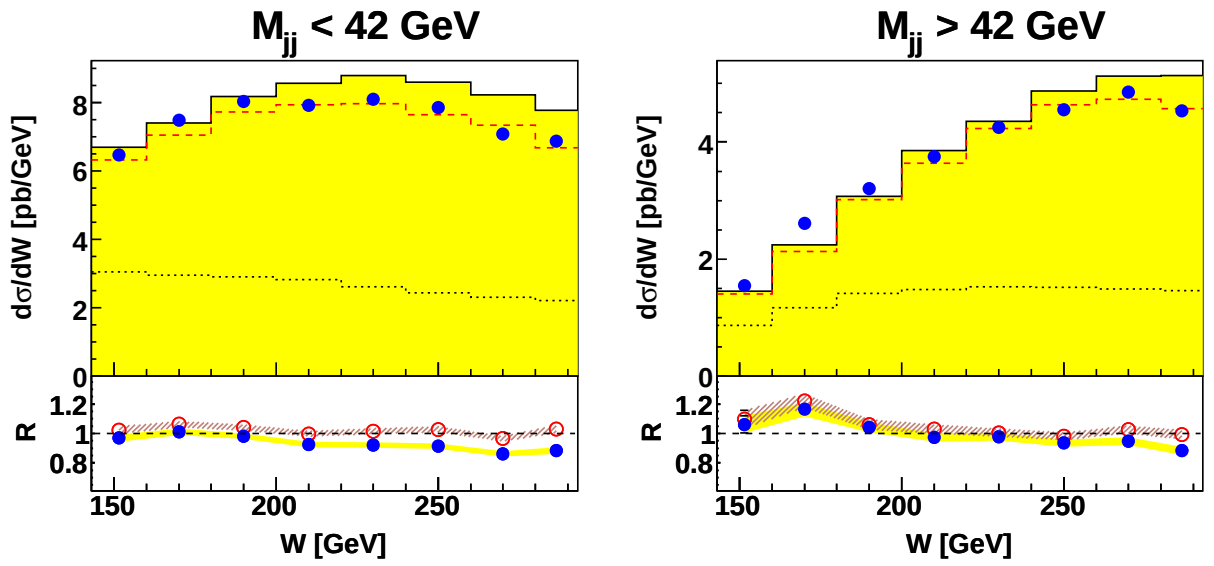

Figure 7.5: Measured cross section for selection 1 as a function of W for low and for high values of the dijet mass M_{jj}. See the caption to figure 7.2 for further details.

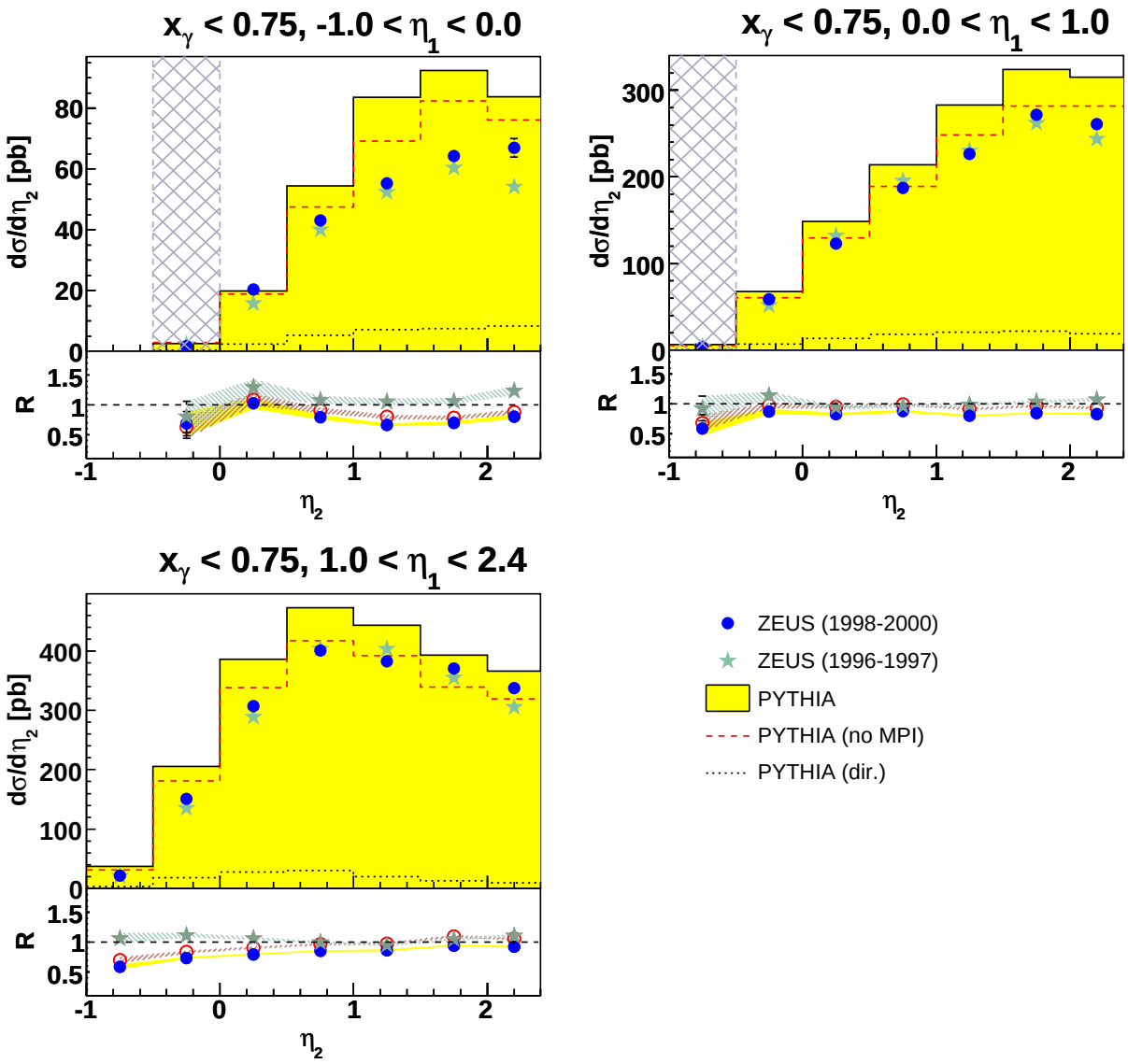

Figure 7.6: Measured cross section for selection 1 as a function of η_2 for the resolved-enriched region ($x_\gamma < 0.75$). The measurement is divided into three different regions of the pseudorapidity of the other jet, η_1. See the caption to figure 7.1 for further details, but note the different scale used to visualize the ratio R here. A crosshatched area is used to indicate bins in which the efficiency was below 10%.

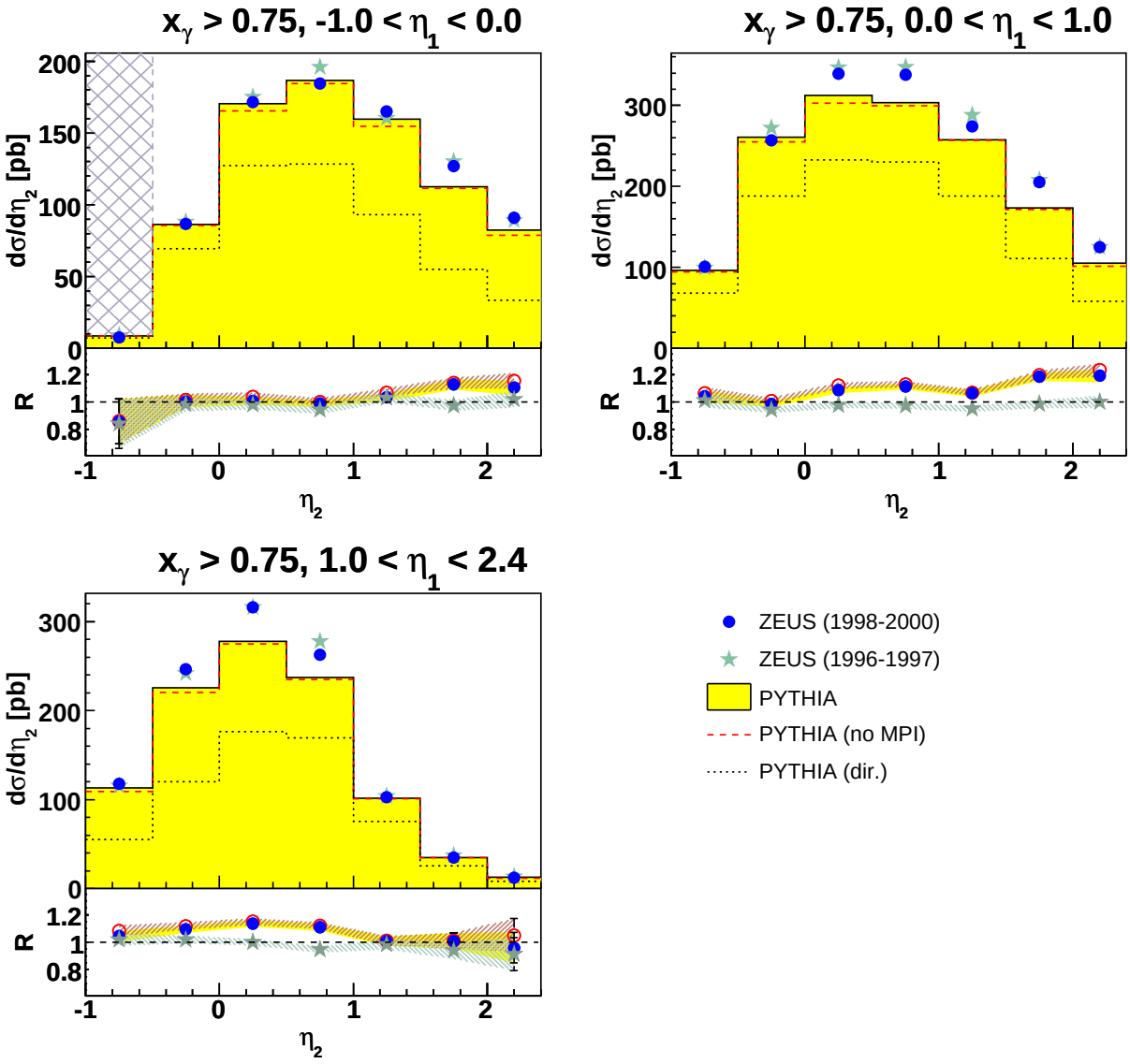

Figure 7.7: Measured cross section for selection 1 as a function of η_2 for the direct-enriched region ($x_\gamma > 0.75$). The measurement is divided into three different regions of the pseudorapidity of the other jet, η_1. See the caption to figure 7.1 for further details. A crosshatched area is used to indicate bins in which the efficiency was below 10%.

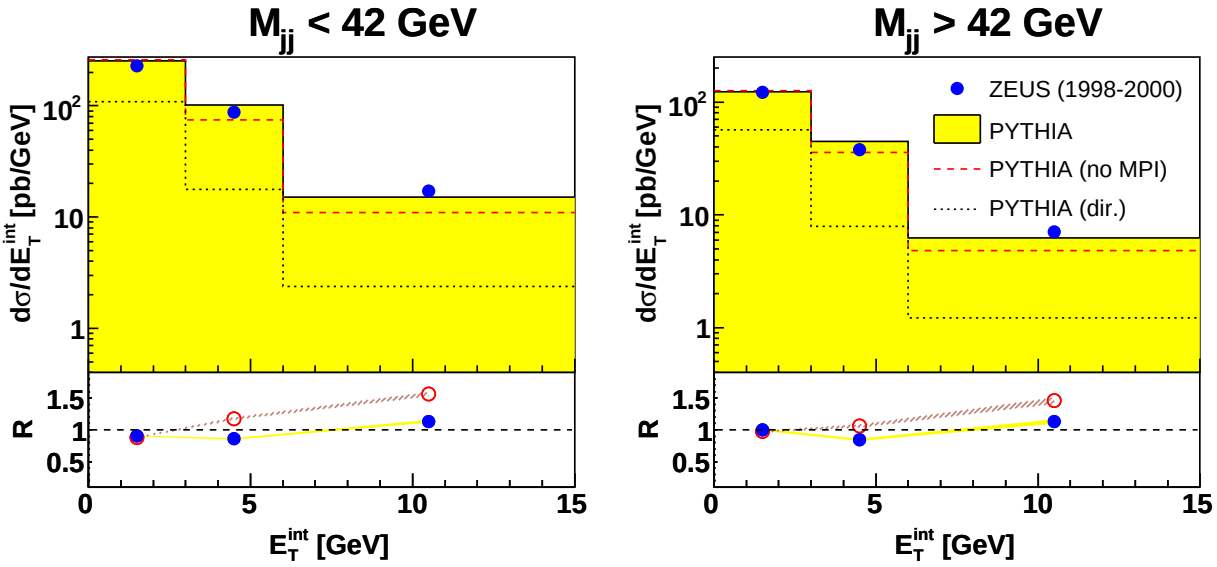

Figure 7.8: Measured cross section for selection 1 as a function of $E_T^{\rm int}$ for low and for high values of the dijet mass M_{jj}. See the caption to figure 7.2 for further details, but note the different scale used to visualize the ratio R here.

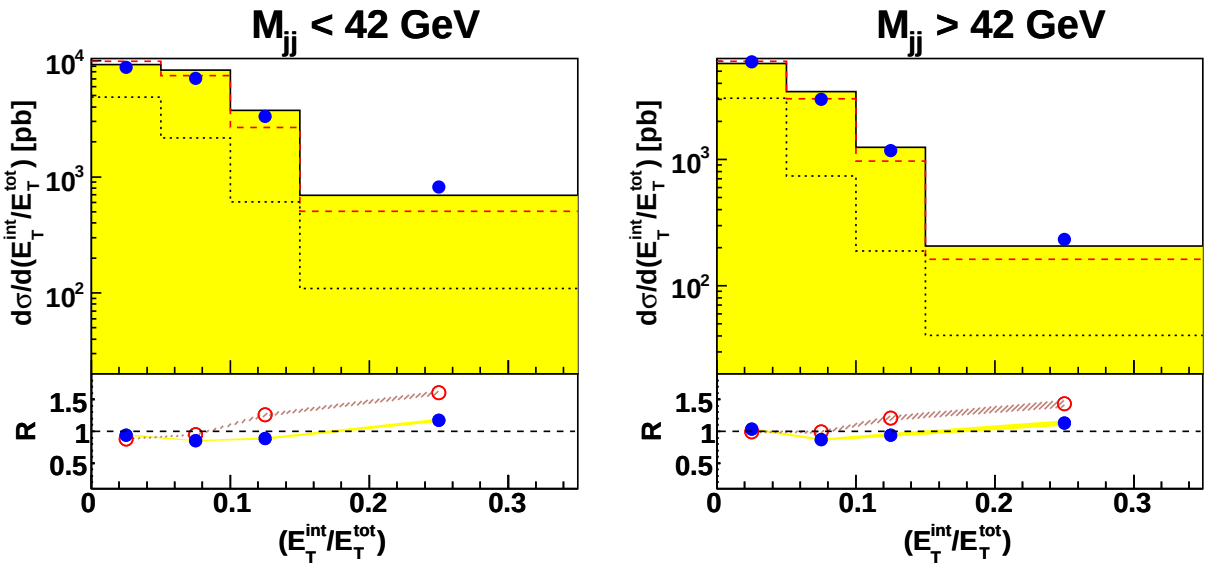

Figure 7.9: Measured cross section for selection 1 as a function of the ratio $E_T^{\rm int}/E_T^{\rm tot}$ for low and for high values of the dijet mass M_{jj}. See the caption to figure 7.2 for further details, but note the different scale used to visualize the ratio R here.

Summary Selection 1
Good agreement between differential cross sections measured in this analysis and ZEUS data from the years 1996-1997 is observed for the more inclusive dijet selection 1. Differences in shape between the resolved-enriched region ($x_\gamma < 0.75$) and the direct-enriched region ($x_\gamma > 0.75$) are confirmed. The cross section for $x_\gamma < 0.75$ rises more steeply with increasing $|\cos\theta^*|$, which can be explained by the different propagator terms in the underlying hard processes. In addition, the resolved part is boosted more towards the forward direction, i.e. large η. This effect is due to the smaller amount of photon momentum entering the hard scattering that is given by x_γ. The prediction from PYTHIA lies typically $(10-20)\%$ above the measured cross section in the resolved-enriched region and by the same amount below the measurement in the direct-enriched region.
Differences in the prediction from PYTHIA with and without MPI are observed in the resolved-enriched region. The effects are concentrated in the region of high γp center-of-mass energies, W, and low dijet masses, M_{jj}, and are more pronounced for small values of x_γ. This can be understood from the fact that in this kinematic region enough phase space is left for secondary interactions. PYTHIA without MPI is slightly closer to the measurement than PYTHIA with MPI in the case of some differential cross sections, but the inclusion of MPI seems to be necessary for an adequate description of the energy flow between the two leading jets. PYTHIA without MPI definitely underestimates the energy in the intermediate region in the azimuthal plane, while PYTHIA with MPI gives a reasonable description of the data.

7.1.2 Selection 2

The measured cross section as a function of $|\cos\theta^*|$ for selection 2 is shown in figure 7.10. The differences in shape between the resolved-enriched and the direct-enriched region can be observed similarly to selection 1 (the ratio of the cross sections in the last bin and the first bin is here 9.4 ± 1.6 for $x_\gamma < 0.75$ and 4.9 ± 0.4 for $x_\gamma > 0.75$). The prediction from PYTHIA lies $(10-30)\%$ below the measured cross section in the direct-enriched region and roughly by the same amount above the measurement in the resolved-enriched region (nearly 50% in one bin of $|\cos\theta^*|$).

Figure 7.11 shows the cross section as function of M_{jj}. Again, the prediction from PYTHIA lies $(10-30)\%$ below the measurement for $x_\gamma > 0.75$ and by the same amount above the measurement in most bins for $x_\gamma < 0.75$. Notable differences between the predictions from PYTHIA with and without MPI can be seen exclusively for low values of M_{jj} in the resolved-enriched region. The predicted cross section is closer to the measurement without than with MPI.

The cross section as a function of x_γ is shown in figures 7.12 and 7.13. With respect to the measurement, the PYTHIA prediction is again too high in the resolved-enriched and too low in the direct-enriched region. The largest differences are observed in the mid-x_γ

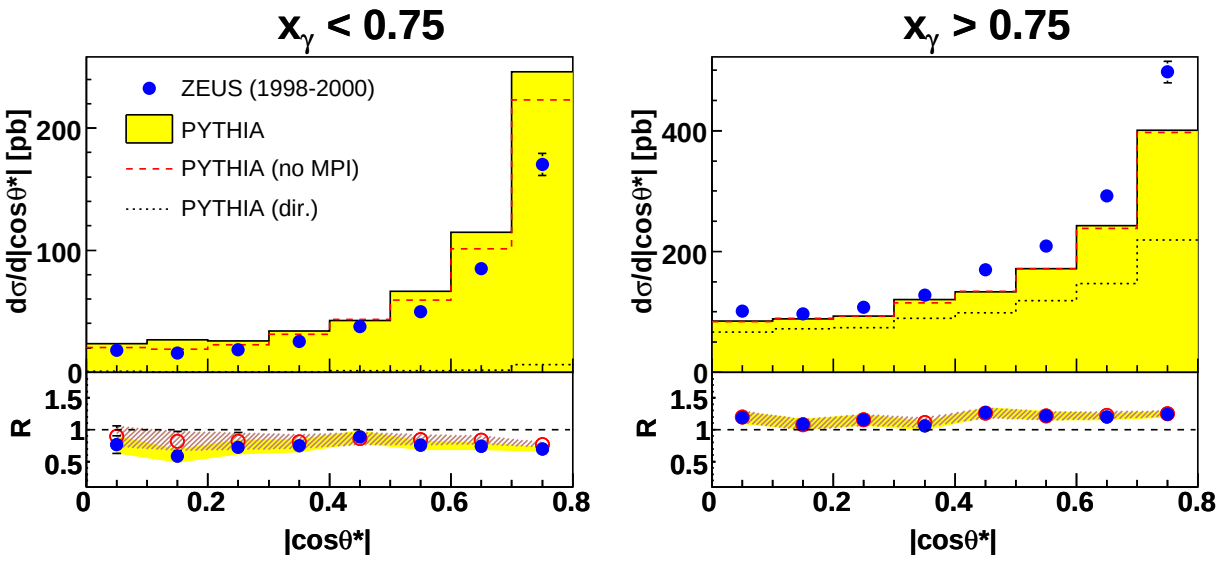

Figure 7.10: Measured cross section for selection 2 as a function of $|\cos\theta^*|$ for the resolved-enriched region ($x_\gamma < 0.75$) and for the direct-enriched region ($x_\gamma > 0.75$). The ratio R is shown for ZEUS over PYTHIA with MPI (solid points) and for ZEUS over PYTHIA without MPI (open circles). Only statistical uncertainties are taken into account and visualized using error bars and shaded or hatched bands. Note the enlarged scale used to visualize the ratio R here.

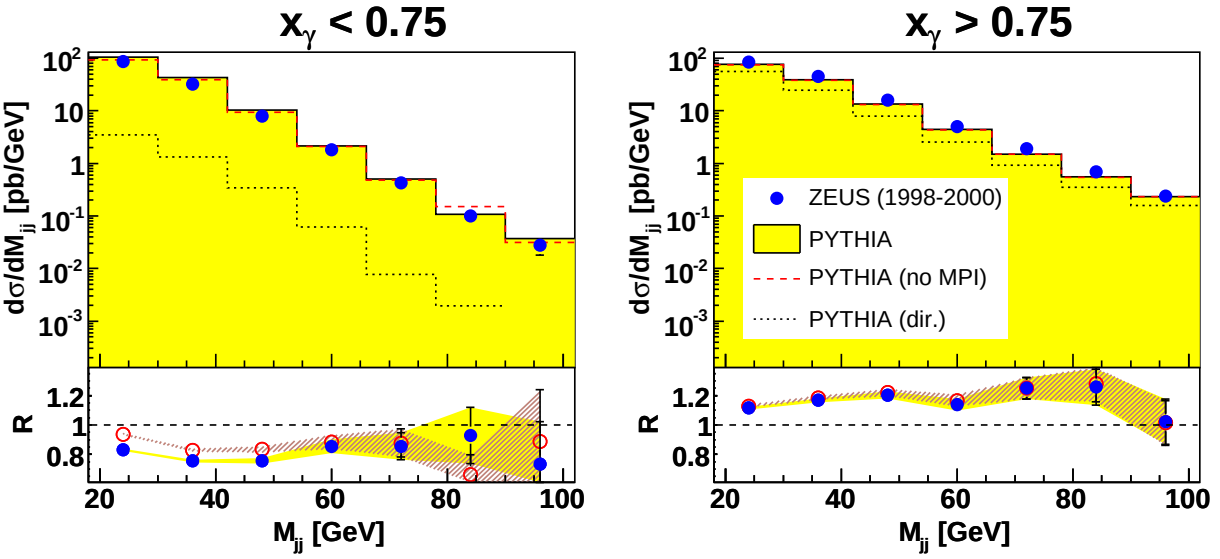

Figure 7.11: Measured cross section for selection 2 as a function of M_{jj} for the resolved-enriched region ($x_\gamma < 0.75$) and for the direct-enriched region ($x_\gamma > 0.75$). See the caption to figure 7.10 for further details.

region for $E_{T,1} < 25\,\text{GeV}$. Effects of the MPI model are visible for low x_γ and low M_{jj}. The low-x_γ region is suppressed for high values of M_{jj}.

Figure 7.14 shows the cross section as a function of W. As for selection 1, the cross section falls noticeably with decreasing W for $M_{jj} > 42\,\text{GeV}$. The biggest effects of the MPI model can be seen for high values of W and $M_{jj} < 42\,\text{GeV}$. Again, PYTHIA without MPI seems to describe the measured cross section in this range slightly better than PYTHIA with MPI. Both predictions fail up to around 20% in other regions of W.

The cross section as a function of η_2 is shown in figure 7.15 for $x_\gamma < 0.75$ and in figure 7.16 for $x_\gamma > 0.75$. It can bee seen that, as observed for selection 1, the boost towards the forward region is significantly larger in the resolved-enriched than in the direct-enriched region. Like for the other cross sections, the prediction from PYTHIA lies $(10 - 30)\%$ below the measurement in the direct-enriched and above it in the resolved-enriched region.

The cross section as a function of E_T^{int} and as a function of $E_T^{\text{int}}/E_T^{\text{tot}}$ is shown in figure 7.17 and figure 7.18, respectively. For $6\,\text{GeV} < E_T^{\text{int}} < 15\,\text{GeV}$ and $M_{jj} < 42\,\text{GeV}$, the PYTHIA prediction without MPI is too low with respect to the measurement by a factor of 3. For $0.15 < E_T^{\text{int}}/E_T^{\text{tot}} < 0.35$ and $M_{jj} < 42\,\text{GeV}$, the prediction without MPI is about 80% too low. PYTHIA with MPI describes the measured cross section relatively well over the whole range, the agreement is within 20% in all bins. The measured differential cross sections for high dijet masses fall extremely more rapidly than in the case of low masses. For $M_{jj} < 42\,\text{GeV}$, the distribution of $d\sigma/d(E_T^{\text{int}}/E_T^{\text{tot}})$ actually does not peak in the first bin but at $0.05 < E_T^{\text{int}}/E_T^{\text{tot}} < 0.10$. This shape is not described by PYTHIA without the MPI model. It should be mentioned that for selection 2, where the energy flow into the intermediate region from other effects than MPI is minimized, the differences between the PYTHIA predictions with and without MPI are drastically larger for low than for high dijet masses. The fact that clear differences can still be seen at $M_{jj} > 42\,\text{GeV}$ indicates that there is some influence from soft MPI even above this value of the dijet mass.

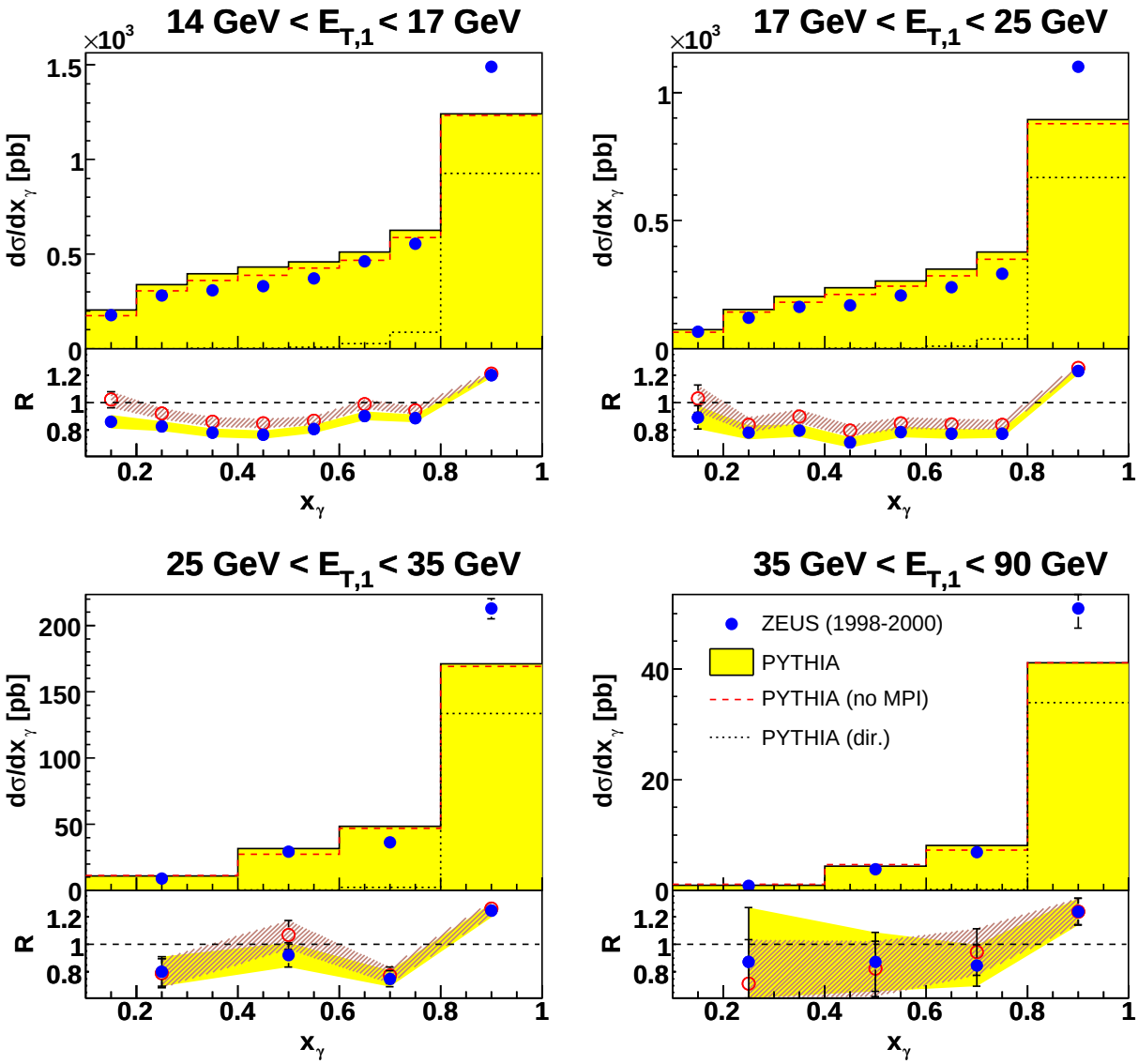

Figure 7.12: Measured cross section for selection 2 as a function of x_γ in four different regions of the transverse energy of the leading jet, $E_{T,1}$. See the caption to figure 7.10 for further details.

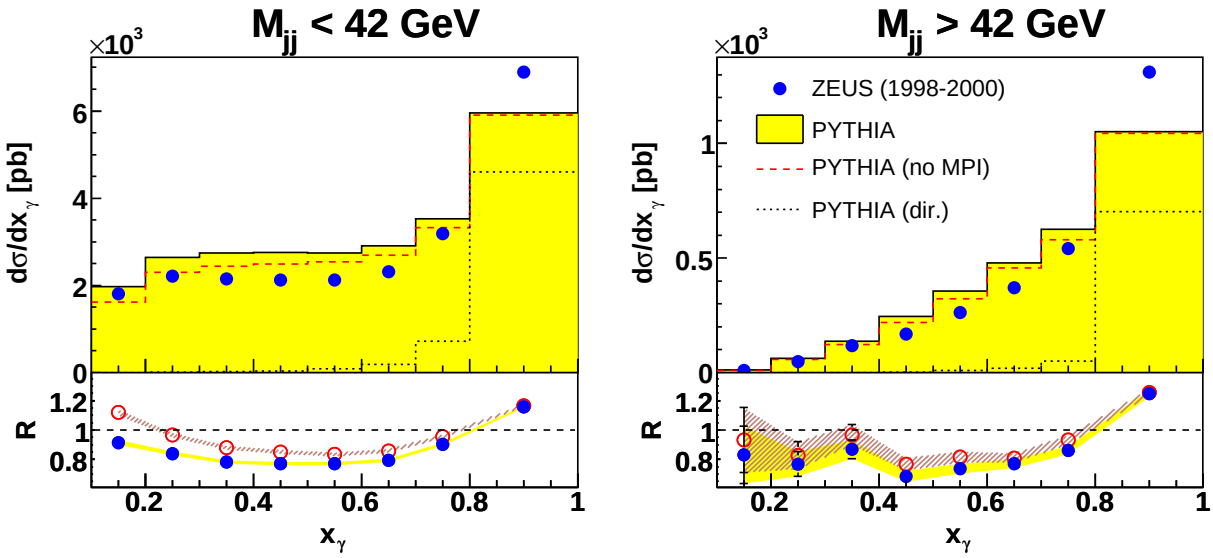

Figure 7.13: Measured cross section for selection 2 as a function of x_γ for low and for high values of the dijet mass M_{jj}. See the caption to figure 7.10 for further details.

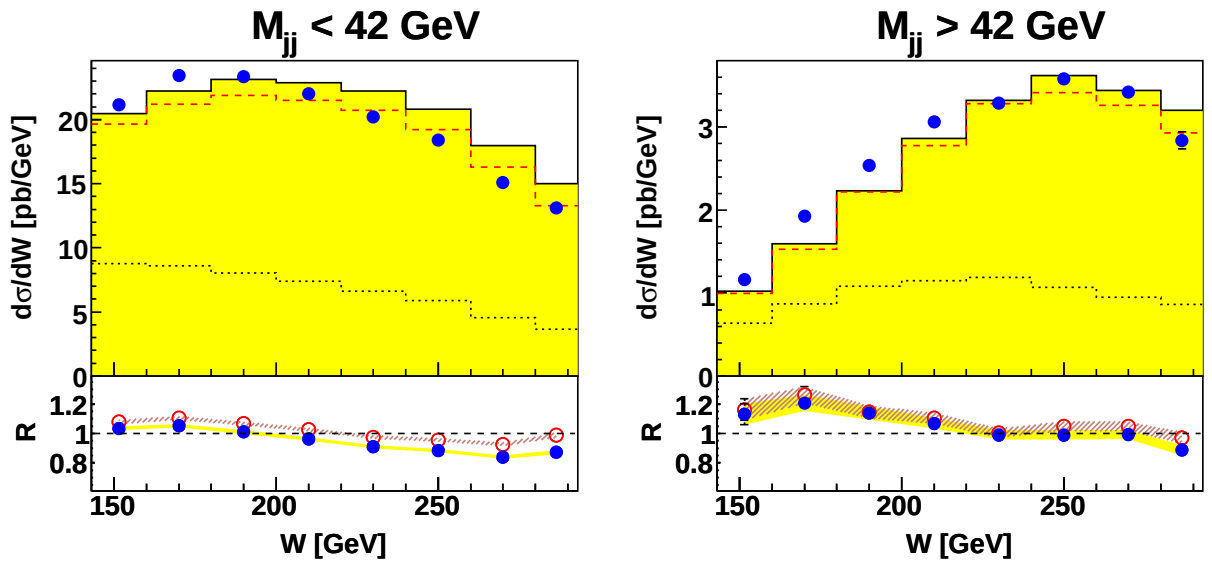

Figure 7.14: Measured cross section for selection 2 as a function of W for low and for high values of the dijet mass M_{jj}. See the caption to figure 7.10 for further details.

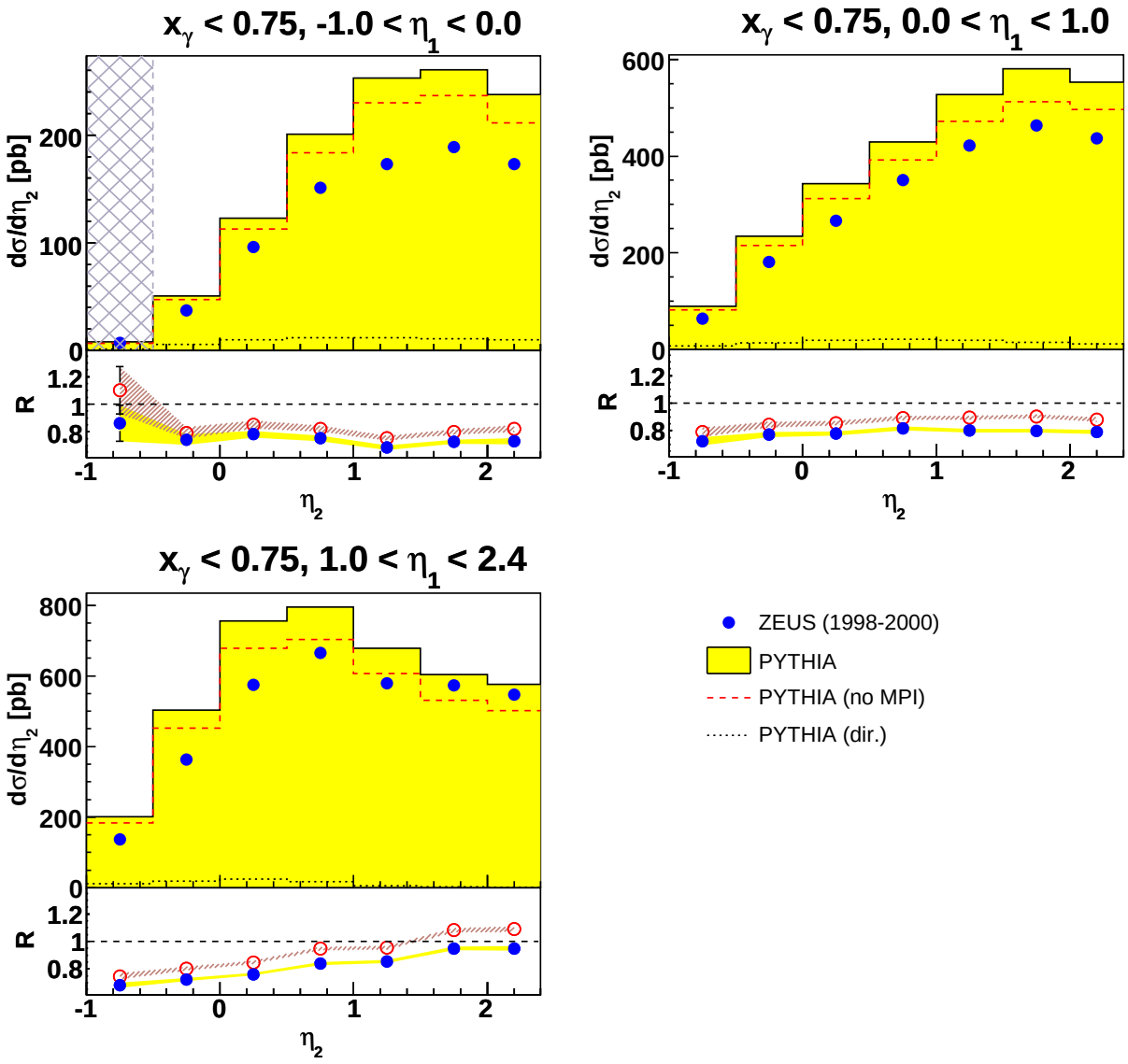

Figure 7.15: Measured cross section for selection 2 as a function of η_2 for the resolved-enriched region ($x_\gamma < 0.75$). The measurement is divided into three different regions of the pseudorapidity of the other jet, η_1. See the caption to figure 7.10 for further details. A crosshatched area is used to indicate bins in which the efficiency was below 10%.

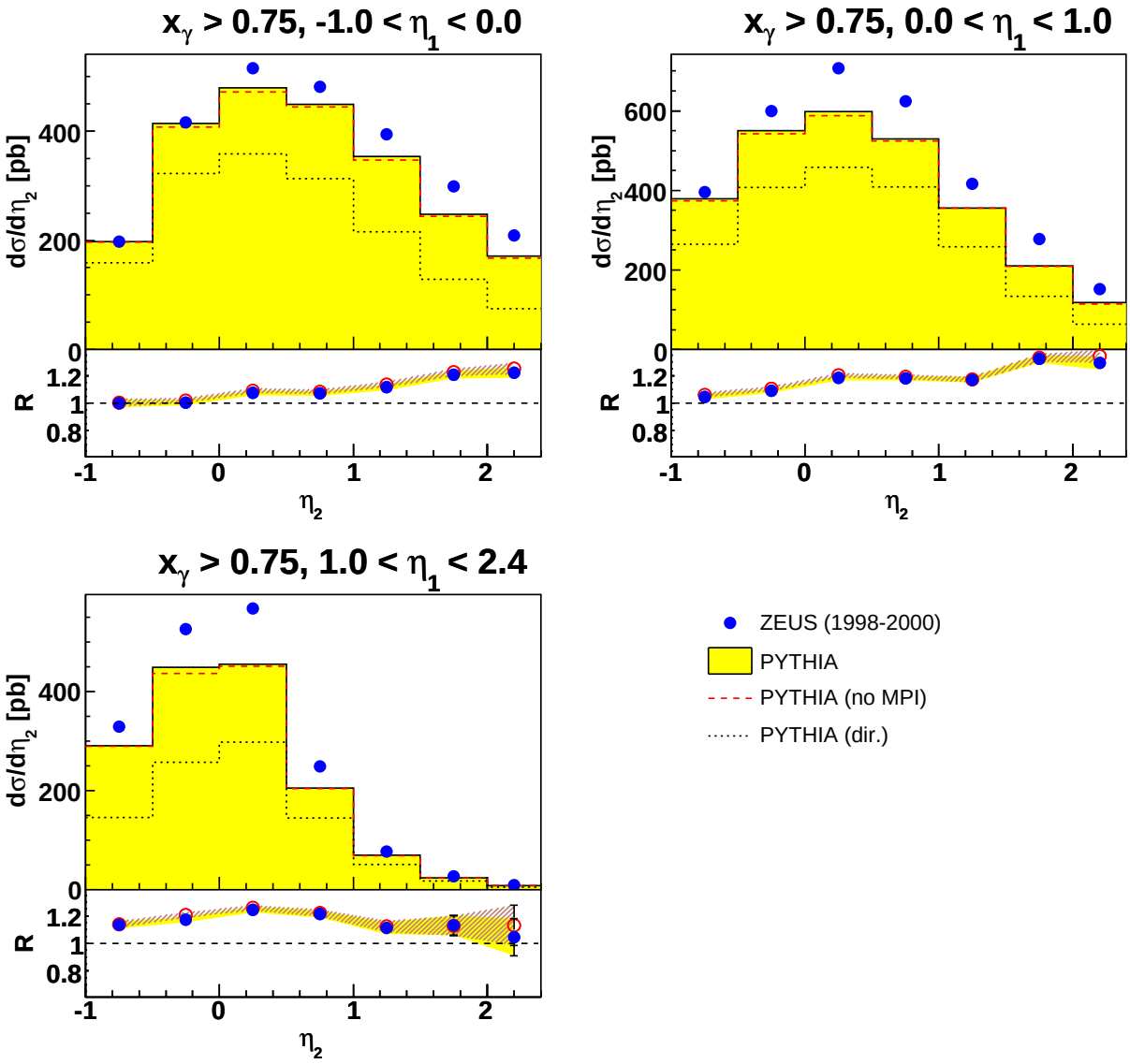

Figure 7.16: Measured cross section for selection 2 as a function of η_2 for the direct-enriched region ($x_\gamma > 0.75$). The measurement is divided into three different regions of the pseudorapidity of the other jet, η_1. See the caption to figure 7.10 for further details.

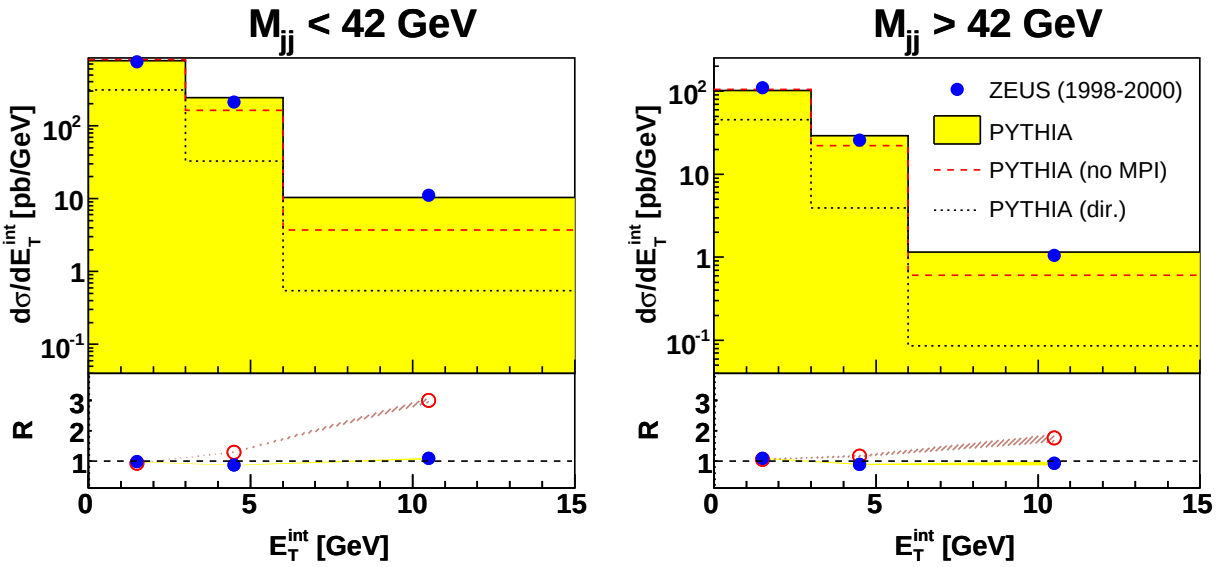

Figure 7.17: Measured cross section for selection 2 as a function of E_T^{int} for low and for high values of the dijet mass M_{jj}. See the caption to figure 7.10 for further details, but note the different scale used to visualize the ratio R here.

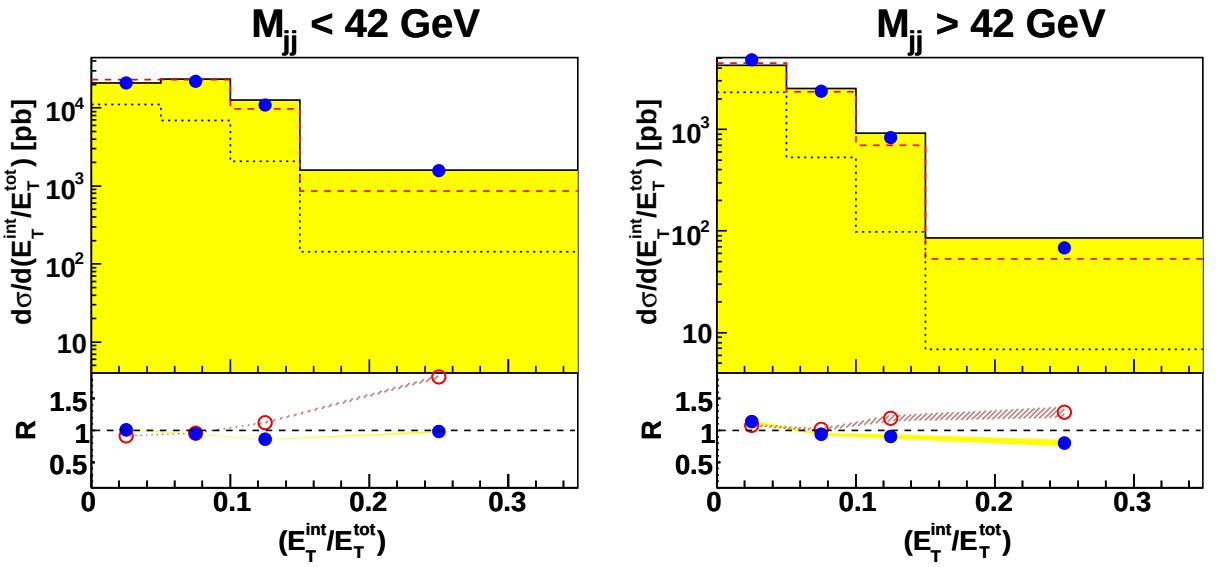

Figure 7.18: Measured cross section for selection 2 as a function of the ratio $E_T^{\text{int}}/E_T^{\text{tot}}$ for low and for high values of the dijet mass M_{jj}. See the caption to figure 7.10 for further details, but note the different scale used to visualize the ratio R here.

Summary Selection 2

Most observations that can be made in the differential cross sections measured for the more exclusive dijet selection 2 are similar to what has been seen in selection 1 (cf. section 7.1.1). The cross section in the resolved-enriched region ($x_\gamma < 0.75$) rises more steeply with increasing $|\cos\theta^*|$ and is boosted more towards the forward direction than the cross section in the region dominated by direct photon processes ($x_\gamma > 0.75$). The prediction from PYTHIA for selection 2 differs slightly more from the data than in the case of selection 1 and lies typically $(10 - 30)\%$ above the measured cross section in the resolved-enriched region and by the same amount below the measurement in the direct-enriched region.

Differences in the prediction from PYTHIA with and without MPI are observed in the resolved-enriched region, predominantly for high W, low M_{jj} and small x_γ. PYTHIA without MPI is again slightly closer to the measurement than PYTHIA with MPI in the case of some differential cross sections. However, the inclusion of MPI seems to be indispensable for an adequate description of the energy flow between the two jets. This can be seen even more clearly in selection 2, where the influence of other effects than MPI on the intermediate region is supposed to be minimized. PYTHIA with MPI gives a reasonable prediction of the energy flow, while PYTHIA without MPI fails completely.

7.2 Tuning PYTHIA

The large sensitivity to the MPI model in PYTHIA of some differential cross sections presented in section 7.1 is encouraging for further studies. For this purpose, a large number of PYTHIA samples with different parameter settings was generated and compared to the measured cross section on hadron level. As a starting point for a tuning procedure, four parameters of the MPI model were varied: `PARP(81)` and `PARP(90)`, which determine $p_{T,\mathrm{min}}^{\mathrm{MPI}}$ and its energy dependence according to equation 3.1, and `PARP(85)` and `PARP(86)`, which are related to the fraction of gluon pairs produced in MPI with and without color connections to the nearest neighbors in momentum space.[1] All other settings were kept fixed and as described in section 3.3. The parameter `PARP(81)` was changed with a step size of 0.1 GeV up and down from its default value at 1.9 GeV. The power of the energy-rescaling term, `PARP(90)`, was set to 0.00, 0.13, 0.16 (default value) and 0.19. Besides the default setting `PARP(85;86)` $= 0.33; 0.66$, the configuration `PARP(85;86)` $= 0.90; 0.95$, which is the default in newer PYTHIA versions, was tested for `PARP(90)` $= 0.00$ and `PARP(90)` $= 0.16$. Although more than a million events were generated for every point in the parameter space mentioned above, this corresponds only to roughly $(2-4)\,\mathrm{pb}^{-1}$ in each case, i.e. approximately $(2-5)\%$ of the integrated luminosity of the ZEUS data from 1998-2000, and only a few thousand events for each PYTHIA sample passed the final event selection.

A series of χ^2-tests is performed with the aim of assessing the degree by which the different MC predictions match the measurement. The differential cross section $d\sigma/d(E_T^{\mathrm{int}}/E_T^{\mathrm{tot}})$ for $M_{jj} < 42\,\mathrm{GeV}$ in selection 2 is used here, since it showed a large sensitivity to the MPI model and - compared to $d\sigma/dE_T^{\mathrm{int}}$ - the effect of energy mismeasurements is supposed to be reduced by cancellation. In order to adjust the normalization of the predicted cross section (cf. section 7.1), all PYTHIA samples are scaled with the same factor $k = 0.95$, which has been determined as the ratio of the measured cross section for $M_{jj} > 42\,\mathrm{GeV}$ and the prediction from PYTHIA without MPI. The number of degrees of freedom (NDF) in the χ^2-tests is 4. The resulting value of χ^2 as a function of `PARP(81)` is shown in figure 7.19 for 54 different PYTHIA samples. Despite the small statistics in the MC samples, the trend is clearly visible. A parabola is fitted to the distribution of the χ^2-values for each combination of values for `PARP(90)`, `PARP(85)` and `PARP(86)`. The position of the minimum of the parabola is used as an indicator for a possibly best value of `PARP(81)`. It has to be pointed out that none of the PYTHIA samples tested here gives a perfect description of the data, which would have been achieved at $\chi^2/\mathrm{NDF} \approx 1$.

Taking into account the respective `PARP(90)` as the power of the energy-rescaling term in equation 3.1 with the reference energy `PARP(89)` set to 1 TeV and using a mean γp center-of-mass energy of $\langle W \rangle = (213.38 \pm 0.15)\,\mathrm{GeV}$ for $M_{jj} < 42\,\mathrm{GeV}$ in selection 2, all curves presented in figure 7.19 are compatible with $p_{T,\mathrm{min}}^{\mathrm{MPI}} = (1.7 \pm 0.2)\,\mathrm{GeV}$. This is shown

[1] Cf. section 3.2 for more information about the parameters in PYTHIA.

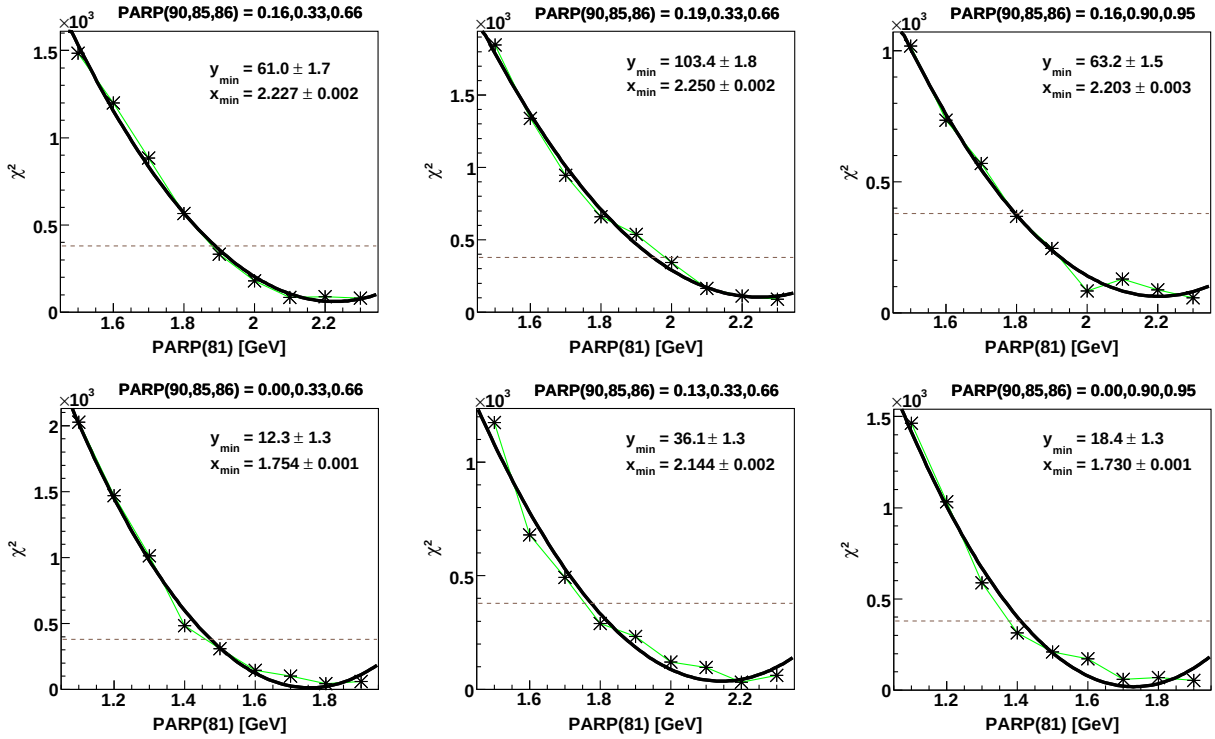

Figure 7.19: Results of the χ^2-test using the differential cross section $d\sigma/d(E_T^{\text{int}}/E_T^{\text{tot}})$ for $M_{jj} < 42\,\text{GeV}$ in selection 2 and PYTHIA samples with different parameter settings. Shown is χ^2 as a function of `PARP(81)`. Each of the six histograms holds the results for a specific combination of values for `PARP(90)`, `PARP(85)` and `PARP(86)`. x_{min} and y_{min} refer to the coordinates of the minimum of the parabola fitted to the histogram. The dashed line indicates the χ^2 obtained for PYTHIA without MPI.

`PARP(85;86)`	`PARP(90)`	`PARP(81)` [GeV]	$p_{T,\text{min}}^{\text{MPI}}$ [GeV]
0.33; 0.66	0.00	1.754 ± 0.001	1.754 ± 0.001
0.33; 0.66	0.13	2.144 ± 0.002	1.75 ± 0.16
0.33; 0.66	0.16	2.227 ± 0.002	1.74 ± 0.20
0.33; 0.66	0.19	2.250 ± 0.002	1.68 ± 0.22
0.90; 0.95	0.00	1.730 ± 0.001	1.730 ± 0.001
0.90; 0.95	0.16	2.203 ± 0.003	1.72 ± 0.19

Table 7.1: Summary of the results for `PARP(81)` from the χ^2-tests shown in figure 7.19. The values of $p_{T,\text{min}}^{\text{MPI}}$ for the different PYTHIA settings are calculated from the respective values of `PARP(81)` and `PARP(90)` using equation 3.1 with `PARP(89)` $= 1\,\text{TeV}$ and $\langle W \rangle = (213.38 \pm 0.15)\,\text{GeV}$.

in table 7.2. Details on the error estimation can be found in appendix D. It turns out that the relative uncertainty on the horizontal position of the minimum of a parabola is in the same order as the relative uncertainty on $\langle W \rangle$, which is roughly 1‰, but that the effect of the former on the the calculated value of $p_{T,\mathrm{min}}^{\mathrm{MPI}}$ is very small, while the effect of the latter is dominant. The samples generated with `PARP(85;86)` $= 0.33; 0.66$ suggest values of $p_{T,\mathrm{min}}^{\mathrm{MPI}}$ very close to 1.75 GeV. The only outlier is the sample with `PARP(90)` $= 0.19$, which yields 1.68 GeV. However, taking into account the large error of ± 0.22 GeV caused by the energy rescaling, also this $p_{T,\mathrm{min}}^{\mathrm{MPI}}$ is compatible with 1.75 GeV. Those samples generated with `PARP(85;86)` $= 0.90; 0.95$ seem to suggest values of $p_{T,\mathrm{min}}^{\mathrm{MPI}}$ closer to 1.73 GeV, i.e. slightly lower than for `PARP(85;86)` $= 0.33; 0.66$

The shift of the best value of `PARP(81)` as a function of `PARP(90)` and lines of constant values of χ^2 in the plane spanned by these two parameters are illustrated in figure 7.20 for a subset of the samples that are shown in figure 7.19.

The results presented here strongly suggest that the quality of the prediction by PYTHIA samples including the MPI model with `PARP(81)` set to an appropriate value is superior with respect to PYTHIA without MPI. However, lowering $p_{T,\mathrm{min}}^{\mathrm{MPI}}$ too far leads to the prediction of so much additional energy flow that PYTHIA without MPI is again noticeably closer to the measurement presented in this thesis (the respective χ^2 is indicated in figure 7.19 by a dashed line).[2] In the tuning performed so far, the value of `PARP(81)` was not raised higher than shown here. The intention was to avoid conflicts between $p_{T,\mathrm{min}}^{\mathrm{MPI}}$ and the minimum p_T of the hard primary interaction, which was set to 2.0 GeV, although in contrast to other generators PYTHIA does not require this explicit p_T ordering.

Unfortunately it is not possible to make strong statements yet about an optimal energy rescaling for $p_{T,\mathrm{min}}^{\mathrm{MPI}}$ and about the fraction of gluon pairs in MPI with and without color connections, although the results of this analysis seem to suggest `PARP(90)` $= 0.00$ (i.e. no energy rescaling) for the ZEUS data and differences in the minimum χ^2 for different settings of `PARP(85)` and `PARP(86)` are observed. Increased statistics in the MC samples and still more studies related to the uncertainties would be necessary to draw further conclusions. The analysis presented here is a first step towards a more precise tuning.

[2] Some bias might result from the fact that the k-factor for all samples in this analysis is determined using PYTHIA without MPI and the cross section for $M_{jj} > 42$ GeV even though still above this value of M_{jj} influences of MPI are observed.

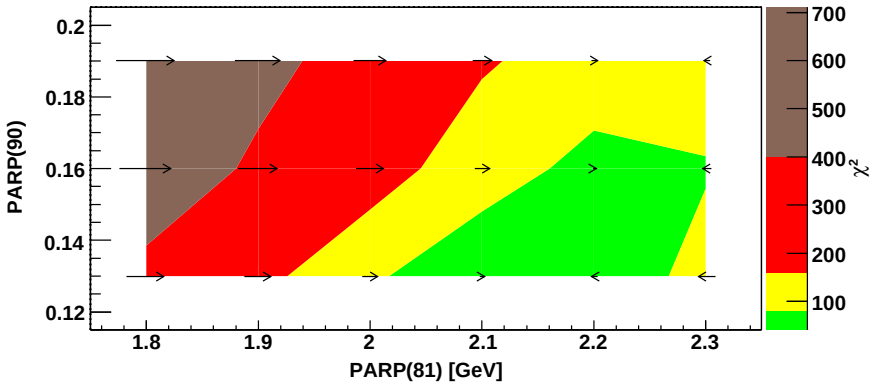

Figure 7.20: Results of the χ^2-test using the differential cross section $d\sigma/d(E_T^{\text{int}}/E_T^{\text{tot}})$ for $M_{jj} < 42\,\text{GeV}$ in selection 2 and PYTHIA samples with the setting `PARP(85;86)` $= 0.33; 0.66$. Shown is χ^2 as a function of `PARP(81)` and `PARP(90)`. The arrows illustrate the gradient along three lines of constant `PARP(90)`, pointing towards the minimum of the respective parabola shown in figure 7.19. Note that `PARP(90)` $= 0.00$, which gave the best χ^2 in this analysis, is not shown in this figure.

Summary and Conclusions

In this thesis, dijet events in photoproduction at HERA have been studied. Data collected with the ZEUS detector in the years 1998-2000 and corresponding to an integrated luminosity of $81.7\,\mathrm{pb}^{-1}$ have been used. The kinematic range has been restricted to photon virtualities of $Q^2 < 1\,\mathrm{GeV}^2$ and inelasticities of $0.2 < y < 0.85$, leading to photon-proton center-of-mass energies in the range of $142\,\mathrm{GeV} < W < 293\,\mathrm{GeV}$.

A variety of differential dijet cross sections has been measured for two different sets of jet selection criteria. The measurements are based mainly on energy flow objects that have been reconstructed using a combination of tracking and calorimeter information. Several corrections for energy mismeasurements in the detector have been applied. Jets have been reconstructed with the k_T-clustering algorithm. A bin-by-bin correction method has been employed for unfolding the data to the level of final-state hadrons.

An inclusive sample of dijet events has been obtained by requiring at least two hard jets in the pseudorapidity range $-1.0 < \eta < 2.4$ with transverse energies $E_{T,1} > 14\,\mathrm{GeV}$ and $E_{T,2} > 11\,\mathrm{GeV}$. It has been shown that the cross sections obtained with these selection criteria are compatible with previously published results for the ZEUS data from 1996-1997, which already had been shown to agree reasonably with next-to-leading-order QCD calculations. It has not been studied further within the scope of this thesis how much the different center-of-mass energies ($134\,\mathrm{GeV} < W < 277\,\mathrm{GeV}$ in the 1996-1997 measurement) contribute to the observed discrepancies between the old and the new data set.

A second, more exclusive sample of dijet events has been obtained by requiring two hard jets in the pseudorapidity range $-1.0 < \eta < 2.4$ with transverse energies $E_{T,1} > 10\,\mathrm{GeV}$ and $E_{T,2} > 8\,\mathrm{GeV}$. In addition, it has been demanded that the two jets are roughly back-to-back in azimuth ($\Delta\phi_{jj} > 150°$), that they have almost equal transverse energies ($E_{T,2}/E_{T,1} > 0.75$) and that no further jets with $E_T > 5\,\mathrm{GeV}$ are found in the event. These additional criteria have been imposed in order to maximize the sensitivity to soft multiparton interactions (MPI) in the region between the jets.

All results have been compared to predictions from the the leading-order Monte Carlo (MC) simulation PYTHIA. It has been confirmed that regions in phase space dominated by either direct or resolved photon processes can be separated using the variable x_γ. With

respect to the measurement, PYTHIA seems to generally overestimate the cross sections for resolved photoproduction or underestimate direct photoproduction.

Besides the x_γ distribution, significant differences between direct and resolved photon processes can be seen in the shape of the differential cross sections as a function of the jet pseudorapidities and of $|\cos\theta^*|$, where θ^* is the dijet scattering angle. The mean pseudorapidity of the two jets in each event is sensitive to the momentum distributions of the incoming partons, and the scattering angle is related to the matrix elements of the hard processes. Except for very few bins, the respective cross sections measured for the inclusive dijet sample are in nice agreement with the 1996-1997 data. They are well described by the next-to-leading-order predictions, which is to be expected because these observables are closely related to the hard scattering matrix element and less sensitive to effects like MPI.

Significant differences in the predictions from PYTHIA with and without the "simple model" for MPI are observed in the resolved-enriched region. Contrary to expectations, PYTHIA without MPI seems to be closer to the measurement in a lot of bins. In the high-mass region defined by $M_{jj} > 42\,\text{GeV}$, only a comparatively small contribution from MPI is predicted . The largest effect of the MPI model is seen in variables correlated with the energy flow in the "intermediate region" between the two hard jets. Here, PYTHIA without MPI fails completely, while the simple MPI model gives a reasonable description of the measurement.

The measured cross section as a function of $E_T^{\text{int}}/E_T^{\text{tot}}$, the fraction of transverse energy in the event deposited in the region between the two jets, has been used in the low-mass region ($M_{jj} < 42\,\text{GeV}$) to tune parameters in PYTHIA's MPI model in a series of χ^2-fits. A large number of different MC samples has been generated and tested. The best results have been obtained with a minimum transverse momentum for MPI, $p_{T,\text{min}}^{\text{MPI}}$, in the range of $(1.7 \pm 0.2)\,\text{GeV}$. Due to limited statistics in the MC samples, it has not been possible yet to draw conclusions regarding other parameters.

Altogether, it has been shown that the physics of soft MPI can be studied in photoproduction at HERA. Some variables that are highly sensitive to the respective processes have been pointed out. A promising method for testing models and tuning their parameters has been presented. The measurement strongly suggests that soft MPI are required to adequately describe the data.

This thesis provides a basis for further investigations. Some ideas and open questions are listed in the following.

- Measuring cross sections for discrete values of W would allow to explicitly test the energy dependence of $p_{T,\text{min}}^{\text{MPI}}$ and allow to use the more sophisticated MPI models in PYTHIA.

- Measuring the number of charged particles in the region between the jets would allow to study the frequently reported problem of adjusting both the energy flow and the particle multiplicity in MPI at the same time.
- It is essential to study the systematic uncertainties on all measured quantities.
- It would be nice to further improve the trigger efficiency and the bin-to-bin migrations.
- Increasing the MC statistics in the interesting ranges of the parameter space would allow to draw further conclusions with respect to the different features of the MPI model. In addition, it would then be possible to split the MC samples for each point in the parameter space in order to get a better estimate for the uncertainty on the χ^2-values obtained in the tuning procedure.
- Finally, it is very important to compare the data to a second MC, e.g. HERWIG [49] with its MPI model JIMMY.

These tasks will hopefully be addressed within the ZEUS Collaboration in the near future.

Acknowledgments

I would like to express my gratitude to Prof. Robert Klanner and Prof. Peter Schleper for giving me the opportunity to join their workgroup, for providing such a pleasant working environment and for many helpful comments.

I am grateful to JunProf. Johannes Haller for reading this thesis as second referee.

The biggest impact on my work had Dr. Thomas Schörner-Sadenius. He captured me with his enthusiasm for this field of physics, and with inspiring energy he guided me throughout the course of my diploma study. Thank you, Thomas, for always giving me your precious attention regardless of how many other things were on your mind.

I also have to thank the other postdocs and students of our group, not only those working on jets at ZEUS, for helpful discussions on particle physics and programming issues. I only want to mention here Erik Butz, whose analysis code I inherited, as well as Thorben Theedt and Hanno Perrey, with whom I shared more than the office.

The analysis presented in this thesis was performed in a collaboration of many people from around the world. Without the effort of these people the results would not have been obtained. I am indebted to the ZEUS Collaboration and to the QCD group in particular. Exemplarily I would like to thank Dr. Claudia Glasman and Dr. Tim Namsoo for their advice.

Appendix A

Control Plots

On the next two pages, control plots for event variables and jet quantities after the final event selection but before the reweighting with respect to x_γ^{true} are shown. See section 5.4.1 for further informations.

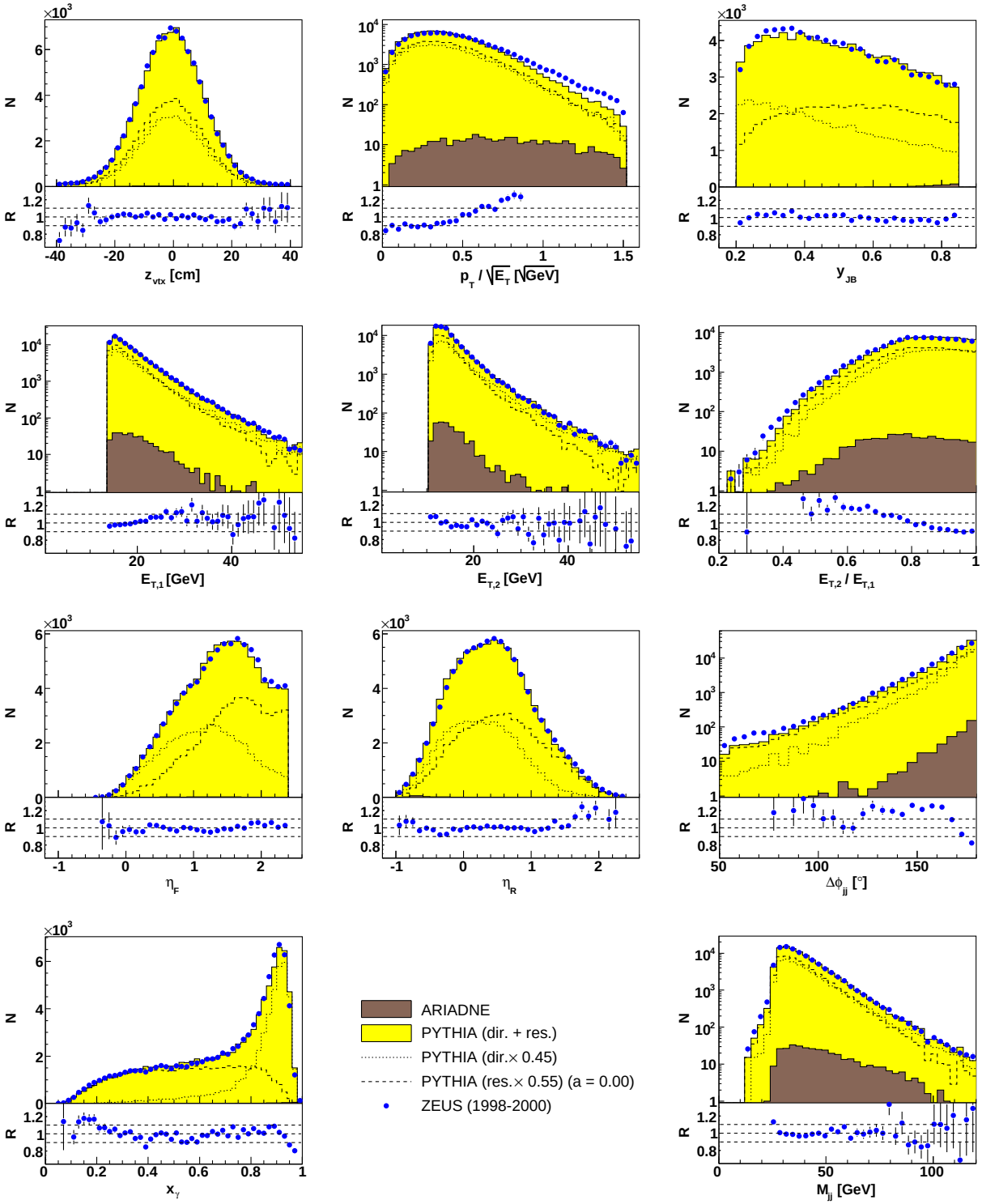

Figure A.1: Control plots for selection 1 before the reweighting with respect to x_γ^{true}. Shown are the number of selected events N and the ratio R = ZEUS / PYTHIA.

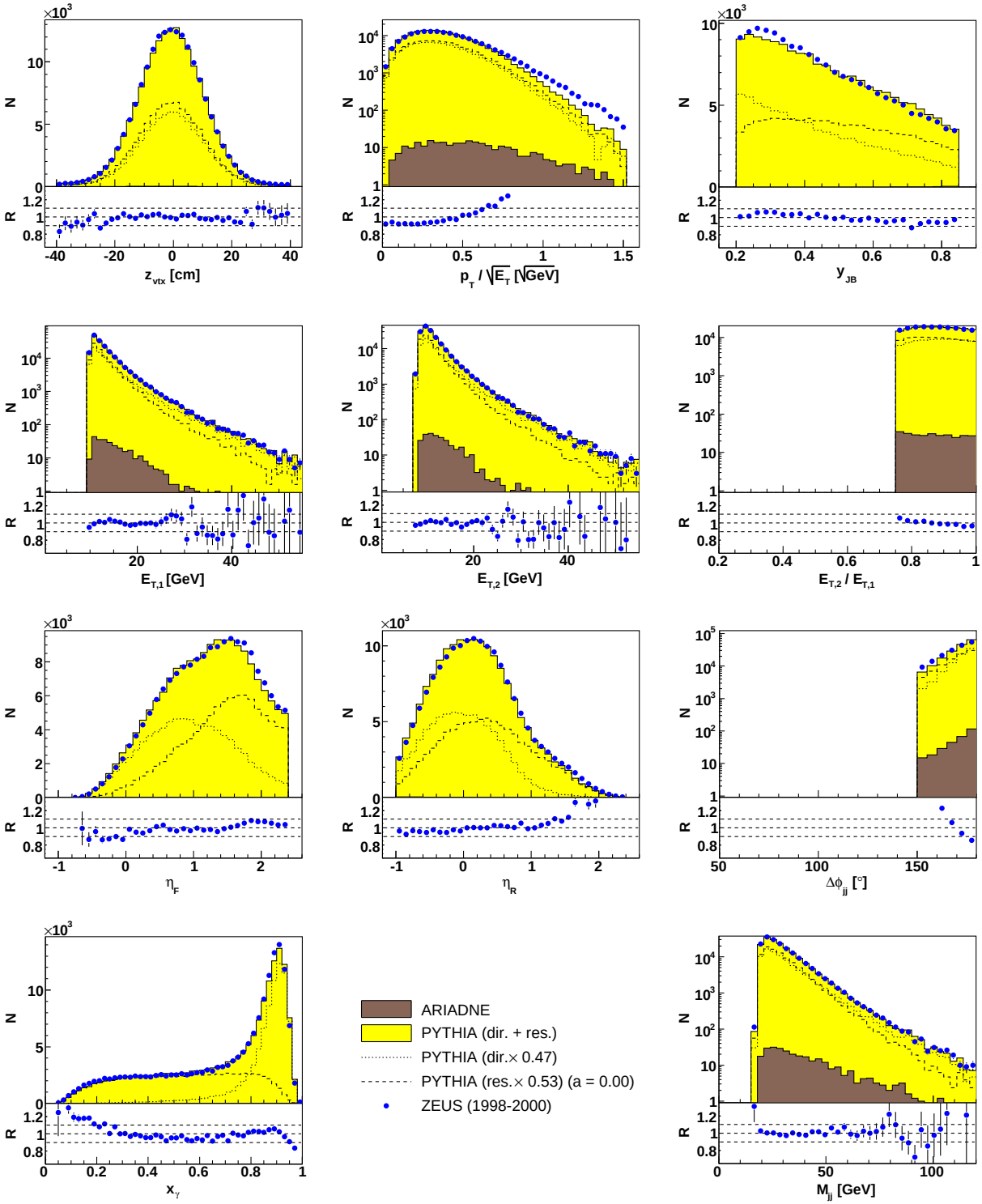

Figure A.2: Control plots for selection 2 before the reweighting with respect to x_γ^{true}. Shown are the number of selected events N and the ratio R = ZEUS / PYTHIA.

Appendix B

Unfolding

On the following pages, all histograms related to the unfolding of the data used in this thesis are provided. See chapter 6 for an explanation of the unfolding procedure.

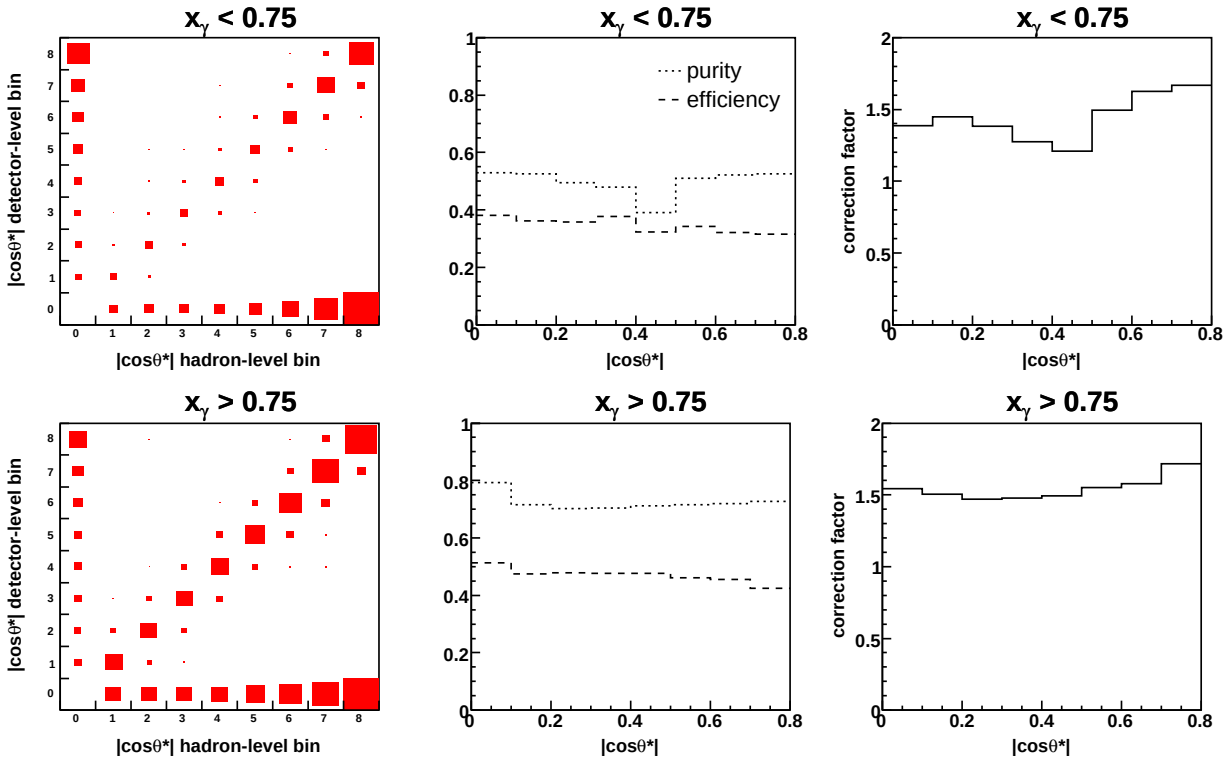

Figure B.1: Histograms for the unfolding for selection 1 as a function of $|\cos\theta^*|$ for the resolved-enriched region ($x_\gamma < 0.75$) and for the direct-enriched region ($x_\gamma > 0.75$). Shown are the migration matrix (left), the efficiencies and purities (center) and the correction factors (right).

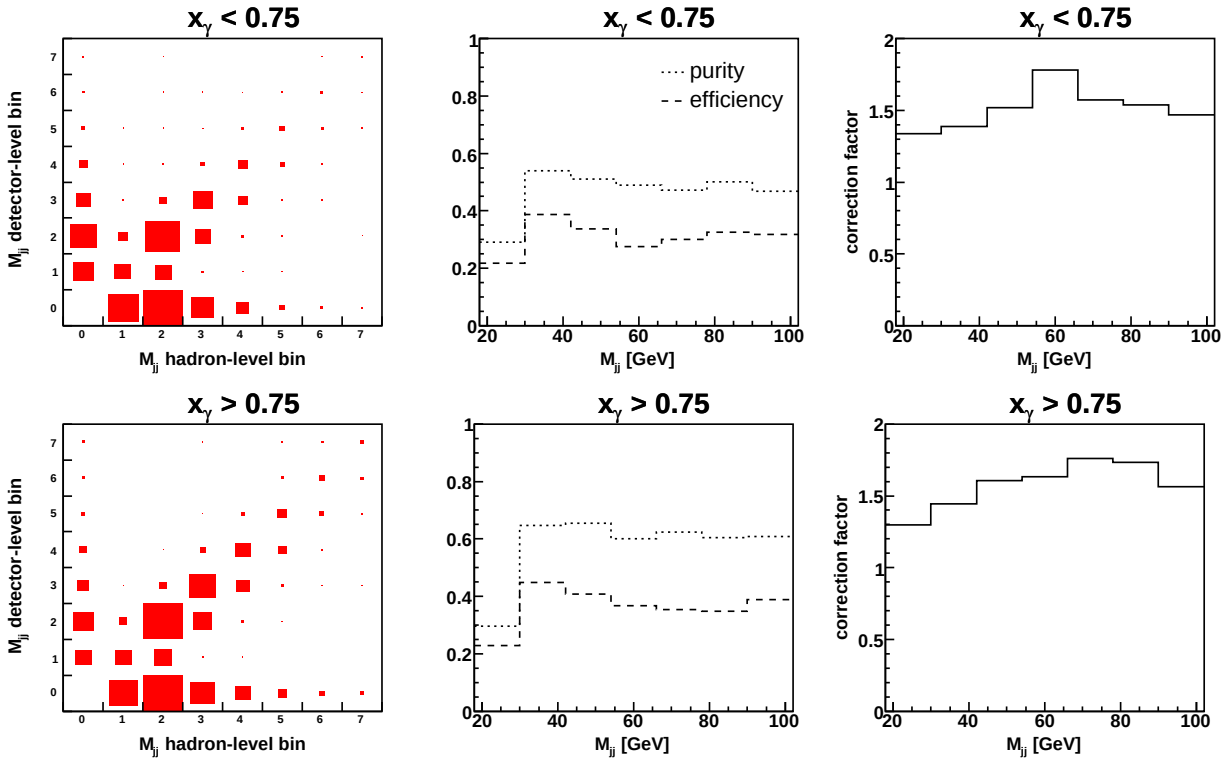

Figure B.2: Histograms for the unfolding for selection 1 as a function of M_{jj} for the resolved-enriched region ($x_\gamma < 0.75$) and for the direct-enriched region ($x_\gamma > 0.75$). See the caption to figure B.1 for further details.

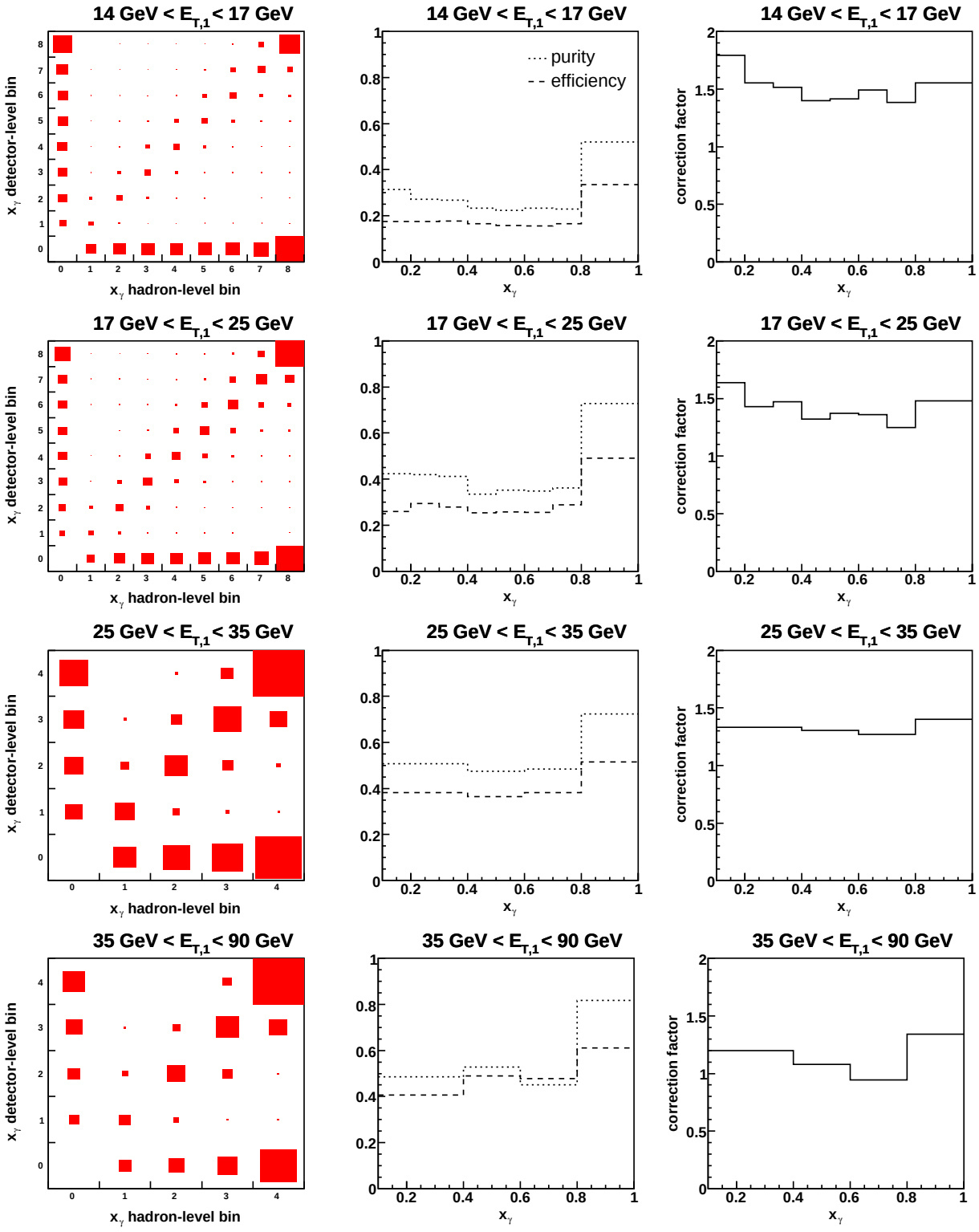

Figure B.3: Histograms for the unfolding for selection 1 as a function of x_γ in four different regions of the transverse energy of the leading jet, $E_{T,1}$. See the caption to figure B.1 for further details.

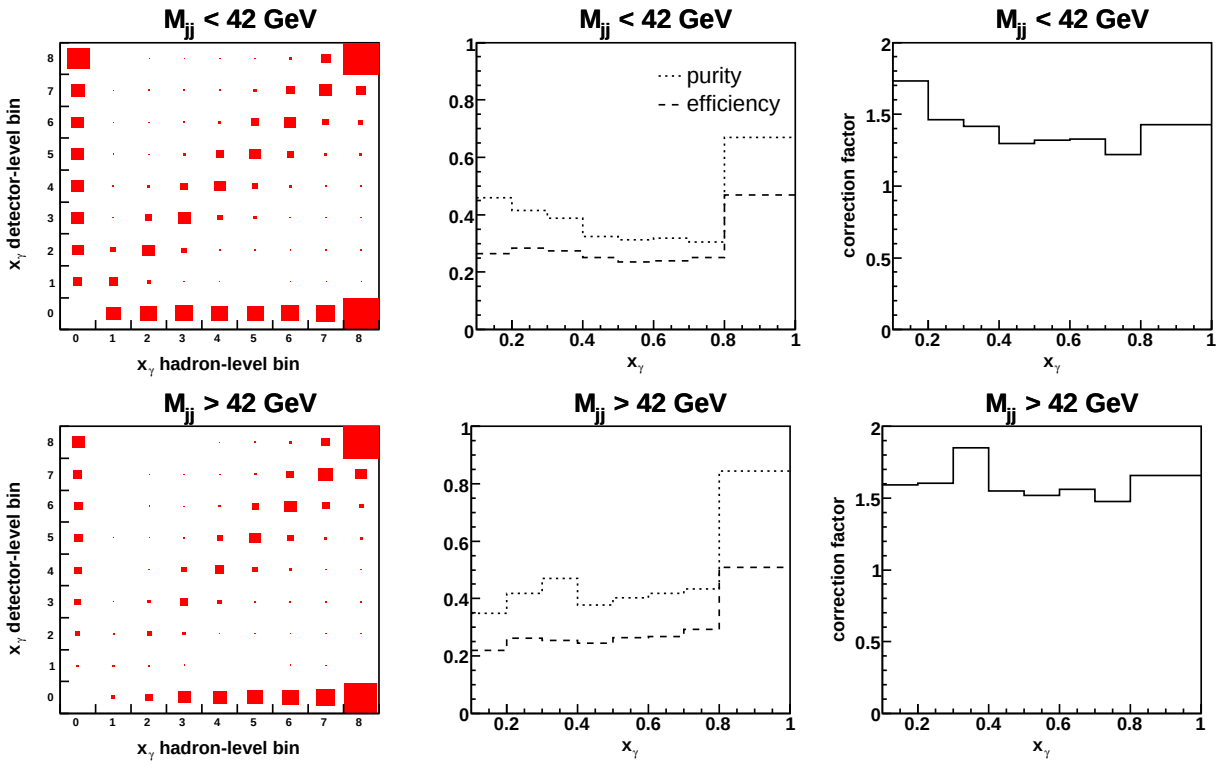

Figure B.4: Histograms for the unfolding for selection 1 as a function of x_γ for high and for low values of the dijet mass M_{jj}. See the caption to figure B.1 for further details.

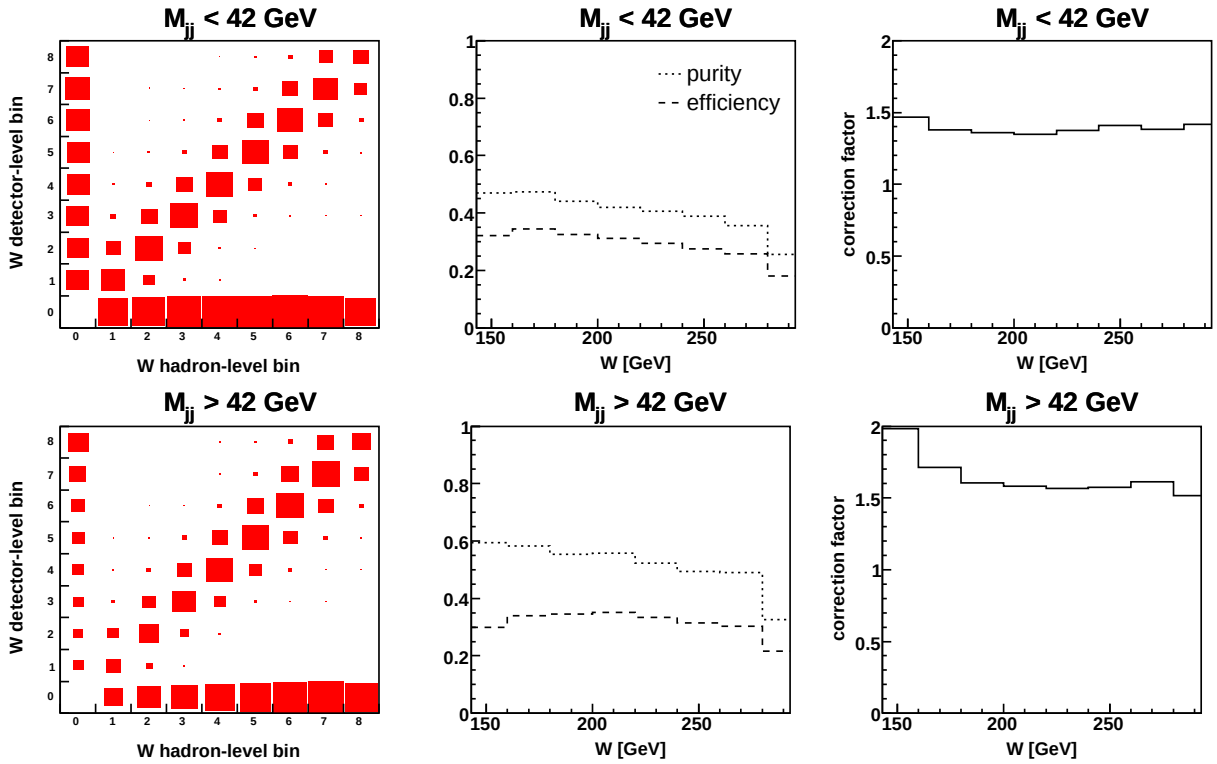

Figure B.5: Histograms for the unfolding for selection 1 as a function of W for for high and for low values of the dijet mass M_{jj}. See the caption to figure B.1 for further details.

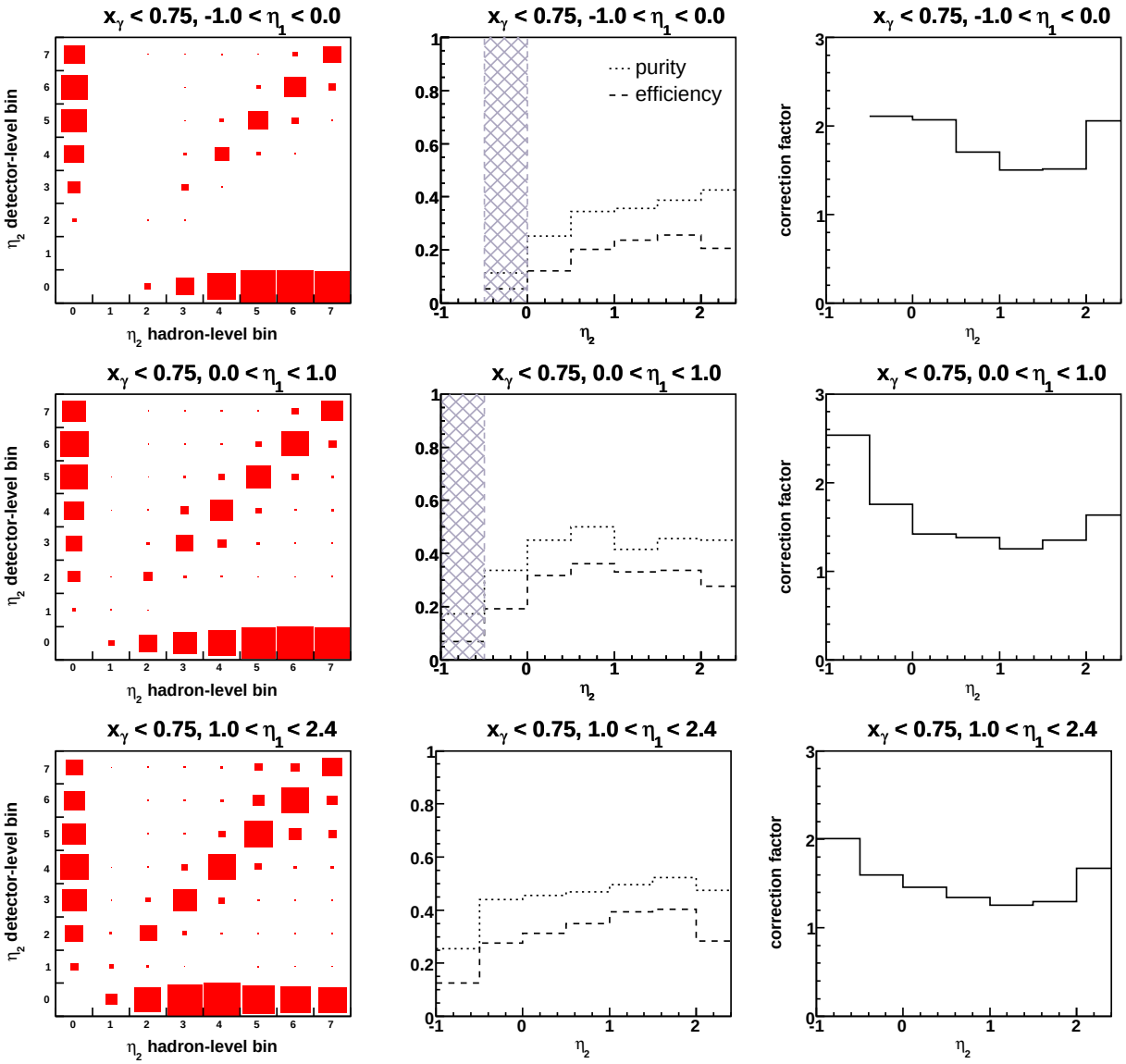

Figure B.6: Histograms for the unfolding for selection 1 as a function of η_2 for the resolved-enriched region ($x_\gamma < 0.75$) in three different regions of the pseudorapidity of the other jet, η_1. See the caption to figure B.1 for further details. A crosshatched area is used to indicate bins in which the efficiency is below 10%.

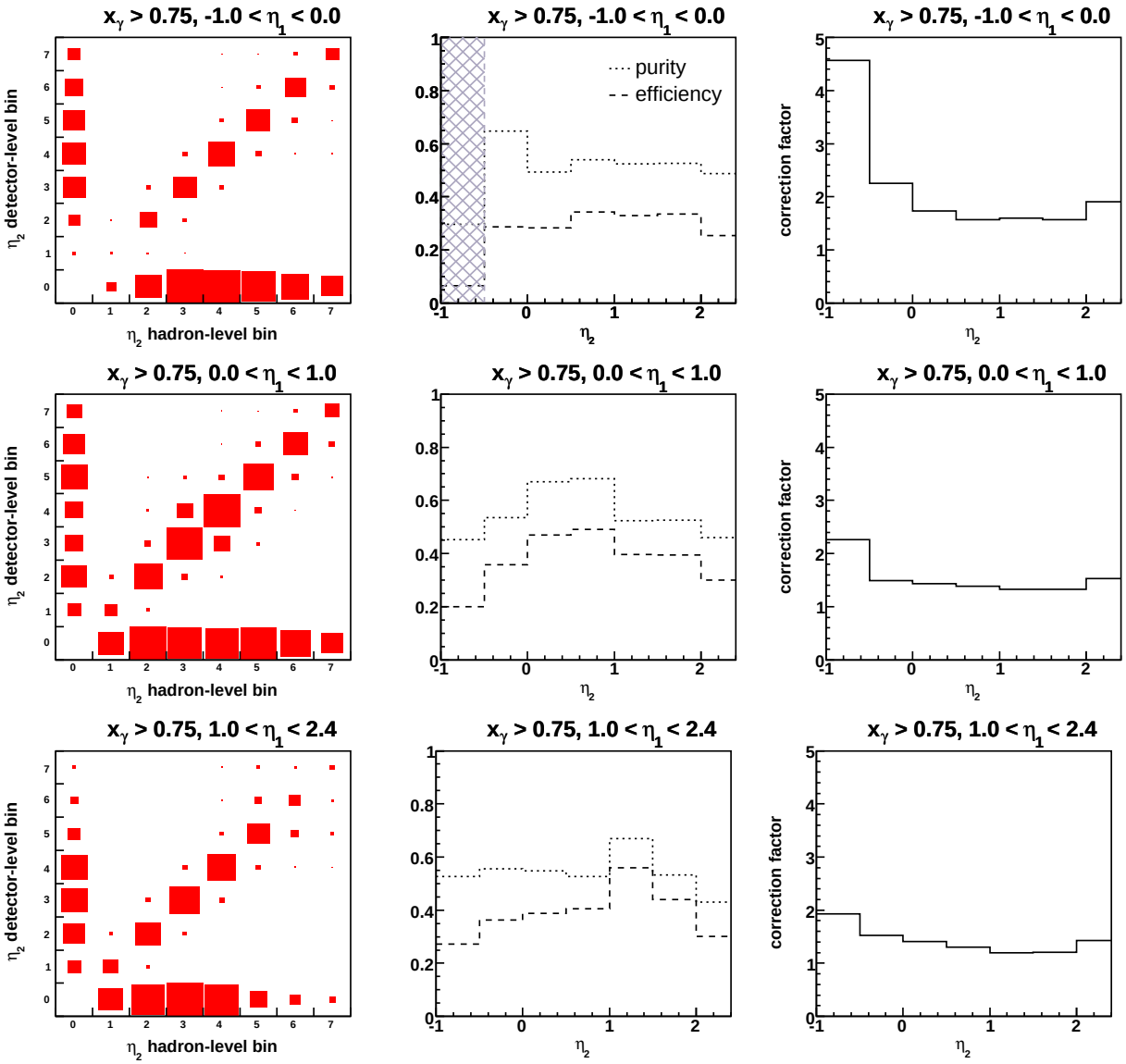

Figure B.7: Histograms for the unfolding for selection 1 as a function of η_2 for the direct-enriched region ($x_\gamma > 0.75$) in three different regions of the pseudorapidity of the other jet, η_1. See the caption to figure B.1 for further details. A crosshatched area is used to indicate bins in which the efficiency is below 10%.

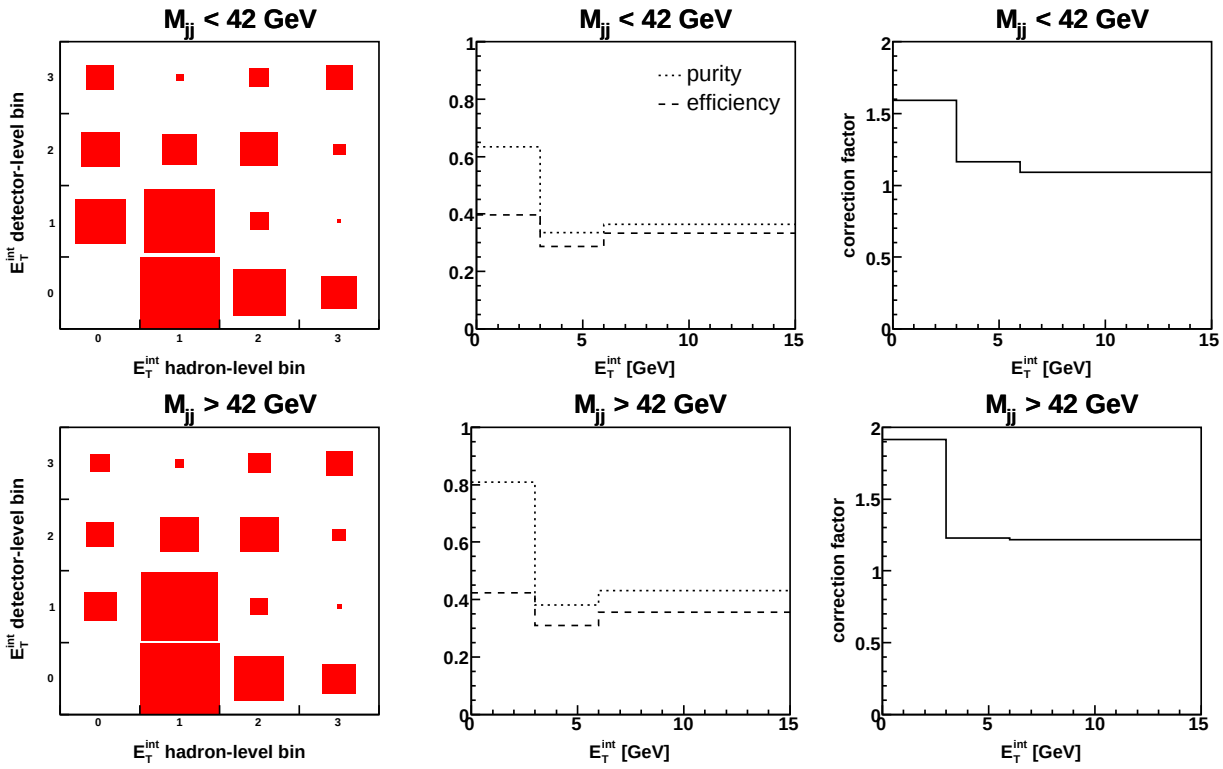

Figure B.8: Histograms for the unfolding for selection 1 as a function of E_T^{int} for high and for low values of the dijet mass M_{jj}. See the caption to figure B.1 for further details.

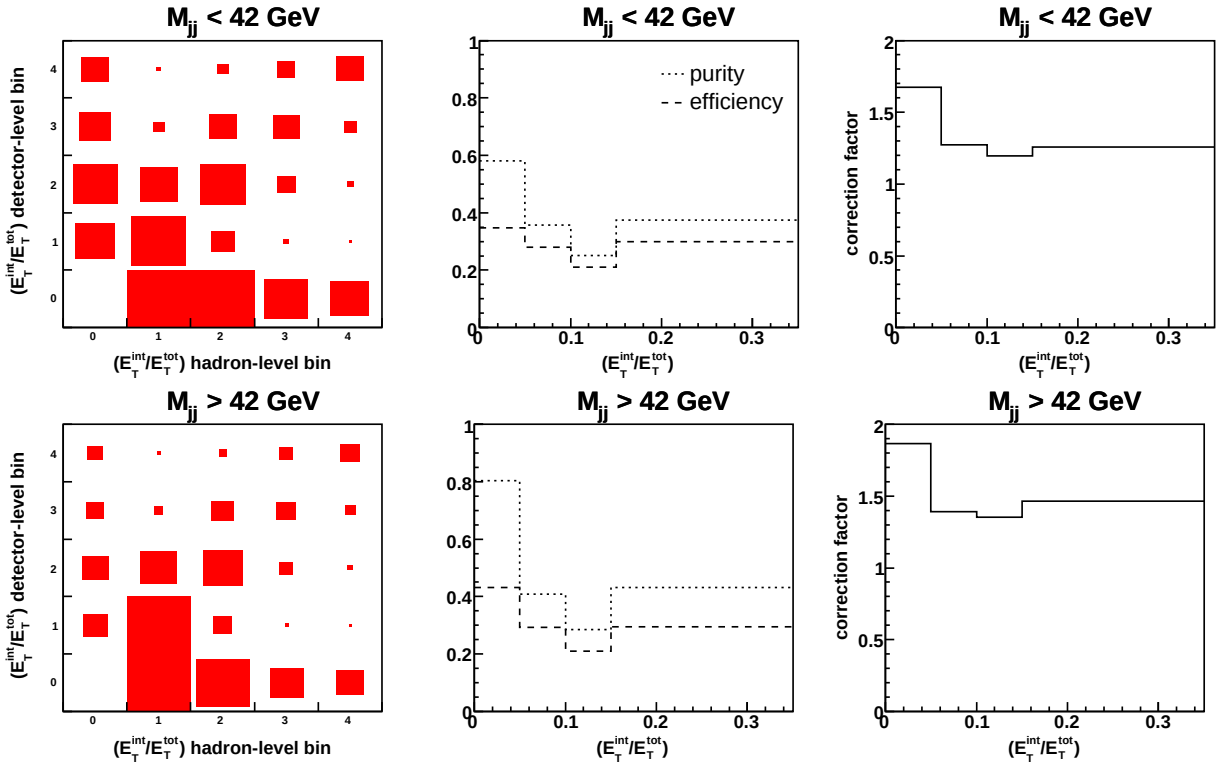

Figure B.9: Histograms for the unfolding for selection 1 as a function of the ratio $E_T^{\text{int}}/E_T^{\text{tot}}$ for high and for low values of the dijet mass M_{jj}. See the caption to figure B.1 for further details.

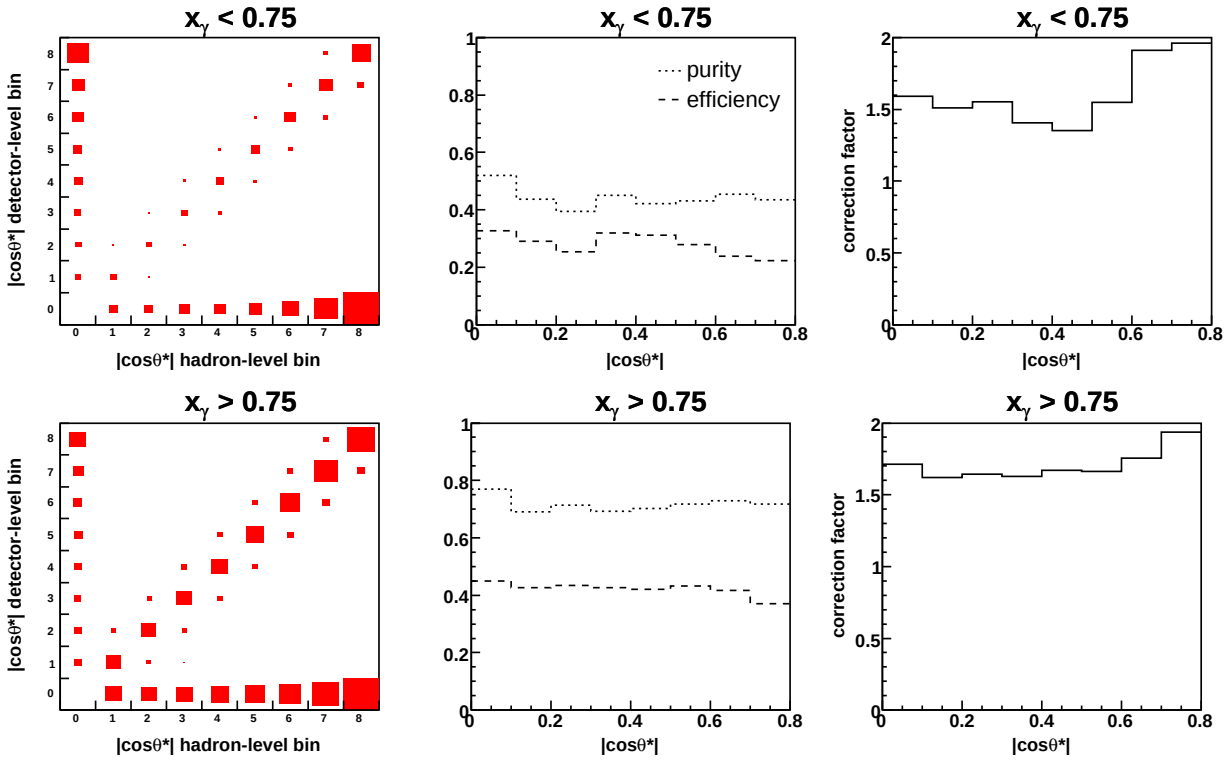

Figure B.10: Histograms for the unfolding for selection 2 as a function of $|\cos\theta^*|$ for the resolved-enriched region ($x_\gamma < 0.75$) and for the direct-enriched region ($x_\gamma > 0.75$). See the caption to figure B.1 for further details.

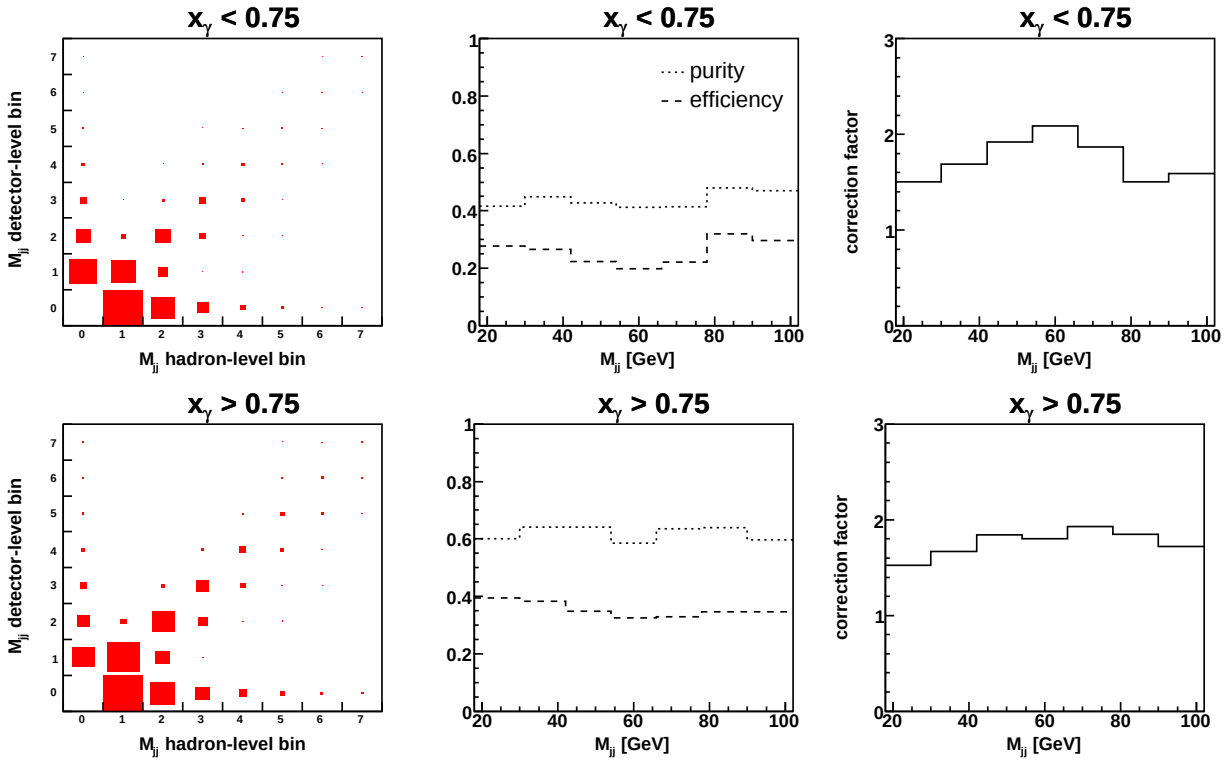

Figure B.11: Histograms for the unfolding for selection 2 as a function of M_{jj} for the resolved-enriched region ($x_\gamma < 0.75$) and for the direct-enriched region ($x_\gamma > 0.75$). See the caption to figure B.1 for further details.

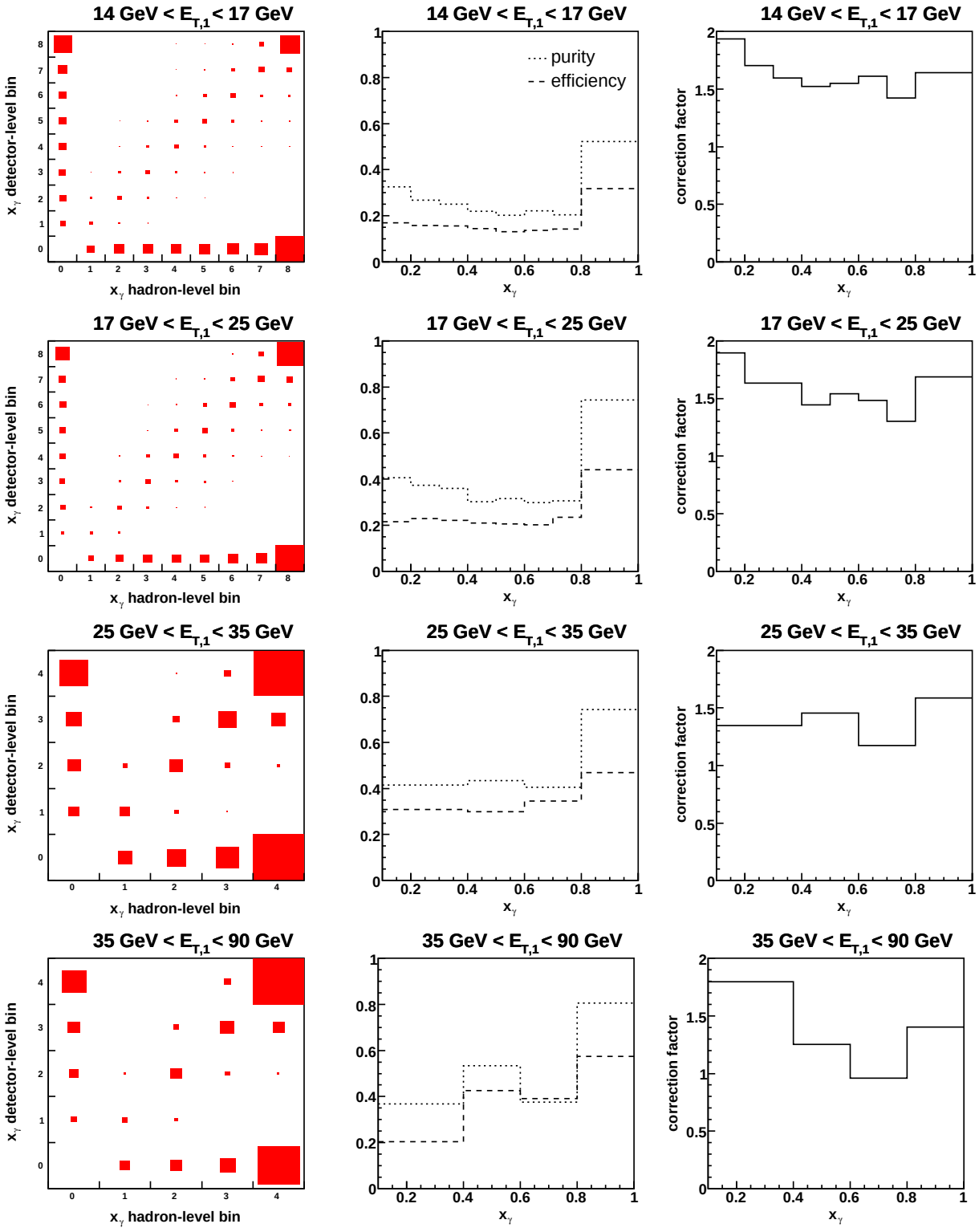

Figure B.12: Histograms for the unfolding for selection 2 as a function of x_γ in four different regions of the transverse energy of the leading jet, $E_{T,1}$. See the caption to figure B.1 for further details.

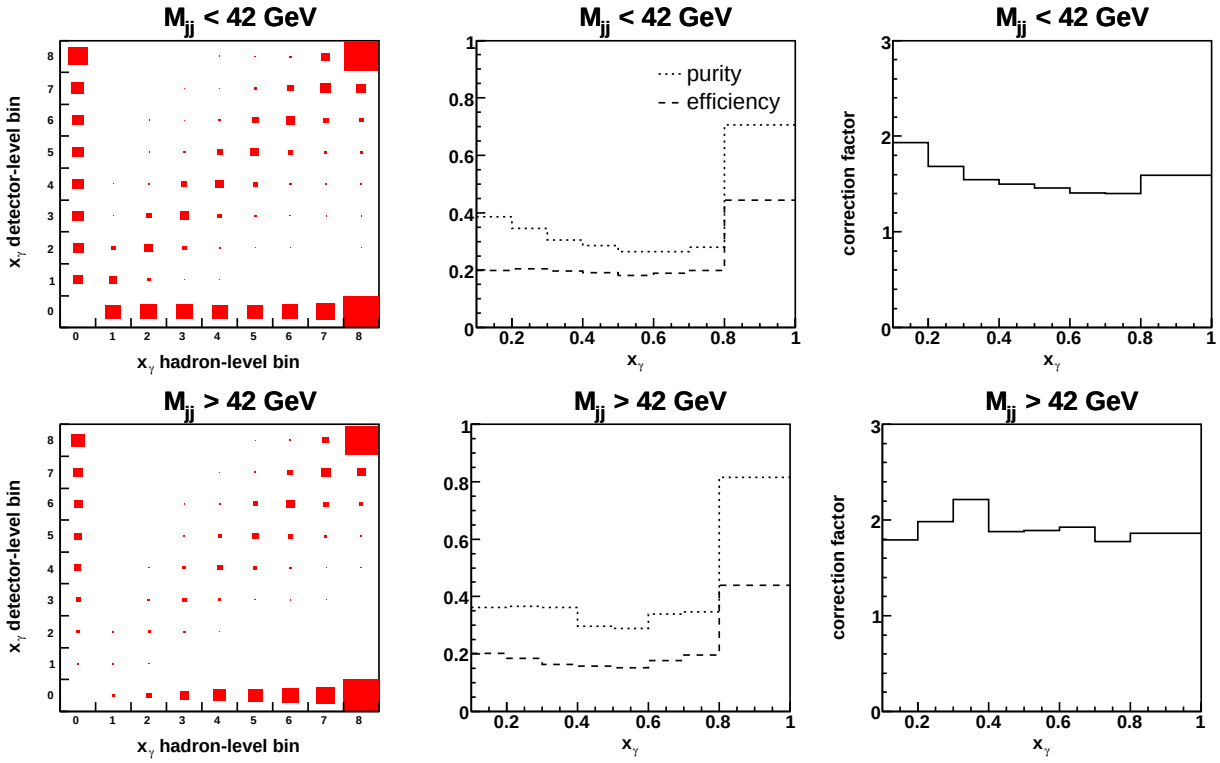

Figure B.13: Histograms for the unfolding for selection 2 as a function of x_γ for high and for low values of the dijet mass M_{jj}. See the caption to figure B.1 for further details.

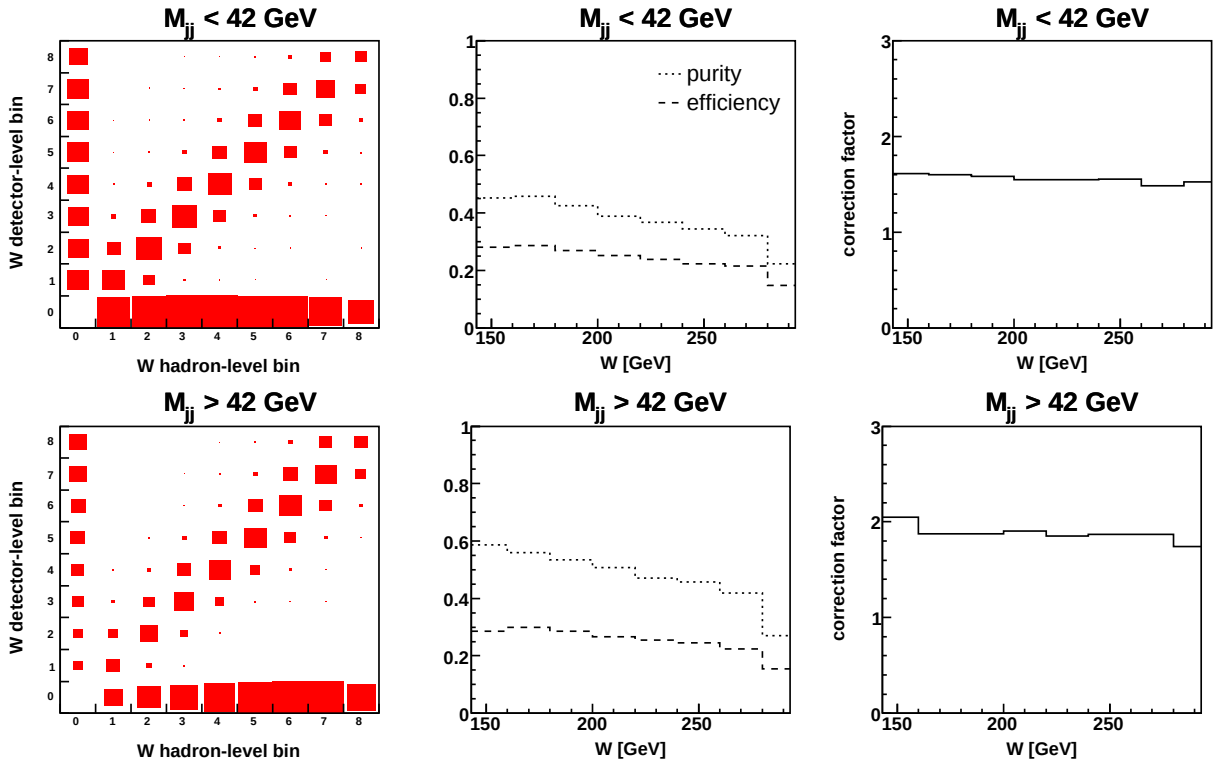

Figure B.14: Histograms for the unfolding for selection 2 as a function of W for for high and for low values of the dijet mass M_{jj}. See the caption to figure B.1 for further details.

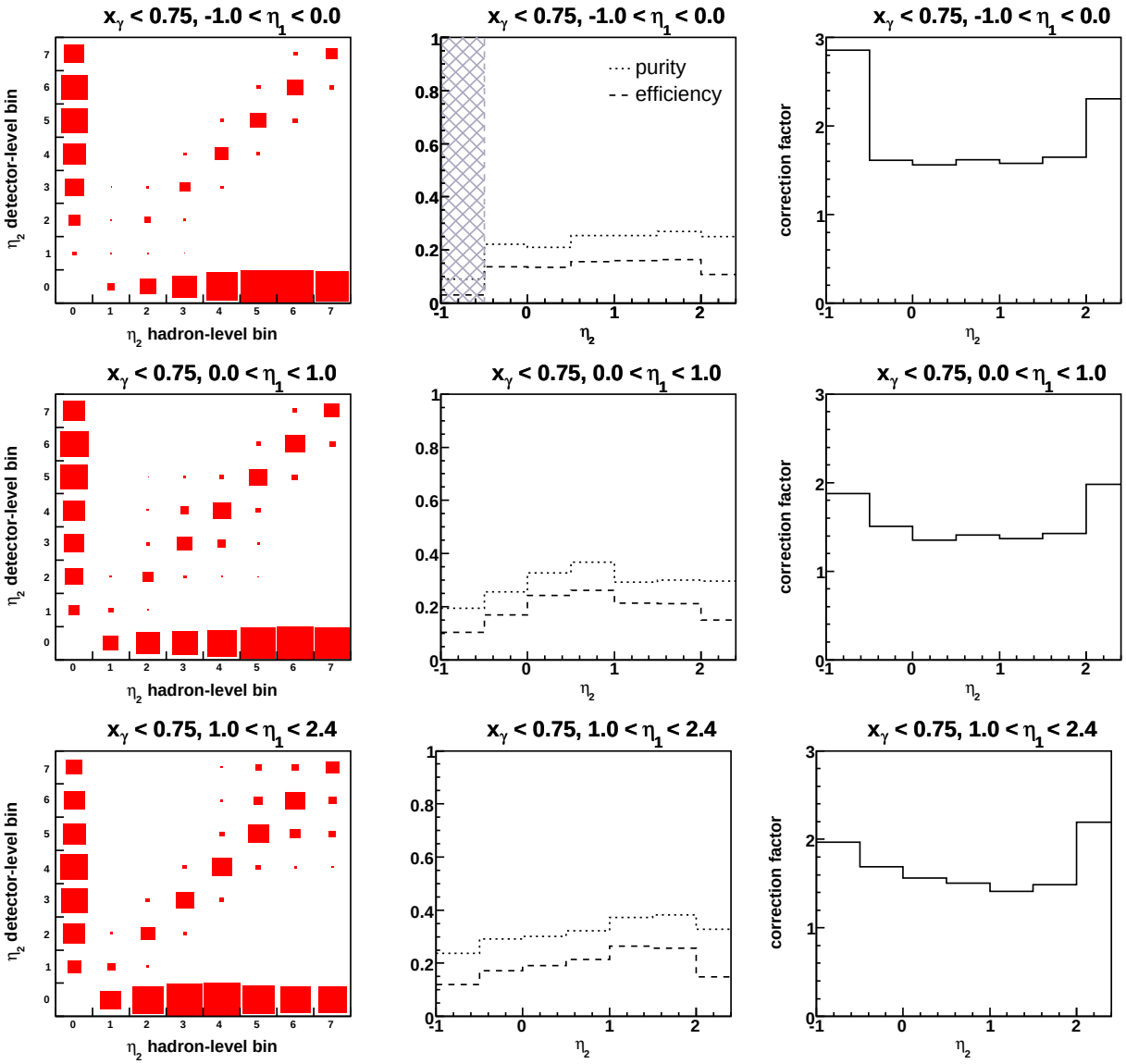

Figure B.15: Histograms for the unfolding for selection 2 as a function of η_2 for the resolved-enriched region ($x_\gamma < 0.75$) in three different regions of the pseudorapidity of the other jet, η_1. See the caption to figure B.1 for further details. A crosshatched area is used to indicate bins in which the efficiency is below 10%.

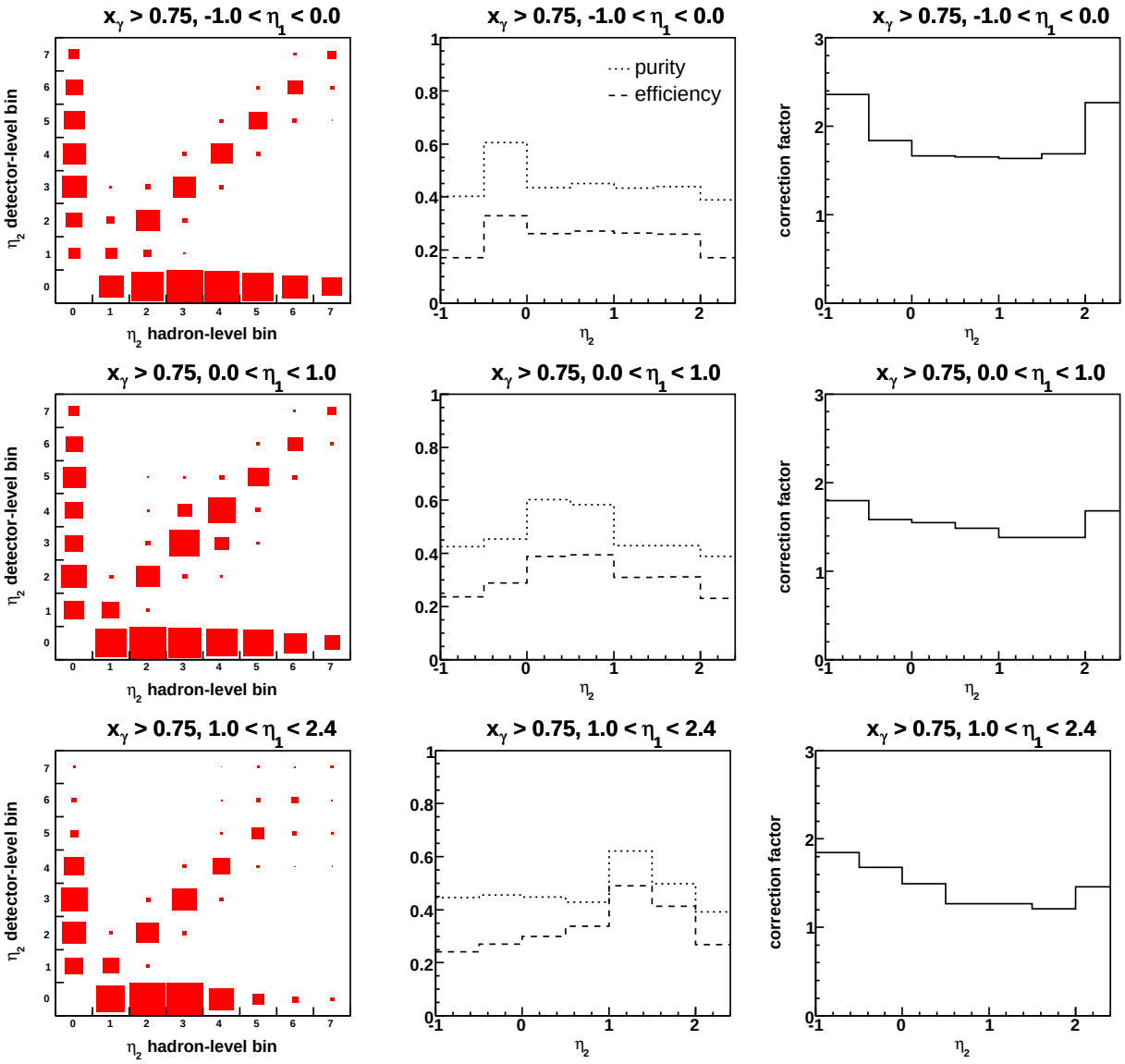

Figure B.16: Histograms for the unfolding for selection 2 as a function of η_2 for the direct-enriched region ($x_\gamma > 0.75$) in three different regions of the pseudorapidity of the other jet, η_1. See the caption to figure B.1 for further details.

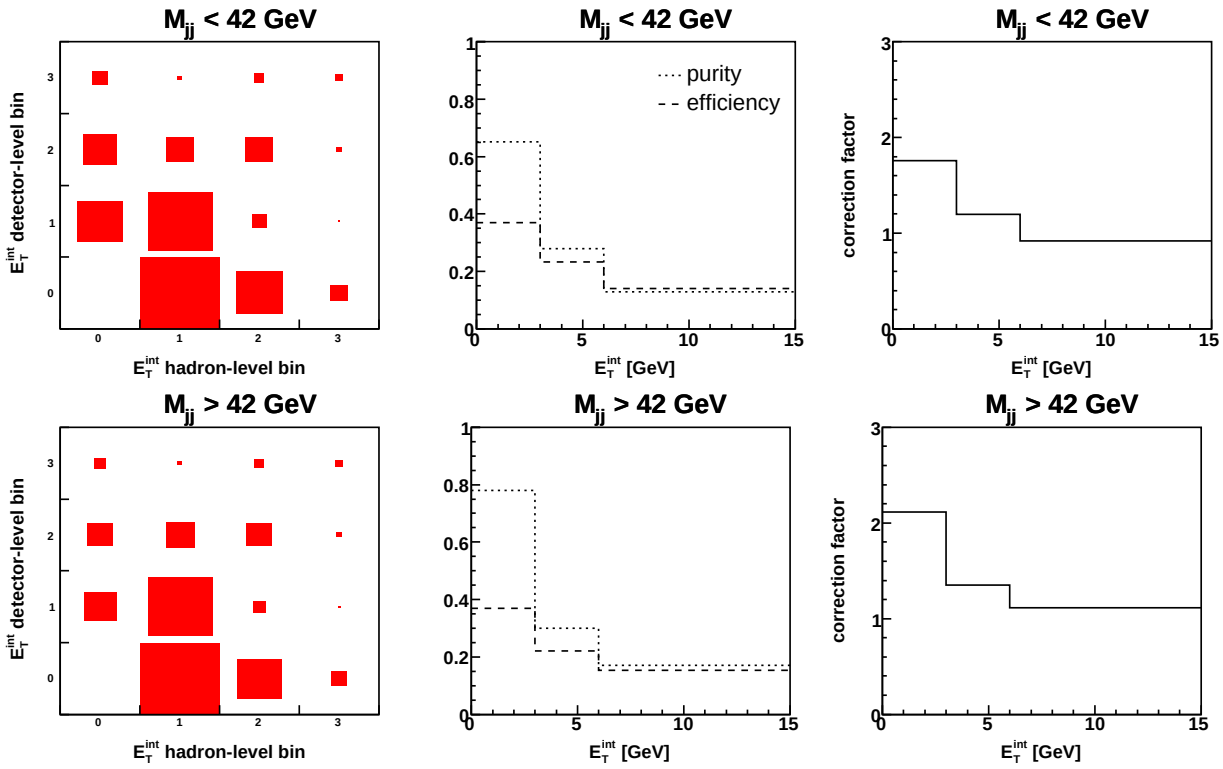

Figure B.17: Histograms for the unfolding for selection 2 as a function of E_T^{int} for high and for low values of the dijet mass M_{jj}. See the caption to figure B.1 for further details.

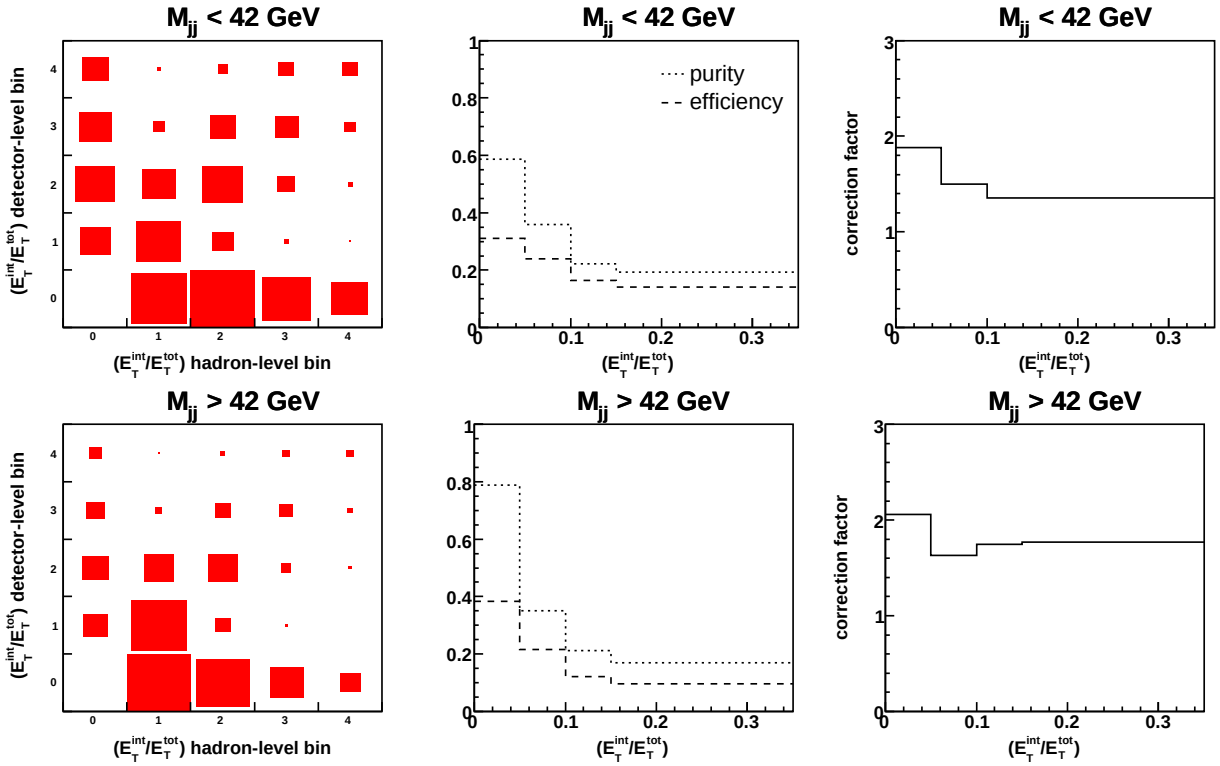

Figure B.18: Histograms for the unfolding for selection 2 as a function of the ratio $E_T^{\text{int}}/E_T^{\text{tot}}$ for high and for low values of the dijet mass M_{jj}. See the caption to figure B.1 for further details.

Appendix C

Cross Sections

Numerical values for all differential cross sections measured in this thesis and presented in section 7.1 can be found on the following pages.

$x_\gamma < 0.75$

$\lvert\cos\theta^*\rvert$ bin	$d\sigma/d\lvert\cos\theta^*\rvert \pm \Delta_{\text{stat}}$ [pb]			
	selection 1		selection 2	
0.0, 0.1	38.7	±4.5	18.1	±3.0
0.1, 0.2	38.7	±4.2	15.7	±2.7
0.2, 0.3	47.8	±4.8	18.6	±2.8
0.3, 0.4	56.3	±4.9	25.3	±3.2
0.4, 0.5	82.3	±6.1	37.4	±4.0
0.5, 0.6	127.2	±7.7	49.9	±4.6
0.6, 0.7	218.7	±10.3	84.7	±6.3
0.7, 0.8	411.8	±13.9	170.2	±8.9

$x_\gamma > 0.75$

$\lvert\cos\theta^*\rvert$ bin	$d\sigma/d\lvert\cos\theta^*\rvert \pm \Delta_{\text{stat}}$ [pb]			
	selection 1		selection 2	
0.0, 0.1	140.0	±8.7	101.0	±7.5
0.1, 0.2	142.5	±8.7	96.5	±7.1
0.2, 0.3	142.4	±8.5	107.4	±7.5
0.3, 0.4	174.5	±9.6	127.8	±8.3
0.4, 0.5	223.7	±11.0	169.9	±9.9
0.5, 0.6	304.0	±13.3	209.0	±11.0
0.6, 0.7	418.0	±15.5	291.8	±13.1
0.7, 0.8	718.2	±21.5	497.2	±18.1

Table C.1: Measured cross section for the two jet selections as a function of $\lvert\cos\theta^*\rvert$ for the resolved-enriched region ($x_\gamma < 0.75$) and for the direct-enriched region ($x_\gamma > 0.75$). Δ_{stat} refers to the statistical uncertainty.

$x_\gamma < 0.75$

M_{jj} bin [GeV]	$d\sigma/dM_{jj} \pm \Delta_{\text{stat}}$ [pb/GeV]			
	selection 1		selection 2	
18, 30	15.47	±0.24	87.19	±0.55
30, 42	33.90	±0.35	32.27	±0.34
42, 54	12.20	±0.22	7.87	±0.18
54, 66	4.15	±0.14	1.84	±0.09
66, 78	1.00	±0.06	0.43	±0.04
78, 90	0.32	±0.04	0.10	±0.02
90, 102	0.09	±0.02	0.03	±0.01

$x_\gamma > 0.75$

M_{jj} bin [GeV]	$d\sigma/dM_{jj} \pm \Delta_{\text{stat}}$ [pb/GeV]			
	selection 1		selection 2	
18, 30	10.97	±0.21	85.09	±0.61
30, 42	34.12	±0.39	45.21	±0.46
42, 54	17.14	±0.29	16.08	±0.29
54, 66	6.71	±0.18	5.04	±0.16
66, 78	2.69	±0.12	1.89	±0.10
78, 90	1.02	±0.07	0.69	±0.06
90, 102	0.33	±0.04	0.24	±0.03

Table C.2: Measured cross section for the two jet selections as a function of M_{jj} for the resolved-enriched region ($x_\gamma < 0.75$) and for the direct-enriched region ($x_\gamma > 0.75$). Δ_{stat} refers to the statistical uncertainty.

$14\,\text{GeV} < E_{T,1} < 17\,\text{GeV}$

x_γ bin	$d\sigma/dx_\gamma \pm \Delta_{\text{stat}}$ [pb]			
	selection 1		selection 2	
0.1, 0.2	383.0	±14.3	177.5	±9.2
0.2, 0.3	561.0	±16.2	280.8	±11.0
0.3, 0.4	618.6	±16.6	310.4	±11.3
0.4, 0.5	618.9	±16.4	330.9	±11.7
0.5, 0.6	646.2	±16.5	371.1	±12.5
0.6, 0.7	799.0	±19.4	461.9	±14.6
0.7, 0.8	957.4	±21.2	556.3	±15.6
0.8, 1.0	1772.2	±22.3	1488.8	±20.7

$17\,\text{GeV} < E_{T,1} < 25\,\text{GeV}$

x_γ bin	$d\sigma/dx_\gamma \pm \Delta_{\text{stat}}$ [pb]			
	selection 1		selection 2	
0.1, 0.2	233.4	±11.0	66.4	±5.7
0.2, 0.3	413.1	±13.7	120.7	±7.0
0.3, 0.4	524.8	±15.2	163.4	±8.3
0.4, 0.5	532.3	±15.0	169.2	±8.0
0.5, 0.6	592.1	±16.0	207.6	±9.4
0.6, 0.7	702.4	±17.9	241.1	±10.0
0.7, 0.8	828.1	±19.1	293.6	±10.7
0.8, 1.0	1637.4	±21.4	1099.6	±17.8

$25\,\text{GeV} < E_{T,1} < 35\,\text{GeV}$

x_γ bin	$d\sigma/dx_\gamma \pm \Delta_{\text{stat}}$ [pb]			
	selection 1		selection 2	
0.1, 0.4	47.1	±2.7	8.9	±1.1
0.4, 0.6	103.9	±5.0	29.1	±2.5
0.6, 0.8	147.3	±5.9	36.4	±2.5
0.8, 1.0	337.5	±9.6	212.7	±7.7

$35\,\text{GeV} < E_{T,1} < 90\,\text{GeV}$

x_γ bin	$d\sigma/dx_\gamma \pm \Delta_{\text{stat}}$ [pb]			
	selection 1		selection 2	
0.1, 0.4	4.7	±0.8	0.8	±0.3
0.4, 0.6	14.0	±1.7	3.8	±0.8
0.6, 0.8	24.7	±2.2	6.9	±1.1
0.8, 1.0	78.1	±4.4	50.9	±3.5

Table C.3: Measured cross section for the two jet selections as a function of x_γ in four different regions of the transverse energy of the leading jet, $E_{T,1}$. Δ_{stat} refers to the statistical uncertainty.

$M_{jj} < 42\,\text{GeV}$

x_γ bin	$d\sigma/dx_\gamma \pm \Delta_{\text{stat}}$ [pb]			
	selection 1		selection 2	
0.1, 0.2	614.0	±18.1	1810.1	±29.6
0.2, 0.3	902.6	±20.2	2218.0	±31.0
0.3, 0.4	968.7	±20.4	2146.1	±29.4
0.4, 0.5	929.6	±19.8	2119.7	±29.1
0.5, 0.6	927.9	±19.8	2118.3	±28.9
0.6, 0.7	1047.8	±21.7	2310.7	±30.4
0.7, 0.8	1200.2	±23.0	3182.6	±37.3
0.8, 1.0	2358.4	±25.1	6886.1	±43.5

$M_{jj} > 42\,\text{GeV}$

x_γ bin	$d\sigma/dx_\gamma \pm \Delta_{\text{stat}}$ [pb]			
	selection 1		selection 2	
0.1, 0.2	21.8	±3.2	9.9	±2.1
0.2, 0.3	114.9	±7.5	47.3	±4.9
0.3, 0.4	270.6	±11.8	118.8	±8.0
0.4, 0.5	323.2	±12.0	168.5	±8.6
0.5, 0.6	441.0	±14.1	263.3	±11.1
0.6, 0.7	597.7	±17.1	369.5	±13.3
0.7, 0.8	789.2	±19.7	540.6	±16.4
0.8, 1.0	1478.0	±21.3	1310.5	±20.5

Table C.4: Measured cross section for the two jet selections as a function of x_γ for low and for high values of the dijet mass M_{jj}. Δ_{stat} refers to the statistical uncertainty.

$M_{jj} < 42\,\text{GeV}$

W bin [GeV]	$d\sigma/dW \pm \Delta_{\text{stat}}$ [pb/GeV]	
	selection 1	selection 2
143, 160	6.47 ±0.14	21.17 ±0.26
160, 180	7.48 ±0.14	23.42 ±0.25
180, 200	8.02 ±0.14	23.36 ±0.24
200, 220	7.92 ±0.14	22.04 ±0.23
220, 240	8.09 ±0.14	20.21 ±0.22
240, 260	7.85 ±0.14	18.40 ±0.20
260, 280	7.07 ±0.13	15.10 ±0.18
280, 293	6.87 ±0.16	13.11 ±0.21

$M_{jj} > 42\,\text{GeV}$

W bin [GeV]	$d\sigma/dW \pm \Delta_{\text{stat}}$ [pb/GeV]	
	selection 1	selection 2
143, 160	1.54 ±0.08	1.16 ±0.07
160, 180	2.61 ±0.09	1.92 ±0.08
180, 200	3.20 ±0.10	2.54 ±0.09
200, 220	3.75 ±0.10	3.06 ±0.10
220, 240	4.25 ±0.11	3.29 ±0.10
240, 260	4.55 ±0.11	3.58 ±0.10
260, 280	4.86 ±0.11	3.42 ±0.10
280, 293	4.53 ±0.13	2.84 ±0.10

Table C.5: Measured cross section for the two jet selections as a function of W for low and for high values of the dijet mass M_{jj}. Δ_{stat} refers to the statistical uncertainty.

$x_\gamma < 0.75$, $1.0 < \eta_1 < 2.4$

η_2 bin	$d\sigma/d\eta_2 \pm \Delta_{\text{stat}}$ [pb]			
	selection 1		selection 2	
-1.0, -0.5	21.8	±1.5	136.8	±3.5
-0.5, 0.0	150.6	±3.6	363.0	±5.5
0.0, 0.5	306.7	±5.2	575.0	±6.9
0.5, 1.0	400.8	±5.9	665.8	±7.4
1.0, 1.5	382.2	±5.7	578.5	±6.7
1.5, 2.0	370.7	±5.7	573.3	±6.9
2.0, 2.4	337.0	±6.7	546.7	±8.7

$x_\gamma > 0.75$, $1.0 < \eta_1 < 2.4$

η_2 bin	$d\sigma/d\eta_2 \pm \Delta_{\text{stat}}$ [pb]			
	selection 1		selection 2	
-1.0, -0.5	117.7	±4.0	329.2	±6.4
-0.5, 0.0	246.4	±5.3	526.2	±7.8
0.0, 0.5	315.8	±5.9	566.9	±7.8
0.5, 1.0	262.8	±5.1	248.7	±4.8
1.0, 1.5	102.4	±3.0	77.0	±2.6
1.5, 2.0	34.9	±1.7	26.9	±1.5
2.0, 2.4	12.1	±1.2	9.2	±1.1

$x_\gamma < 0.75$, $0.0 < \eta_1 < 1.0$

η_2 bin	$d\sigma/d\eta_2 \pm \Delta_{\text{stat}}$ [pb]			
	selection 1		selection 2	
-1.0, -0.5	(3.8	±0.7)	64.4	±2.5
-0.5, 0.0	59.0	±2.6	181.3	±3.9
0.0, 0.5	123.1	±3.4	266.5	±4.6
0.5, 1.0	187.5	±4.2	350.3	±5.3
1.0, 1.5	226.5	±4.3	421.7	±5.7
1.5, 2.0	271.7	±4.8	463.5	±6.0
2.0, 2.4	260.9	±5.6	437.0	±7.3

$x_\gamma > 0.75$, $0.0 < \eta_1 < 1.0$

η_2 bin	$d\sigma/d\eta_2 \pm \Delta_{\text{stat}}$ [pb]			
	selection 1		selection 2	
-1.0, -0.5	100.6	±3.9	396.1	±6.8
-0.5, 0.0	256.8	±5.2	599.8	±8.0
0.0, 0.5	339.2	±6.1	706.5	±8.8
0.5, 1.0	337.6	±6.0	624.4	±8.1
1.0, 1.5	273.8	±5.2	416.3	±6.4
1.5, 2.0	205.0	±4.6	277.2	±5.4
2.0, 2.4	125.1	±4.3	152.4	±4.8

$x_\gamma < 0.75$, $-1.0 < \eta_1 < 0.0$

η_2 bin	$d\sigma/d\eta_2 \pm \Delta_{\text{stat}}$ [pb]			
	selection 1		selection 2	
-1.0, -0.5	——	——	(7.1	±1.0)
-0.5, 0.0	(1.8	±0.5)	37.5	±1.8
0.0, 0.5	20.4	±1.7	96.0	±2.9
0.5, 1.0	43.1	±2.1	151.0	±3.6
1.0, 1.5	55.2	±2.1	173.0	±3.7
1.5, 2.0	64.3	±2.3	189.1	±3.9
2.0, 2.4	67.0	±3.0	173.4	±4.8

$x_\gamma > 0.75$, $-1.0 < \eta_1 < 0.0$

η_2 bin	$d\sigma/d\eta_2 \pm \Delta_{\text{stat}}$ [pb]			
	selection 1		selection 2	
-1.0, -0.5	(7.5	±1.4)	197.6	±5.3
-0.5, 0.0	86.8	±3.6	416.1	±6.9
0.0, 0.5	171.6	±4.6	515.0	±7.5
0.5, 1.0	184.6	±4.5	481.0	±7.3
1.0, 1.5	165.2	±4.4	394.9	±6.6
1.5, 2.0	126.8	±3.9	298.7	±5.9
2.0, 2.4	91.0	±4.0	209.3	±6.3

Table C.6: Measured cross section for the two jet selections as a function of η_2 for the resolved-enriched region ($x_\gamma < 0.75$) and for the direct-enriched region ($x_\gamma > 0.75$). The measurement is divided into three different regions of the pseudorapidity of the other jet, η_1. Δ_{stat} refers to the statistical uncertainty. Cross sections for bins in which the efficiency is below 10% are quoted in brackets.

$M_{jj} < 42\,\text{GeV}$

E_T^{int} bin [GeV]	$d\sigma/dE_T^{\text{int}} \pm \Delta_{\text{stat}}$ [pb/GeV]			
	selection 1		selection 2	
0, 3	229.07	±2.02	752.04	±3.68
3, 6	87.42	±1.07	210.20	±1.58
6, 15	17.10	±0.29	11.18	±0.21

$M_{jj} > 42\,\text{GeV}$

E_T^{int} bin [GeV]	$d\sigma/dE_T^{\text{int}} \pm \Delta_{\text{stat}}$ [pb/GeV]			
	selection 1		selection 2	
0, 3	122.67	±1.62	109.90	±1.56
3, 6	37.80	±0.71	25.73	±0.59
6, 15	7.03	±0.19	1.06	±0.06

Table C.7: Measured cross section for the two jet selections as a function of E_T^{int} for low and for high values of the dijet mass M_{jj}. Δ_{stat} refers to the statistical uncertainty.

$M_{jj} < 42\,\text{GeV}$

$(E_T^{\text{int}}/E_T^{\text{tot}})$ bin	$d\sigma/d(E_T^{\text{int}}/E_T^{\text{tot}}) \pm \Delta_{\text{stat}}$ [pb]			
	selection 1		selection 2	
0.00, 0.05	8750.7	±100.2	20987.4	±158.9
0.05, 0.10	7070.1	±77.4	21923.4	±141.6
0.10, 0.15	3331.1	±52.2	10835.8	±92.6
0.15, 0.35	813.0	±14.3	1575.9	±18.1

$M_{jj} > 42\,\text{GeV}$

$(E_T^{\text{int}}/E_T^{\text{tot}})$ bin	$d\sigma/d(E_T^{\text{int}}/E_T^{\text{tot}}) \pm \Delta_{\text{stat}}$ [pb]			
	selection 1		selection 2	
0.00, 0.05	5924.3	±87.4	4830.7	±80.4
0.05, 0.10	2993.2	±51.8	2370.5	±47.8
0.10, 0.15	1175.5	±32.6	832.2	±28.2
0.15, 0.35	231.6	±7.9	68.0	±4.0

Table C.8: Measured cross section for the two jet selections as a function of the ratio $E_T^{\text{int}}/E_T^{\text{tot}}$ for low and for high values of the dijet mass M_{jj}. Δ_{stat} refers to the statistical uncertainty.

Appendix D

Error Propagation

In section 7.2, parameters in PYTHIA are tuned by performing χ^2-tests to quantify the agreement between the MC prediction and the cross section measured in ZEUS data. In this appendix, the derivation of uncertainties on the tuned quantities is explained.

For large numbers of degrees of freedom, NDF, the χ^2 probability density function approaches a Gaussian with a mean at the value of NDF and a variance of $\sigma^2 = 2 \cdot \text{NDF}$. Since NDF = 4 in this analysis, an error of $\pm\sqrt{8}$ is assumed on all χ^2-values, although this is only a poor estimate for such a low NDF.

The χ^2-values obtained for PYTHIA samples with different `PARP(81)` but identical settings for all other parameters are fitted with a parabolic function (cf. figure 7.19):

$$y = p_0 + p_1 \cdot x + p_2 \cdot x^2 \tag{D.1}$$

The parameters p_0, p_1 and p_2 are returned by the fitting algorithm together with a 3×3 covariance matrix V, specifying the uncertainties on the three parameters and the correlations between them. The coordinates of the minimum of the parabola can be calculated from the zero of the first derivative of the polynomial in equation D.1:

$$x_{\min} = \frac{-p_1}{2p_2} \tag{D.2}$$

$$y_{\min} = p_0 - \frac{p_1^2}{4p_2} \tag{D.3}$$

The uncertainties on $x_{\min}$ and $y_{\min}$ can be approximated using error propagation based on the elements of the symmetric matrix V [50]:

$$\begin{aligned} (\Delta x_{\min})^2 &\approx \sum_{k,l} \frac{\partial x_{\min}}{\partial p_k} \frac{\partial x_{\min}}{\partial p_l} V_{kl} \\ &= \frac{1}{4p_2^2} \left(V_{11} + \left(\frac{p_1}{p_2}\right)^2 V_{22} - \frac{2p_1}{p_2} V_{12} \right) \end{aligned} \tag{D.4}$$

$$
\begin{aligned}
(\Delta y_{\min})^2 &\approx \sum_{k,l} \frac{\partial y_{\min}}{\partial p_k} \frac{\partial y_{\min}}{\partial p_l} V_{kl} \\
&= V_{00} + \left(\frac{p_1}{2p_2}\right)^2 V_{11} + \left(\frac{p_1}{2p_2}\right)^4 V_{22} \\
&\quad -\frac{p_1}{p_2} V_{01} + \frac{1}{2}\left(\frac{p_1}{p_2}\right)^2 V_{02} - \frac{1}{4}\left(\frac{p_1}{p_2}\right)^3 V_{12}
\end{aligned} \tag{D.5}
$$

The best value for $p_{T,\min}^{\mathrm{MPI}}$ is calculated from `PARP(81)` at $x_{\min}$, i.e. where the χ^2 is supposed to be minimized, using PYTHIA's energy-rescaling term (cf. equation 3.1):

$$
p_{T,\min}^{\mathrm{MPI}} = x_{\min} \cdot \left(\frac{\langle W \rangle}{1\,\mathrm{TeV}}\right)^{\texttt{PARP(90)}} \tag{D.6}
$$

Assuming that the uncertainties on $x_{\min}$ and $\langle W \rangle$ are uncorrelated, the error propagation for the uncertainty on $p_{T,\min}^{\mathrm{MPI}}$ finally gives:

$$
\begin{aligned}
\left(\Delta p_{T,\min}^{\mathrm{MPI}}\right)^2 &\approx \left(\left(\frac{\langle W \rangle}{1\,\mathrm{TeV}}\right)^{\texttt{PARP(90)}} \cdot \Delta x_{\min}\right)^2 \\
&\quad + \left(x_{\min} \cdot \texttt{PARP(90)} \cdot \left(\frac{\langle W \rangle}{1\,\mathrm{TeV}}\right)^{\texttt{PARP(90)} - 1} \cdot \Delta W\right)^2
\end{aligned} \tag{D.7}
$$

Bibliography

[1] R. K. Ellis, W. J. Stirling and B. R. Webber. *QCD and collider physics*. Camb. Monogr. Part. Phys. Nucl. Phys. Cosmol., vol. 8, p. 1, 1996.

[2] S. Bethke. *Experimental tests of asymptotic freedom*. 2006. {hep-ex/0606035}.

[3] M. Gell-Mann. *A schematic model of baryons and mesons*. Phys. Lett., vol. 8, p. 214, 1964.

[4] G. Zweig. *An SU(3) model for strong interaction symmetry and its breaking*. 1964. CERN-TH-401.

[5] O. W. Greenberg. *Spin and unitary spin independence in a paraquark model of baryons and mesons*. Phys. Rev. Lett., vol. 13, p. 598, 1964.

[6] M. Y. Han and Y. Nambu. *Three-triplet model with double SU(3) symmetry*. Phys. Rev., vol. 139, p. B1006, 1965.

[7] H. Fritzsch, M. Gell-Mann and H. Leutwyler. *Advantages of the color octet gluon picture*. Phys. Lett., vol. B47, p. 365, 1973.

[8] D. J. Gross and F. Wilczek. *Ultraviolet behavior of non-abelian gauge theories*. Phys. Rev. Lett., vol. 30, p. 1343, 1973.

[9] H. D. Politzer. *Reliable perturbative results for strong interactions?* Phys. Rev. Lett., vol. 30, p. 1346, 1973.

[10] C. Glasman. *Precision measurements of α_S at HERA*. AIP Conf. Proc., vol. 792, p. 689, 2005. {hep-ex/0506035}.

[11] J. C. Collins, D. E. Soper and G. Sterman. *Factorization of hard processes in QCD*. Adv. Ser. Direct. High Energy Phys., vol. 5, p. 1, 1988. {hep-ph/0409313}.

[12] H. Plothow-Besch. *PDFLIB: A library of all available parton density functions of the nucleon, the pion and the photon and the corresponding α_S calculations*. Comput. Phys. Commun., vol. 75, p. 396, 1993.

[13] ZEUS Collaboration. S. Chekanov et al. *An NLO QCD analysis of inclusive cross-section and jet-production data from the ZEUS experiment.* Eur. Phys. J., vol. C42, p. 1, 2005. {hep-ph/0503274}.

[14] S. Frixione, M. L. Mangano, P. Nason and G. Ridolfi. *Improving the Weizsacker-Williams approximation in electron-proton collisions.* Phys. Lett., vol. B319, p. 339, 1993. {hep-ph/9310350}.

[15] S. Frixione and G. Ridolfi. *Jet photoproduction at HERA.* Nucl. Phys., vol. B507, p. 315, 1997. {hep-ph/9707345}.

[16] ZEUS Collaboration. M. Derrick et al. *Dijet cross-sections in photoproduction at HERA.* Phys. Lett., vol. B348, p. 665, 1995. {hep-ex/9502008}.

[17] ZEUS Collaboration. M. Derrick et al. *Dijet angular distributions in direct and resolved photoproduction at HERA.* Phys. Lett., vol. B384, p. 401, 1996. {hep-ex/9605009}.

[18] J. M. Butterworth, J. R. Forshaw, T. Sjöstrand and J. K. Storrow. *Multiple hard parton interactions at HERA.* J. Phys., vol. G22, p. 883, 1996. {hep-ph/9601322}.

[19] J. M. Butterworth, J. R. Forshaw and M. H. Seymour. *Multiparton interactions in photoproduction at HERA.* Z. Phys., vol. C72, p. 637, 1996. {hep-ph/9601371}.

[20] T. Sjöstrand and M. van Zijl. *A multiple interaction model for the event structure in hadron collisions.* Phys. Rev., vol. D36, p. 2019, 1987.

[21] CDF Collaboration. F. Abe et al. *Measurement of double parton scattering in $\bar{p}p$ collisions at $\sqrt{s} = 1.8\,\mathrm{TeV}$.* Phys. Rev. Lett., vol. 79, p. 584, 1997.

[22] T. Namsoo. *Three- and four-jet states in photoproduction at HERA.* Ph.D. Thesis, U. Bristol, 2006.

[23] H1 Collaboration. S. Aid et al. *Jets and energy flow in photon-proton collisions at HERA.* Z. Phys., vol. C70, p. 17, 1996. {hep-ex/9511012}.

[24] CDF Collaboration. R. D. Field. *Studying the underlying event at CDF.* Presented at 33rd International Conference on High Energy Physics (ICHEP 06), Moscow, Russia, 26 July - 2 August 2006.

[25] G. A. Voss and B. H. Wiik. *The electron proton collider HERA.* Ann. Rev. Nucl. Part. Sci., vol. 44, p. 413, 1994.

[26] H1 Collaboration. I. Abt et al. *The H1 detector at HERA.* Nucl. Instrum. Meth., vol. A386, p. 310, 1997.

[27] HERMES Collaboration. K. Ackerstaff et al. *HERMES spectrometer.* Nucl. Instrum. Meth., vol. A417, p. 230, 1998. {hep-ex/9806008}.

[28] E. Hartouni et al. *HERA-B: An experiment to study CP violation in the B system using an internal target at the HERA proton ring. Design report.* DESY-PRC-95-01.

[29] ZEUS Collaboration. *The ZEUS detector: Status report 1993.* ZEUS-STATUS-REPT-1993.

[30] R. Hall-Wilton, N. McCubbin, P. Nylander, M. Sutton and M. Wing. *The CTD tracking resolution.* 1999. ZEUS-99-024.

[31] L. Lönnblad, S. Mrenna and T. Sjöstrand. *PYTHIA 6.2. Physics and manual.* 2001. {hep-ph/0108264}.

[32] P. Skands, S. Mrenna and T. Sjöstrand. *PYTHIA 6.4. Physics and manual.* JHEP, vol. 05, p. 026, 2006. {hep-ph/0603175}.

[33] B. Andersson, G. Gustafson, G. Ingelman and T. Sjöstrand. *Parton fragmentation and string dynamics.* Phys. Rept., vol. 97, p. 31, 1983.

[34] T. Sjöstrand. Private communication, 19 September 2006.

[35] R. Brun, F. Bruyant, M. Maire, A. C. McPherson and P. Zanarini. *GEANT3.* 1987. CERN-DD/EE/84-1.

[36] CTEQ Collaboration. H. L. Lai et al. *Improved parton distributions from global analysis of recent deep inelastic scattering and inclusive jet data.* Phys. Rev., vol. D55, p. 1280, 1997. {hep-ph/9606399}.

[37] CTEQ Collaboration. H. L. Lai et al. *Global QCD analysis of parton structure of the nucleon: CTEQ5 parton distributions.* Eur. Phys. J., vol. C12, p. 375, 2000. {hep-ph/9903282}.

[38] M. Glück, E. Reya and A. Vogt. *Photonic parton distributions.* Phys. Rev., vol. D46, p. 1973, 1992.

[39] L. Lönnblad. *ARIADNE version 4: A program for simulation of QCD cascades implementing the color dipole model.* Comput. Phys. Commun., vol. 71, p. 15, 1992.

[40] H. Abramowicz, A. Caldwell and R. Sinkus. *Neural network based electron identification in the ZEUS calorimeter.* Nucl. Instrum. Meth., vol. A365, p. 508, 1995. {hep-ex/9505004}.

[41] G. M. Briskin. *Diffractive dissociation in e p deep inelastic scattering.* Ph.D. Thesis, U. Tel Aviv, 1998.

[42] J. H. Vossebeld. *Dijet photoproduction at high transverse energies.* Ph.D. Thesis, U. Amsterdam, 1999.

[43] U. Amaldi (ed.). *Study of an e p facility for Europe: Proceedings, ECFA, Hamburg, Germany, April 2-3, 1979*. DESY-79-48.

[44] J. E. Huth et al. *Toward a standardization of jet definitions*. Presented at Summer Study on High Energy Physics, Research Directions for the Decade, Snowmass, USA, 25 June - 13 July 1990.

[45] S. Catani, Y. L. Dokshitzer, M. H. Seymour and B. R. Webber. *Longitudinally invariant $k_\perp$-clustering algorithms for hadron hadron collisions*. Nucl. Phys., vol. B406, p. 187, 1993.

[46] S. D. Ellis and D. E. Soper. *Successive combination jet algorithm for hadron collisions*. Phys. Rev., vol. D48, p. 3160, 1993. {hep-ph/9305266}.

[47] ZEUS Collaboration. S. Chekanov et al. *Dijet photoproduction at HERA and the structure of the photon*. Eur. Phys. J., vol. C23, p. 615, 2002. {hep-ex/0112029}.

[48] W. T. Giele, E. W. N. Glover and D. A. Kosower. *The two jet differential cross-section at $\mathcal{O}(\alpha_s^3)$ in hadron collisions*. Phys. Rev. Lett., vol. 73, p. 2019, 1994. {hep-ph/9403347}.

[49] G. Corcella et al. *HERWIG 6: An event generator for hadron emission reactions with interfering gluons (including supersymmetric processes)*. JHEP, vol. 1, p. 10, 2001. {hep-ph/0011363}.

[50] R. Cousins, G. Cowan and F. James. *Statistics*. In: Particle Data Group. W.-M. Yao et al. *Review of particle physics*. J. Phys., vol. G33, p. 301. 2006.